On Integral Quadratic Constraint Theory and Robust Control of Unmanned Aircraft Systems

Jedediah Micah Fry

Dissertation submitted to the Faculty of the
Virginia Polytechnic Institute and State University
in partial fulfillment of the requirements for the degree of

Doctor of Philosophy
in
Aerospace Engineering

Mazen H. Farhood, Chair
Craig A. Woolsey
Mayuresh J. Patil
Daniel J. Stilwell

July 22, 2019
Blacksburg, Virginia

Keywords: integral quadratic constraints, unmanned aircraft systems, robust control, linear time-varying systems, $\mathcal{H}_\infty/\mathcal{H}_2$/PID control, path following, trajectory tracking

On Integral Quadratic Constraint Theory and Robust Control of Unmanned Aircraft Systems

Jedediah Micah Fry

(ABSTRACT)

This dissertation advances tools for the certification of unmanned aircraft system (UAS) flight controllers. We develop two thrusts to this goal: (1) the validation and improvement of an uncertain UAS framework based on integral quadratic constraint (IQC) theory and (2) the development of novel IQC theorems which allow the analysis of uncertain systems having time-varying characteristics.

Pertaining to the first thrust, this work improves and implements an IQC-based robustness analysis framework for UAS. The approach models the UAS using a linear fractional transformation on uncertainties and conducts robustness analysis on the uncertain system via IQC theory. By expressing the set of desired UAS flight paths with an uncertainty, the framework enables analysis of the uncertain UAS flying about any level path whose radius of curvature is bounded. To demonstrate the versatility of this technique, we use IQC analysis to tune trajectory-tracking and path-following controllers designed via $\mathcal{H}_2$ or $\mathcal{H}_\infty$ synthesis methods. IQC analysis is also used to tune path-following PID controllers. By employing a non-deterministic simulation environment and conducting numerous flight tests, we demonstrate the capability of the framework in predicting loss of control, comparing the robustness of different controllers, and tuning controllers. Finally, this work demonstrates that signal IQCs have an important role in obtaining IQC analysis results which are less conservative and more consistent with observations from flight test data.

With regards to the second thrust, we prove a novel theorem which enables robustness analysis of uncertain systems where the nominal plant and the IQC multiplier are linear time-varying systems and the nominal plant may have a non-zero initial condition. When the nominal plant and the IQC multiplier are eventually periodic, robustness analysis can be accomplished by solving a finite-dimensional semidefinite program. Time-varying IQC multipliers are beneficial in analysis because they provide the possibility of reducing conservatism and are capable of expressing uncertainties that have unique time-domain characteristics. A number of time-varying IQC multipliers are introduced to better describe such uncertainties. The utility of this theorem is demonstrated with various examples, including one which produces bounds on the UAS position after an aggressive Split-S maneuver.

On Integral Quadratic Constraint Theory and Robust Control of Unmanned Aircraft Systems

Jedediah Micah Fry

(GENERAL AUDIENCE ABSTRACT)

This work develops tools to aid in the certification of unmanned aircraft system (UAS) flight controllers. The forthcoming results are founded on robust control theory, which allows the incorporation of a variety of uncertainties in the UAS mathematical model and provides tools to determine how robust the system is to these uncertainties. Such a foundation provides a complementary perspective to that obtained with simulations. Whereas simulation environments provide a probabilistic-type analysis and are oftentimes costly, the following results provide worst-case guarantees—for the allowable disturbances and uncertainties—and require far less computational resources. Here we take two approaches in our development of certification tools for UAS. First we validate and improve on an uncertain UAS framework that relies on integral quadratic constraint (IQC) theory to analyze the robustness of the UAS in the presence of uncertainties and disturbances. Our second approach develops novel IQC theorems that can aid in providing bounds on the UAS state during its flight trajectory. Though the applications in this dissertation are focused on UAS, the theory can be applied to a wide variety of physical and nonphysical problems wherein uncertainties in the mathematical model cannot be avoided.

Dedication

To my wife, Rachel, and our children, Rosy, Atticus, and Mercedes

Acknowledgments

I am most grateful to my God and Savior, on whose patience, mercy, and strength I continually rely. I am also grateful for my advisor, Dr. Mazen Farhood. I sought a keen theoretician with the guts to apply things in the real-world; I found not only that, but a friend, a guide, and an incredible mentor. His efforts also secured the funding that was provided by the National Science Foundation (Grant # CMMI-1351640) and NAVAIR (Contract # N00421-16-2-0001), without which this dissertation would not have been possible. Thank you. I would also like to thank my committee members, Dr. Craig Woolsey, Dr. Mayuresh Patil, and Dr. Dan Stilwell. Your comments and questions throughout my research helped me develop new tools and uncover new observations that would not have been realized otherwise. A special thanks to Devaprakash Muniraj, our late night theoretical discussions and long flight campaigns in freezing weather are as amusing to me now as they were fruitful then. I also appreciate Dany Abou Jaoude for our many discussions on IQC theory and for sharing the excitement felt when grasping a new result. Sanity is (or probably should be) an important trait for aspiring PhD students; I owe a debt to my labmates Jean-Michel Fahmi, Billy Greer, Hunter McClelland, Deva, and Dany for buoying me up in this regard.

I would be remiss if I did not thank my mom and dad. Both the values they have taught and the love they have shown me have made all the difference. Among all my friends, family, and colleagues, I am most indebted to my wife Rachel. Rachel's patience and mettle have been my stable anchor in the midst of a turbulent flow. She brought our beautiful children into this world and together they have given my life meaning. Rosy, Atticus, and Mercedes, the value of dedicating my dissertation to you pales in comparison to the joy you have brought me. I suppose I have no choice but to try dedicating my whole life instead.

Contents

List of Figures

List of Tables

List of Abbreviations

UAS	unmanned aircraft system
IQC	integral quadratic constraint
LTI	linear time-invariant
LTV	linear time-varying
LFT	linear fractional transformation
CG	center of gravity
KYP	Kalman-Yakubovich-Popov
SDP	semidefinite program
6-DOF	six-degrees-of-freedom
LPF	low pass filter
IDM	infinite dimensional matrix
$\mathbb{R}_+$	Nonnegative real numbers
$\mathbb{R}_{++}$	Positive real numbers
$\mathbb{R}^n$	Real n-tuples (real vectors of dimension n)
$\mathbb{R}^{n\times m}$	Real $n \times m$ matrices
$\mathbb{S}^n$	Real $n \times n$ symmetric matrices

$x^\times$ Skew-symmetric matrix representation of $x \in \mathbb{R}^3$

$X \otimes Y$ Kronecker product of matrices X and Y

$\|x\|$ Norm of x

$\langle x, y \rangle$ Inner product of x and y

X^* Adjoint of operator or matrix X

X^T Transpose of matrix X

$X \succeq 0$ Operator or matrix X is positive semidefinite

$X \succ 0$ Operator or matrix X is positive definite

ℓ_{2e}^n Space of $\mathbb{R}^n$-valued semi-infinite sequences

ℓ_2 Space of square-summable sequences in ℓ_{2e}

$I,\ I_n$ Identity operator or matrix, Identity $n \times n$ matrix

$\hat{M},\ \hat{d}$ Frequency-domain representation of LTI operator M or ℓ_2 signal d

$x^\star$ Trim value, reference trajectory, or reference signal

$\bar{x}$ Error from trim value, reference trajectory, or reference signal

$\mathcal{RL}_\infty$ Space of real-rational matrix-valued functions essentially bounded on the unit circle

$\mathcal{RH}_\infty$ Subspace of $\mathcal{RL}_\infty$ with functions analytic outside the unit circle

$\|M\|_{D \to E}$ D-to-E induced norm of $M : D \to E$

$\|\hat{M}\|_2$ $\mathcal{H}_2$ norm of $\hat{M}$

$\|\hat{M}\|_\infty$ $\mathcal{H}_\infty$ norm of $\hat{M}$

$\hat{M}^{\sim}$ Para-hermitian conjugate of $\hat{M}$

(M, Δ) Upper LFT of M and Δ

$\left[\begin{array}{c|c} A & B \\ \hline C & D \end{array}\right]$ State-space realization of $\hat{M}$, where $\hat{M}(z) = D + C(zI - A)^{-1}B$

$\mathrm{diag}(A, B)$ Block diagonal augmentation of A and B

N_+ The set $\{N, N+1, \ldots\}$

N_- The set $\{0, 1, \ldots, N-1\}$ (0_- is the empty set)

$\ell_2(N)$ Set of signals in ℓ_2 with support on $N \subseteq 0_+$

$\mathbb{P}_N^+$ Projection operator from ℓ_2 to $\ell_2(N_+)$

$\mathbb{P}_N^-$ Projection operator from ℓ_2 to $\ell_2(N_-)$

${}^N G$, ${}^N u$ Causal Toeplitz operator for G ($\mathbb{P}_N^+ G \mathbb{P}_N^+$), or forward truncation of u ($\mathbb{P}_N^+ u$)

${}_N G$, ${}_N u$ Anticausal Toeplitz operator for G ($\mathbb{P}_N^- G \mathbb{P}_N^-$), or backward truncation of u ($\mathbb{P}_N^- u$)

${}_N^T G$ ${}_N^T G = ({}_N({}^T G)) = ({}^T({}_N G))$

$\{\!\!\{x_1, x_2\}\!\!\}$ Interchangeable notation for $\begin{bmatrix} x_1 \\ x_2 \end{bmatrix}$

$\mathcal{E}(\Xi)$ Ellipsoid defined by positive definite matrix Ξ

Chapter 1

Introduction

Ensuring that a flight controller will safely perform its assigned task is a critical part of airworthiness certification. The accepted standard for software certification of airborne systems—DO-178C—states that the controller software must meet agreed upon performance requirements; this includes the requirement that the controller stabilizes the aircraft and safely tracks commands within some tolerance [3, 4]. The Department of Defense is also concerned with these, as flight control systems have been a leading cause of unmanned aircraft system (UAS) failures [5]. As UAS are designed to be less costly and more modifiable than manned aircraft, the certification process for a UAS flight controller must also be modular and economical.

Besides flight tests, there are two methodologies which guide the flight controller certification procedure: simulating the controlled UAS and using control theory to prove stability and performance characteristics of the UAS [6, 7]. Simulation environments typically sample uncertainties within an uncertainty space, conduct numerous simulations, and provide an estimate on the probable performance of the UAS in physical flight [8]. Though this approach provides useful information, simulation environments oftentimes predict better performance than experienced in flight and require considerable resources (time, computational effort, and money). When applying control theory for certifying the UAS controller, the engineer typically assumes a simplified model of the UAS and draws from a suite of theoretic tools (Lyapunov theory, Bode plots, input-output theory, etc.) to obtain a rigorous stability or

performance guarantee [9, 10]. However, once these simplifying assumptions are removed, as is the case for a physical UAS, such theoretical guarantees are lost, and the theory is incapable of providing a rigorous proof or the mathematical argument must be re-derived.

This dissertation develops tools to aid in the certification of UAS flight controllers. Its contributions can be divided into two themes. The first theme looks strictly at the application of integral quadratic constraint (IQC) theory [11] to the UAS. Though the uncertain UAS framework was originally derived in [12], the results given therein were only validated by simulation environments. The following results demonstrate how it can be applied to a physical UAS, and provide validation of the uncertain UAS framework via simulations and flight tests [13]. We furthermore improve this framework by parameterizing the set of trim-points about which the UAS operates, thus allowing the IQC analysis framework to apply to a UAS flying arbitrary level paths with bounds on the radius of curvature. An exhaustive series of flight tests also accompany this improvement to the framework, demonstrating its utility on a variety of flight controller schemes (path-following/trajectory-tracking and $\mathcal{H}_\infty/\mathcal{H}_2$/PID) [14]. The second theme develops novel IQC-based robustness analysis theorems. By building from dissipativity-based arguments demonstrated in [15], we show how IQC analysis can be applied when there may be uncertain initial conditions and the nominal system G and/or the IQC multiplier Π are time-varying. When both systems are eventually-periodic, a finite-dimensional semidefinite program (SDP) may be solved to conduct robustness analysis.

1.1 Validating an uncertain UAS framework

Chapters 3 and 4 implement a framework based off robustness analysis and IQCs to aid in the certification and design of UAS flight controllers. The full six-degrees-of-freedom (6-DOF)

equations of motion are used to model the UAS, with uncertainties included to account for modeling inaccuracies and the effect of removing simplifying assumptions from the analysis. By modeling the system as a linear fractional transformation (LFT) on uncertainties, IQC analysis is capable of determining an upper bound on the worst-case performance of the UAS, thereby providing a conservative perspective. This complements the oftentimes optimistic results seen from uncertain simulation environments. Because IQC theory is well-suited for a large suite of uncertainty types, this framework provides assessments on a closer approximation of the physical system and can flexibly include or remove uncertainties in the analysis. These tools empower engineers in rigorously understanding the effect of multiple uncertainties and their interactions on the system's stability and performance.

We select IQC analysis to measure robust performance because it is capable of both considering numerous types of uncertainties and specifying characteristics of the system's exogenous disturbances [16,17]. Although the first point is well recognized and explored in the academic community, unfortunately the latter point is not often investigated. Our results indicate the importance of characterizing disturbances in both obtaining consistent predictions for physical flight and achieving less conservative robust performance results.

Similar to IQC analysis, μ-analysis can provide robustness assertions for uncertain systems [18, 19]. Though μ-analysis can be less computationally demanding than IQC analysis, it cannot incorporate the wide variety of uncertainties that IQC analysis can. Not only can IQC analysis incorporate static and dynamic time-invariant uncertainties, but it can consider time-varying (rate-bounded and arbitrarily fast) uncertainties, nonlinear (sector-bounded, norm-bounded, slope-restricted, and passive) uncertainties, and a variety of delay uncertainties [11, 20].

A variety of works have utilized IQC analysis to provide robustness assertions for aircraft flight controllers. Most of these have focused on analyzing simplified longitudinal aircraft

models: in [21] the authors consider the longitudinal dynamics of an ONERA fighter aircraft with uncertainties in the aerodynamics, flight envelope, and model parameters; [22] analyzes the robustness of the NASA HL-20 longitudinal model in the presence of aerodynamic, parametric, actuator, and time-delay uncertainties; [23] studies the short period pitch model of a Cessna Citation 500 parameterized by altitude and airspeed; [24] considers the short period dynamics of the NASA Generic Transport Model. Other groups have investigated the application of IQC analysis to understand the stability properties of aeroelastic vehicles: [25] studies the stability of an aeroelastic aircraft with freeplay in the elevator actuation; the aeroelastic longitudinal dynamics of the B-1 Lancer gridded by altitude and airspeed are analyzed in [26]; the work in [27] studies the stability of the aeroelastic longitudinal dynamics with parametric uncertainties and freeplay. The work herein differs from the previously cited works in that it studies robustness properties of the UAS 6-DOF equations of motion with uncertainties and/or nonlinearities in the aerodynamic, dynamic, and actuator models. Furthermore, we provide validation of this framework by conducting numerous flight tests and comparing results against predictions from the IQC-based framework and a non-deterministic simulation environment.

Building off the work in [12], Chapter 3 discusses the uncertain UAS framework implemented and validated herein. Uncertainties inherent to the UAS aerodynamics, actuation and control, and dynamics are characterized, quantified, and expressed in the UAS model. To clearly attribute the content in this dissertation, all the derivations in Section 3.2 are first developed in [12]. However, they were not applied to the Senior Telemaster Plus, whose nominal model is detailed in Chapter 2. Applying the uncertain UAS framework to the Senior Telemaster Plus is a contribution of the current author. As an additional contribution, we demonstrate the application of model reduction techniques (specifically the coprime factors reduction method [28]) in Section 3.2.3 to obtain a computationally tractable model of

the uncertain UAS. The expression of the uncertain UAS framework in Section 3.2 appears for completeness, and–except for the aerodynamic uncertainty bounds in Section 3.2.1 and the model reduction technique in Section 3.2.3–should be understood to originate from the work in [12]. Further details on the derivations of these uncertainties and how they are incorporated can be found in [13].

The approach is shown to effectively identify the system's sensitivities to uncertainties, compare controllers' performance, and tune $\mathcal{H}_\infty$ controllers. Despite the successes demonstrated therein, additional work was needed in improving and exhibiting the capabilities and consistency of the method. Chapter 4 augments the framework by incorporating flight characteristics of the uncertain UAS when operating at a variety of trim points. In other words, Chapter 4 broadens the robustness certificate to flight about any level path whose radius of curvature is bounded. This stands in contrast to Chapter 3, whose results pertained only to flight about a predetermined trim point.

Additionally, we develop an original description of UAS path-following dynamics. Although the work in [29] develops an approach to path-following control that is supported by flight tests (see also [1]), the dynamic equations given therein assume that the angle of attack and sideslip angle are negligible, which is not the case in the presence of significant wind. In Chapter 4, we develop an accurate description of the UAS path-following dynamics without these assumptions.

The framework is shown to tune and compare trajectory-tracking $\mathcal{H}_\infty$ (TT$\mathcal{H}_\infty$), trajectory-tracking $\mathcal{H}_2$ (TT$\mathcal{H}_2$), path-following $\mathcal{H}_\infty$ (PF$\mathcal{H}_\infty$), path-following $\mathcal{H}_2$ (PF$\mathcal{H}_2$), and path-following PID (PFpid) controllers. Trajectory-tracking controllers seek to regulate the UAS state with explicit timing constraints, whereas path-following controllers may not have an explicit timing constraint. By conducting numerous simulations and flight tests for a variety of controllers, we show that the uncertain system's robust performance is the most consistent

measure in predicting and comparing controller performance in physical flight. With the acquired simulation and flight test data, the approach is shown to reliably indicate when a controller is insufficiently robust and may lead to loss of control. Furthermore, with IQC analysis, simulations, and flight tests, the merits of path-following over trajectory-tracking control are manifest. This supports the theoretical arguments respecting the superiority of path-following control [30]. We also observe that our $\mathcal{H}_\infty$ and $\mathcal{H}_2$ controllers provide better performance than our PID controller.

The proposed framework is not used to rigorously provide bounds on the worst-case performance for the physical system. Rather, it is a fast, inexpensive, and additional metric in understanding a system's sensitivities to uncertainties, comparing robustness of controllers, and tuning controllers. Moreover, simulation and flight test data demonstrate it is a *reliable* metric, capable of predicting loss of control when non-deterministic simulations may not.

1.2 A novel IQC theorem for time-varying systems

In their seminal paper [11], Megretski and Rantzer place the fulcrum of IQC theory on a bounded, self-adjoint operator Π. Therein, it is demonstrated that if, among other hypotheses, $\begin{bmatrix} G^* & I \end{bmatrix} \Pi \begin{bmatrix} G^* & I \end{bmatrix}^* \preceq -\epsilon I$ $(\epsilon > 0)$, then robustness assertions can be made on an associated interconnection. Verifying the aforementioned operator inequality* is perhaps the most burdensome task in IQC theory and becomes tractable when $G \in \mathcal{RH}_\infty$ and $\Pi \in \mathcal{RL}_\infty$. Chapter 5 demonstrates that G and Π can be in a broader class of operators while affording a computational method for checking the previous operator inequality.

This work is not the first to treat IQC theory where G or Π may be time-varying. To date,

*The original result in [11] expresses G and Π in the frequency domain, but the proof can be replicated where G and Π are (more generally) bounded operators (see [31]).

there are two main approaches which consider such a paradigm. The first approach relies on linking the time-varying system model to a representation in the frequency domain and relying on the celebrated IQC theorem in [11] to conduct robustness analysis. For instance, results in [32] apply IQC analysis to periodic nominal systems G by using periodic IQC multipliers. Periodic IQC multipliers are also used to investigate the stability of periodic solutions for uncertain periodic systems in [33]. In [34], periodically time-varying multipliers are employed to introduce noncausal scaling for robustness analysis. The common linkage between these time-varying systems and the frequency domain is generally through a variety of lifting techniques. Though such an approach is useful for periodic systems, the lifting methods therein employed cannot treat finite-horizon systems, eventually periodic system, or general time-varying systems.

The other main approach which intersects time-varying systems with IQC theory relies on dissipativity-based arguments [35, 36]. These arguments have allowed analysis of uncertain interconnections where the nominal system is linear parameter-varying (LPV) [37], or time-varying in general [38]. However, standard dissapativity-based arguments require more restrictive conditions when asserting robustness, as compared to the homotopy-based result given in [11]. In the works [15,39] it is shown that these restrictions can be relaxed by identifying appropriate factorizations of the IQC multiplier Π. Such work illuminatingly presented IQC theory in the time domain, and results in both the continuous- and discrete-time domain followed [40, 41].

The forthcoming results follow from the dissipativity-based approach to IQC analysis given in [15]. The enabling key in this dissipativity-based approach is a requirement that IQC multipliers have a J-spectral (or canonical) factorization [42–44], a property guaranteed when Π is positive negative. The first connections between IQC theory and J-spectral factorizations were discussed in [45,46]. Though enforcing the IQC multipliers to be positive

negative is a constraint that is not required in [11], this is a relatively minor restriction since the vast majority of known IQC multipliers already satisfy said property. Recent work in [47] also links dissipativity and IQCs by providing a theorem based on hard IQCs with terminal costs. Though not explicitly addressed, the novel approach of [47] has the potential of being generalized to time-varying systems. In Chapter 5, we employ notions of dichotomicity and Popov indices [48] to prove that the dissipativity-based argument extends to analysis of interconnections where G is time-varying and/or Π may be a positive-negative time-varying IQC multiplier [49, 50]. Under this framework, it is also demonstrated how uncertain initial conditions in the nominal system may be incorporated in IQC analysis.

Another related result which belongs neither in the frequency-domain treatment nor the dissapativity-based approach of IQC theory is found in [51]. The IQC analysis theorems presented therein are for both continuous- and discrete-time LTV systems and rely on co-prime factorizations and gap metrics in an operator context. However, the theorems require verifying infinite-dimensional constraints and the authors have not suggested computationally tractable methods. An important benefit of the results in this dissertation is their computational application; if both G and Π are eventually periodic, then one need only solve a finite-dimensional SDP to conduct IQC analysis.

The advantages of applying time-varying IQC multipliers are two-fold. First, standard LTI IQC multipliers can be more flexibly defined, where the factors (Ψ, M) of Π can now be time-varying. This is a useful technique for reducing the conservatism of IQC analysis. Second, novel IQC multipliers may be defined which more aptly describe uncertainties with time-domain characteristics. Many of these new multipliers can be defined by intuitively modifying LTI IQC multipliers, and a few are presented. The last portion of Chapter 5 provides two different examples which apply the aforementioned results. First, we demonstrate how robust bounds on the UAS state (after executing an aggressive Split-S maneuver) may be

generated [38]. Second, we show how time-varying IQC multipliers may be used to better characterize uncertainties with an inverted pendulum example.

1.3 Published materials and structure of dissertation

The following publications and submissions contain the results in this dissertation:

[38] J. M. Fry, M. Farhood, and P. Seiler, "IQC-based robustness analysis of discrete-time linear time-varying systems," *International Journal of Robust and Nonlinear Control*, vol. 27, no. 16, pp. 3135–3157, Nov. 2017. © 2017 John Wiley & Sons, Ltd.

[52] J. M. Fry and M. Farhood, "Robustness analysis of eventually periodic systems using integral quadratic constraints with periodic multipliers," in *Proceedings of the 2017 IEEE 56th Annual Conference on Decision and Control (CDC)*, Melbourne, Australia, Dec. 12–15 2017, pp. 2967–2972. © 2017 IEEE

[13] M. Palframan, J. M. Fry, and M. Farhood, "Robustness analysis of flight controllers for fixed-wing unmanned aircraft systems using integral quadratic constraints," *IEEE Transactions on Control Systems Technology*, vol. 27, no. 1, pp. 86–102, Jan. 2019. © 2017 IEEE

[49] J. M. Fry and M. Farhood, "IQC-based robustness analysis with time-varying multipliers," in *Proceedings of the 2019 American Control Conference (ACC)*, Philadelphia, PA, USA, Jul. 10–12 2019, pp. 1786–1791. © 2019 IEEE

[14] J. M. Fry and M. Farhood, "A comprehensive analytical tool for control validation of fixed-wing unmanned aircraft," *IEEE Transactions on Control Systems Technology*, pp. 1–17, 2019, doi: 10.1109/TCST.2019.2923649. © 2019 IEEE

[50] J. M. Fry, D. Abou Jaoude, and M. Farhood, "Robustness analysis of uncertain

time-varying systems using integral quadratic constraints with time-varying multipliers," Submitted.

In Chapter 2 we provide preliminary notions that are referred to in later chapters. These notions focus on the modeling of the nominal UAS, system robustness, and some basic principles of IQC theory. Chapter 3 is mostly drawn from [13], in which we implement and validate the uncertain UAS framework on the Senior Telemaster Plus (94-inch wingspan) aircraft. The results from [14] are found in Chapter 4, which details improvements made and further validation for the uncertain UAS framework. Chapter 5 provides a novel robustness analysis theorem which extends IQC theory to time-varying systems. The work in [38, 49, 50, 52] comprise Chapter 5. Concluding remarks are made in Chapter 6.

Chapter 2

Preliminaries

2.1 Notation

The sets of nonnegative reals, positive reals, real vectors of dimension n, real $n \times m$ matrices, and real $n \times n$ symmetric matrices are denoted by $\mathbb{R}_+$, $\mathbb{R}_{++}$, $\mathbb{R}^n$, $\mathbb{R}^{n\times m}$, and $\mathbb{S}^n$, respectively. The skew-symmetric matrix representation of a vector $x = [a\, b\, c]^T$ and the Kronecker product of $X \in \mathbb{R}^{m\times n}$ and the matrix Y are given by

$$x^\times = \begin{bmatrix} 0 & -c & b \\ c & 0 & -a \\ -b & a & 0 \end{bmatrix} \text{ and } X \otimes Y = \begin{bmatrix} x_{11}Y & \dots & x_{1n}Y \\ \vdots & \ddots & \vdots \\ x_{m1}Y & \dots & x_{mn}Y \end{bmatrix}$$

respectively. The symbols X^* and X^T denote the adjoint and the transpose of X, respectively. Given a Hilbert space $\mathcal{H}$ with the inner-product $\langle \cdot, \cdot \rangle$, the operator $X = X^*$ is positive semidefinite ($X \succeq 0$) if $\langle u, Xu \rangle \geq 0$ for all $u \in \mathcal{H}$. The operator is positive definite ($X \succ 0$) if there exists an $\epsilon > 0$ such that $\langle u, Xu \rangle \geq \epsilon \langle u, u \rangle$ for all $u \in \mathcal{H}$. The space of $\mathbb{R}^n$-valued semi-infinite sequences $d = (d(0), d(1), \dots)$ is denoted by ℓ_{2e}^n. The Hilbert space $\ell_2^n \subset \ell_{2e}^n$ consists of square-summable sequences with the inner product and norm defined by $\langle d, d \rangle = \|d\|^2 := \sum_{k=0}^{\infty} d(k)^T d(k)$. When the dimension is irrelevant to the discussion, the superscript n is suppressed. The symbol I represents the identity operator. Given a positive integer n, we use I_n to denote an $n \times n$ identity matrix. Given a signal $d \in \ell_2$

and an LTI operator M, the symbols $\hat{d}$ and $\hat{M}$ denote the corresponding frequency-domain interpretations obtained via the Fourier transform. With a slight abuse of notation, the sequel uses e to represent an ℓ_2 signal and $e^{j\omega}$ to represent the natural exponential of $j\omega$. Given a variable x and its trim value $x^\star$, the error from trim is $\bar{x} := x - x^\star$. The space of real-rational matrix-valued functions essentially bounded on the unit circle is denoted by $\mathcal{RL}_\infty$. The subspace of $\mathcal{RL}_\infty$ with functions analytic outside the unit circle is symbolized by $\mathcal{RH}_\infty$. For a bounded operator $M : D \to E$, where D and E are Banach spaces, $\|M\|_{D\to E} := \sup_{0\neq d\in D}(\|Md\|_E/\|d\|_D)$ is the D-to-E induced norm of M. When D is a subset of E, then $\|d\|_D = \|d\|_E$. When M is LTI, $\|\hat{M}\|_2^2 := (1/(2\pi))\int_{-\pi}^{\pi} \mathrm{trace}(\hat{M}(e^{j\omega})^*\hat{M}(e^{j\omega}))d\omega$ and $\|\hat{M}\|_\infty := \sup_{\omega\in[-\pi,\pi]} \bar{\sigma}(\hat{M}(e^{j\omega}))$, where $\bar{\sigma}(\cdot)$ denotes the maximum singular value. The para-Hermitian conjugate of $\hat{M} \in \mathcal{RL}_\infty$ is $\hat{M}^\sim(z) = \hat{M}(z^{-1})^T$. Given operators M and Δ, the upper LFT of M and Δ is

$$\left(\left[\begin{array}{c:c} M_{11} & M_{12} \\ \hdashline M_{21} & M_{22} \end{array}\right], \Delta\right) := M_{22} + M_{21}\Delta(I - M_{11}\Delta)^{-1}M_{12}.$$

The realization of $\hat{M}$ is expressed by $\left[\begin{array}{c|c} A & B \\ \hline C & D \end{array}\right]$, where $D + C(zI - A)^{-1}B = \hat{M}(z)$. For matrices A and B, their block-diagonal augmentation is denoted by $\mathrm{diag}(A, B) := \begin{bmatrix} A & 0 \\ 0 & B \end{bmatrix}$. Sometimes relation symbols (e.g., $=$, $\succ$, etc.) appear alongside vertically aligned terms, which denotes the relation between terms immediately adjacent to each other. For example,

$$\begin{aligned} A &= B \\ &\leq C \\ &= D \end{aligned}$$

is to be understood as $A = B \leq C = D$.

For any natural number N, we define the sets $N_+ = \{N,\ N+1, \ldots\}$ and $N_- = \{0,\ 1, \ldots, N-1\}$, with 0_- being the empty set. For any $N \in 0_+$, we define the Hilbert subspaces $\ell_2(N_+)$ and $\ell_2(N_-)$, which are the spaces of square-summable sequences with support on N_+ and N_-, respectively. These subspaces are orthogonal complements of each other, and $\ell_2(N_+) \bigoplus \ell_2(N_-) = \ell_2$. Given any $N \in 0_+$, the operators $\mathbb{P}_N^+$ and $\mathbb{P}_N^-$ are orthogonal projections from ℓ_2 to $\ell_2(N_+)$ and $\ell_2(N_-)$, respectively. For any $N \in 0_+$ and an operator G on ℓ_2, its causal (anticausal) Toeplitz operator is ${}^N G := \mathbb{P}_N^+ G \mathbb{P}_N^+$ (${}_N G := \mathbb{P}_N^- G \mathbb{P}_N^-$); for any $T \in 0_+$, we denote ${}^T({}_N G) = {}_N ({}^T G)$ by ${}_N^T G$. An operator G on ℓ_2 is said to be causal if ${}^N G = G\mathbb{P}_N^+$, or equivalently, ${}_N G = \mathbb{P}_N^- G$ for all $N \in 0_+$. Given $N \in 0_+$ and a signal $u \in \ell_2$, we define the symbols ${}_N u := \mathbb{P}_N^- u$ and ${}^N u := \mathbb{P}_N^+ u$. Given Hilbert spaces $\mathcal{H}_1$ and $\mathcal{H}_2$ and elements $x_1 \in \mathcal{H}_1$ and $x_2 \in \mathcal{H}_2$, we interchangeably use the denotations $\{\!\!\{x_1, x_2\}\!\!\} = \begin{bmatrix} x_1 \\ x_2 \end{bmatrix} \in \mathcal{H}_1 \times \mathcal{H}_2$, where $\mathcal{H}_1 \times \mathcal{H}_2$ is the direct product of $\mathcal{H}_1$ and $\mathcal{H}_2$. The direct product of r Hilbert spaces $\mathcal{H}_i$ is denoted by $\prod_{i=1}^r \mathcal{H}_i$.

A sequence P is (h, q)-eventually periodic for some $h \in 0_+$ and $q \in 1_+$ if $P(h + iq + k) = P(h+k)$ for all $i, k \in 0_+$. A sequence P is q-eventually periodic for some $q \in 1_+$ if it is $(0, q)$-eventually periodic. A discrete-time linear time-varying (LTV) system is (h, q)-eventually periodic (q-periodic) if its state-space matrix sequences are (h, q)-eventually periodic (q-periodic). Given a positive definite matrix $\Xi \in \mathbb{S}^n$, the ellipsoid $\mathcal{E}(\Xi)$ is the set $\{x \in \mathbb{R}^n | \langle x, \Xi x \rangle \leq 1\}$.

2.2 Nominal model of an unmanned aircraft system

This section details the modeling of a *nominal* UAS–that is, how the UAS behavior is expressed when all uncertainties are absent. In Section 3.2, these equations will be revisited

to demonstrate how uncertainties inherent to the UAS are incorporated to obtain a better representation of the physical system. The UAS dynamic model and uncertainties in this work pertain to a small fixed-wing aircraft based on the radio-controlled Senior Telemaster Plus airframe from Hobby Express (94-inch wingspan) [53]. For simplicity, the equations in this subsection suppress the time dependence of each variable. Two reference frames are used to describe the aircraft state: the Earth-fixed inertial reference frame ($\mathcal{F}_I$) and the body-fixed reference frame ($\mathcal{F}_b$). The origin of the inertial frame is fixed on the local surface of the Earth and has components which point North, East, and downwards. The frame $\mathcal{F}_b$ has its origin affixed to the UAS center of gravity (CG) with components which point to the UAS nose, the right wingtip, and down.

For clarity, we adopt the following convention for denoting position and velocity vectors of frames either in the linear or angular sense. The attribute A of a frame $\mathcal{F}_c$ with respect to the frame $\mathcal{F}_d$, coordinatized in the frame $\mathcal{F}_e$, is expressed as A^e_{cd}. Hence, the position of the UAS body frame with respect to the inertial frame and coordinatized in the inertial frame is $P^I_{bI} = [x_I,\, y_I,\, z_I]^T$. The UAS altitude is $h = -z_I$.

The standard rotation matrix from a frame $\mathcal{F}_c$ to $\mathcal{F}_d$ is denoted by $\mathcal{R}^d_c$. We use Euler angles $\Lambda_{bI} = [\phi, \theta, \psi]^T$ to parameterize the rotation matrix $\mathcal{R}^I_b$ and $\mathcal{E}(\phi, \theta)$ as follows:

$$\mathcal{R}^I_b = \begin{bmatrix} c_\theta c_\psi & s_\phi s_\theta c_\psi - c_\phi s_\psi & c_\phi s_\theta c_\psi + s_\phi s_\psi \\ c_\theta s_\psi & s_\phi s_\theta s_\psi + c_\phi c_\psi & c_\phi s_\theta s_\psi - s_\phi c_\psi \\ -s_\theta & s_\phi c_\theta & c_\phi c_\theta \end{bmatrix}, \quad \mathcal{E}(\phi, \theta) = \begin{bmatrix} 1 & s_\phi s_\theta / c_\theta & c_\phi s_\theta / c_\theta \\ 0 & c_\phi & -s_\phi \\ 0 & s_\phi / c_\theta & c_\phi / c_\theta \end{bmatrix}$$

where $s_x := \sin(x)$ and $c_x := \cos(x)$. The aircraft angular and linear velocities are, respectively, $\Omega^b_{bI} = [p_b,\, q_b,\, r_b]^T$ and $V^b_{bI} = [u_b,\, v_b,\, w_b]^T$. The gravitational force in $\mathcal{F}_b$ is $G(\phi, \theta) := mg \begin{bmatrix} -s_\theta & s_\phi c_\theta & c_\phi c_\theta \end{bmatrix}^T$ where $g = 9.807\,\mathrm{m/s^2}$ and the UAS mass is $m = 5.71\,\mathrm{kg}$. With a slight abuse of notation, the linear velocity relative to the wind is $V^b_{bw} = V^b_{bI} - V^b_{wI}$,

where $V_{wI}^b := [u_w,\, v_w,\, w_w]^T$ denotes the wind velocity coordinatized in the body frame. The airspeed is defined as $V_a := \sqrt{(V_{bw}^b)^T V_{bw}^b}$. In this work, the aircraft actuation is digitally controlled; hence, commands for the elevator (δ_E^c), ailerons (δ_A^c), rudder (δ_R^c), and throttle (δ_T^c) are pulse-width-modulated (PWM) signals. The realized actuation (or the commanded actuation post actuator dynamics) is denoted by $\delta = [\delta_E, \delta_A, \delta_R, \delta_T]^T$. The propulsive and aerodynamic moments and forces are $M(V_{bw}^b, \Omega_{bI}^b, \delta)$ and $F(V_{bw}^b, \Omega_{bI}^b, \delta)$, respectively. The UAS inertia matrix is $J = \mathrm{diag}(1.32, 1.57, 1.87)\,\mathrm{kg}\cdot\mathrm{m}^2$. Therefore, the 6-DOF equations of motion for the aircraft are

$$\dot{\Omega}_{bI}^b = J^{-1}[-(\Omega_{bI}^b \times J\Omega_{bI}^b) + M(V_{bw}^b, \Omega_{bI}^b, \delta)] \tag{2.1}$$

$$\dot{V}_{bI}^b = -\Omega_{bI}^b \times V_{bI}^b + [G(\phi,\theta) + F(V_{bw}^b, \Omega_{bI}^b, \delta)]/m \tag{2.2}$$

$$\dot{\Lambda}_{bI} = \mathcal{E}(\phi,\theta)\Omega_{bI}^b \tag{2.3}$$

$$\dot{P}_{bI}^I = \mathcal{R}_b^I V_{bI}^b. \tag{2.4}$$

If the true aircraft CG is offset from the nominal aircraft CG by the position vector $\Delta_{cg} = [\Delta_x, \Delta_y, \Delta_z]^T$ (coordinatized in $\mathcal{F}_b$), then [54] shows that (2.1) and (2.2) are replaced with

$$\begin{bmatrix} \dot{\Omega}_{bI}^b \\ \dot{V}_{bI}^b \end{bmatrix} = \begin{bmatrix} J & \Delta_{\mathrm{m}} \\ -\Delta_{\mathrm{m}} & mI_3 \end{bmatrix}^{-1} \left(\begin{bmatrix} M(V_{bw}^b, \Omega_{bI}^b, \delta) \\ F(V_{bw}^b, \Omega_{bI}^b, \delta) + G \end{bmatrix} - \begin{bmatrix} (\Omega_{bI}^b)^\times J - (V_{bI}^b)^\times \Delta_{\mathrm{m}} & (\Omega_{bI}^b)^\times \Delta_{\mathrm{m}} \\ -(\Omega_{bI}^b)^\times \Delta_{\mathrm{m}} & (\Omega_{bI}^b)^\times \end{bmatrix} \begin{bmatrix} \Omega_{bI}^b \\ V_{bI}^b \end{bmatrix} \right) \tag{2.5}$$

$$\text{where } \Delta_{\mathrm{m}} = m\Delta_{cg}^\times.$$

Defining T to be the propulsive force (or thrust) imparted by the propeller, the aerodynamic moments and forces in (2.1) and (2.2) are respectively defined as $M = [M_l, M_m, M_n]^T$ and $F = [F_x + T, F_y, F_z]^T$ (notationally dropping the dependence on V_{bw}^b, Ω_{bI}^b, and δ for simplicity). The propulsive force is determined by a series of lookup tables. First, a mapping $\omega_m =$

Table 2.1: Lookup table for $\omega_m = RPM(\delta_T)$

δ_T (ms)	0	0.08	0.16	0.19	0.22	0.29	0.32	0.35	0.38
RPM $\times 10^3$	0	0	1.59	1.89	2.16	2.85	3.18	3.42	3.75

δ_T (ms)	0.41	0.44	0.48	0.54	0.57	0.60	0.63	0.69	1.0
RPM $\times 10^3$	4.14	4.53	4.98	5.58	5.91	6.24	6.48	6.66	6.66

$RPM(\delta_T)$ from δ_T to the propeller motor rotations per minute (RPM) is experimentally determined and shown in Table 2.1. Second, a lookup table $\mathbb{T} = f_p(V_{bw}^b, \omega_m)$ from the airspeed and propeller RPM to the thrust is obtained via vortex theory. The propeller used in this dissertation is a 17×10 carbon fiber propeller from APC, and the associated lookup table can be found in [55]. Hence, we have $T = f_p(V_{bw}^b, RPM(\delta_T))$.

The remaining terms of the aircraft forces and moments have the form

$$
\begin{aligned}
F_i &= 0.5\rho C_i V_a^2 S_a, \text{ for } i = x, y, z \\
M_m &= 0.5\rho C_m V_a^2 S_a \underline{c} \\
M_j &= 0.5\rho C_j V_a^2 S_a \underline{b}, \text{ for } j = l, n
\end{aligned}
$$

where the dependence of $C_{(\cdot)}$ on V_{bw}^b, Ω_{bI}^b, and δ is not annotated for simplicity, $\rho = 1.3302$ kg/m^2 is the density of the air, $C_{(\cdot)}$ is an aerodynamic coefficient, $S_a = 0.89$ m^2 is the UAS wing area, $\underline{c} = 0.36$ m denotes the mean aerodynamic chord, and $\underline{b} = 2.39$ m is the wingspan of the UAS. Given a structure for the aerodynamic coefficient model, the equation error and output error methods are used to obtain the subcoefficients that are part of the nominal nonlinear aerodynamic coefficient model. This is done by comparing forces and moments between measurements from flight data and outputs from the postulated aerodynamic model

Table 2.2: Aero model values and uncertainty bounds

Term	Value	Term	Value	Term	Value
C_{x_0}	-0.1303	C_{z_0}	-0.5892	C_{m_0}	-0.1078
C_{x_α}	-0.0224	C_{z_α}	-3.8864	C_{m_α}	-0.6969
$C_{x_{\delta_T}}$	0.1028	$C_{z_{\delta_E}}$	0.3061	$C_{m_{\delta_E}}$	0.9405
C_{x_T}	-0.0195	C_{z_T}	1.4463	C_{m_q}	-11.8094
		C_{z_q}	-1.9859		
C_{y_0}	0.0165	C_{l_0}	0.0019	C_{n_0}	-0.0015
C_{y_β}	-0.3816	C_{l_β}	-0.0582	C_{n_β}	0.0451
$C_{y_{\delta_A}}$	-0.0413	$C_{l_{\delta_A}}$	0.1619	$C_{n_{\delta_A}}$	-0.0169
$C_{y_{\delta_R}}$	-0.1196	$C_{l_{\delta_R}}$	-0.0128	$C_{n_{\mu_R}}$	0.0555
C_{y_p}	0.1445	C_{l_p}	-0.4137	C_{n_p}	-0.0291
C_{y_r}	0.1441	C_{l_r}	0.1815	C_{n_r}	-0.0781

[56]. We utilize the following aerodynamic model structure:

$$
\begin{aligned}
C_x &= C_{x_0}+C_{x_\alpha}\alpha+C_{x_{\delta_T}}\delta_T+\frac{C_{x_T}2T}{\rho S_a V_a^2} \\
C_y &= C_{y_0}+C_{y_\beta}\beta+C_{y_{\delta_A}}\delta_A+C_{y_{\delta_R}}\delta_R+\frac{(C_{y_p}p+C_{y_r}r)\underline{b}}{2V_a} \\
C_z &= C_{z_0}+C_{z_\alpha}\alpha+C_{z_{\delta_E}}\delta_E+\frac{C_{z_q}q\underline{c}}{2V_a}+\frac{C_{z_T}2T}{\rho S_a V_a^2} \\
C_l &= C_{l_0}+C_{l_\beta}\beta+C_{l_{\delta_A}}\delta_A+C_{l_{\delta_R}}\delta_R+\frac{(C_{l_p}p+C_{l_r}r)\underline{b}}{2V_a} \\
C_m &= C_{m_0}+C_{m_\alpha}\alpha+C_{m_{\delta_E}}\delta_E+\frac{C_{m_q}q\underline{c}}{2V_a} \\
C_n &= C_{n_0}+C_{n_\beta}\beta+C_{n_{\delta_A}}\delta_A+C_{n_{\delta_R}}\delta_R+\frac{(C_{n_p}p+C_{n_r}r)\underline{b}}{2V_a}.
\end{aligned}
$$

The value for each aerodynamic subcoefficient is displayed in Table 2.2.

Three servomotors manipulate the control surfaces of the aircraft, where each actuator is nominally modeled by

$$G^c_{srv}(s) = \omega^2_{ns}/(s^2 + 2\zeta_s\omega_{ns}s + \omega^2_{ns}). \tag{2.6}$$

For these servomotors, the damping ratio and natural frequency are experimentally estimated

as $\zeta_s = 0.67$ and $\omega_{ns} = 13.7$ rad/s by measuring the servomotor frequency response [2]. The actuator states are denoted by x_a. Since the thrust model is based off lookup tables, the propeller motor is assumed to have no dynamics. The propeller motor dynamics will later be incorporated in Section 3.2 as a dynamic uncertainty.

In summary, the nominal nonlinear dynamics of the Telemaster are modeled by the equations

$$\dot{x} = f(x, d, u), \quad e = g(x, d, u), \quad y = h(x, d, u) \tag{2.7}$$

where $x := [(\Omega_{bI}^b)^T, (V_{bI}^b)^T, \Lambda_{bI}^T, (P_{bI}^v)^T, x_a^T]^T$, $d := [(V_{wI}^b)^T, \eta^T]^T$ is the exogenous disturbance composed of wind velocities and sensor noise η, $u = [u_E, u_A, u_R, u_T]^T := \delta^c$ is the control input, e is the performance output, and y is the sensor output. The state function $f(\cdot)$ is defined by (2.1), (2.2), (2.3), and (2.4). The sensor output function is defined as

$$\begin{aligned} h(x, d, u) &= \begin{bmatrix} p_b, & q_b, & r_b, & V_a, & \phi, & \theta, & \psi, & X, & Y, & z \end{bmatrix}^T + W_\eta \eta \\ \eta &:= \begin{bmatrix} \eta_p, & \eta_q, & \eta_r, & \eta_V, & \eta_\phi, & \eta_\theta, & \eta_\psi, & \eta_X, & \eta_Y, & \eta_z \end{bmatrix}^T \\ W_\eta &:= \mathrm{diag}(0.01 I_3, 2, 0.01 I_3, 2 I_3) \end{aligned} \tag{2.8}$$

where W_η is a weighting matrix expressing the standard deviations of the measurement noise. The performance output function is defined as

$$\begin{aligned} g(x, d, u) &= W_e [x^T, u^T]^T \\ W_e &:= \mathrm{diag}(c_p, c_q, c_r, c_{V_a}, c_\phi, c_\theta, c_\psi, c_X, c_Y, c_z, c_{\delta_E}, c_{\delta_A}, c_{\delta_R}, c_{\delta_T}). \end{aligned} \tag{2.9}$$

Though the previous derivations are in continuous time, the sequel synthesizes controllers and analyzes the system in discrete time. To conduct such synthesis and analysis, the equations

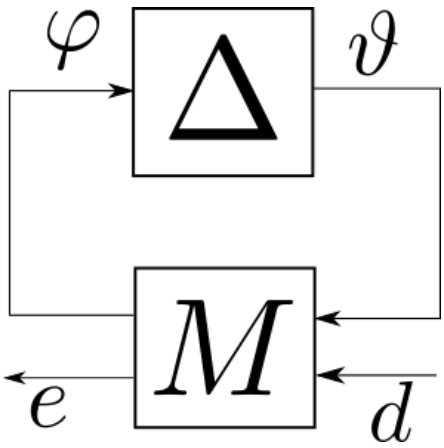

Figure 2.1: The interconnection (M, Δ)

of motion will later be discretized using a sampling time of $\tau = 40$ ms.

2.3 Integral quadratic constraint theory

To investigate the robust stability and performance of an uncertain UAS, we first introduce some preliminary notions of robustness. Consider a causal linear operator M bounded on ℓ_2 and a set $\mathbf{\Delta}$ of causal operators $\Delta : \ell_{2e} \to \ell_{2e}$ that are bounded on ℓ_2. The interconnection (M, Δ) is depicted in Fig. 2.1 and satisfies the equations

$$\begin{bmatrix} \varphi \\ e \end{bmatrix} = \begin{bmatrix} M_{11} & M_{12} \\ M_{21} & M_{22} \end{bmatrix} \begin{bmatrix} \vartheta \\ d \end{bmatrix} \tag{2.10}$$
$$\vartheta = \Delta\varphi, \quad \text{for } \Delta \in \mathbf{\Delta}.$$

The uncertain system $(M, \mathbf{\Delta})$ is robustly well-posed if $I - M_{11}\Delta$ has an algebraic causal inverse on ℓ_{2e} for all $\Delta \in \mathbf{\Delta}$. The uncertain system is robustly stable if (M, Δ) is well-posed and $(I - M_{11}\Delta)^{-1}$ is a bounded operator on ℓ_2 for all $\Delta \in \mathbf{\Delta}$. The uncertain system has a robust ℓ_2-gain performance level of γ if it is robustly stable and $\|(M, \Delta)\|_{\ell_2 \to \ell_2} < \gamma$

for all $\Delta \in \mathbf{\Delta}$. Given a subset $\mathcal{D} \subseteq \ell_2$, the uncertain system has a robust $\mathcal{D}$-to-ℓ_2-gain performance level of γ if it is robustly stable and $\|(M,\Delta)\|_{\mathcal{D}\to\ell_2} < \gamma$ for all $\Delta \in \mathbf{\Delta}$. The robust $\mathcal{D}$-to-ℓ_2-gain performance level is the pivotal measure used herein. This dissertation parsimoniously refers to it as "robust performance." Chapters 3 and 4 demonstrate how the robust performance of the uncertain UAS provides a useful measure to optimize when tuning controllers and a consistent and valuable prediction on the ultimate performance of the physical UAS. IQC analysis is critical in obtaining this robust performance.

Though we only briefly present the IQC analysis theorem used in Chapters 3 and 4, interested readers can find more detailed discussions in [11, 20, 31, 57]. Chapter 5 provides a more in-depth treatment and a novel robustness analysis theorem based on IQC theory. The set $\mathbf{\Delta}$ satisfies the IQC defined by the IQC multiplier $\hat{\Pi} = \hat{\Pi}^{\sim} = \begin{bmatrix} \hat{\Pi}_{11} & \hat{\Pi}_{12} \\ \hat{\Pi}_{12}^{\sim} & \hat{\Pi}_{22} \end{bmatrix} \in \mathcal{RL}_\infty$ if, for all $\Delta \in \mathbf{\Delta}$, $\varphi \in \ell_2$, $\vartheta = \Delta\varphi$,

$$\int_{-\pi}^{\pi} \begin{bmatrix} \hat{\varphi}(e^{j\omega}) \\ \hat{\vartheta}(e^{j\omega}) \end{bmatrix}^* \begin{bmatrix} \hat{\Pi}_{11}(e^{j\omega}) & \hat{\Pi}_{12}(e^{j\omega}) \\ \hat{\Pi}_{12}^{\sim}(e^{j\omega}) & \hat{\Pi}_{22}(e^{j\omega}) \end{bmatrix} \begin{bmatrix} \hat{\varphi}(e^{j\omega}) \\ \hat{\vartheta}(e^{j\omega}) \end{bmatrix} d\omega \geq 0. \tag{2.11}$$

We further assume that $\hat{\Pi}_{11} \succeq 0$ and $\hat{\Pi}_{22} \preceq 0$. $\hat{\Pi}$ can be factorized as $\hat{\Pi} = \hat{\Psi}^{\sim} S \hat{\Psi}$ with the partitioning

$$\begin{bmatrix} \hat{\Pi}_{11} & \hat{\Pi}_{12} \\ \hat{\Pi}_{12}^{\sim} & \hat{\Pi}_{22} \end{bmatrix} = \begin{bmatrix} \hat{\Psi}_{11} & \hat{\Psi}_{12} \\ \hat{\Psi}_{21} & \hat{\Psi}_{22} \end{bmatrix}^{\sim} \begin{bmatrix} S_{11} & S_{12} \\ S_{12}^T & S_{22} \end{bmatrix} \begin{bmatrix} \hat{\Psi}_{11} & \hat{\Psi}_{12} \\ \hat{\Psi}_{21} & \hat{\Psi}_{22} \end{bmatrix}$$

where $\hat{\Psi} \in \mathcal{RH}_\infty$ and S is a real symmetric matrix. The subset $\mathcal{D} \subseteq \ell_2$ satisfies the IQC defined by the signal IQC multiplier $\hat{\Phi} = \hat{\Phi}^{\sim} \in \mathcal{RL}_\infty$ if, for all $d \in \mathcal{D}$,

$$\int_{-\pi}^{\pi} \hat{d}(e^{j\omega})^* \hat{\Phi}(e^{j\omega}) \hat{d}(e^{j\omega}) d\omega \geq 0. \tag{2.12}$$

$\hat{\Phi}$ can be factorized as $\hat{\Phi} = \hat{\Theta}^{\sim} R \hat{\Theta}$, where $\hat{\Theta} \in \mathcal{RH}_\infty$ and R is a real symmetric matrix. The following is a variant of the theorem in [11] (see [39]).

Theorem 2.1 ([11]). *The uncertain system* (3.2) *has a robust $\mathcal{D}$-to-ℓ_2-gain performance level of γ if $(M, \mathbf{\Delta})$ is well-posed, $\mathbf{\Delta}$ satisfies the IQC defined by $\hat{\Psi}^{\sim} S \hat{\Psi}$, $\mathcal{D}$ satisfies the signal IQC defined by $\hat{\Theta}^{\sim} R \hat{\Theta}$, and there exists an $\epsilon > 0$ such that the following holds for all $\omega \in [-\pi, \pi]$:*

$$\begin{bmatrix} \hat{M}(e^{j\omega}) \\ I \end{bmatrix}^* \hat{\tilde{\Psi}}(e^{j\omega})^* \tilde{S} \hat{\tilde{\Psi}}(e^{j\omega}) \begin{bmatrix} \hat{M}(e^{j\omega}) \\ I \end{bmatrix} \preceq -\epsilon I, \ \textit{where} \tag{2.13}$$

$$\tilde{S} := \begin{bmatrix} \mathrm{diag}(S_{11}, I) & \mathrm{diag}(S_{12}, 0) \\ \mathrm{diag}(S_{12}^T, 0) & \mathrm{diag}(S_{22}, R, -\gamma^2 I) \end{bmatrix}$$

$$\hat{\tilde{\Psi}} := \begin{bmatrix} \mathrm{diag}(\hat{\Psi}_{11}, I) & \mathrm{diag}(\hat{\Psi}_{12}, 0) \\ \mathrm{diag}(\hat{\Psi}_{21}, 0) & \mathrm{diag}(\hat{\Psi}_{22}, [\hat{\Theta}^{\sim} \ \ I]^{\sim}) \end{bmatrix}.$$

By selecting $\hat{\Psi}$ and $\hat{\Theta}$ as known transfer functions in $\mathcal{RH}_\infty$, the frequency-domain inequality (2.13) can be equivalently expressed as a linear matrix inequality (LMI) through the use of the Kalman-Yakubovich-Popov (KYP) Lemma [58]. Specifically, if we define $\mathcal{D} + \mathcal{C}(zI - \mathcal{A})^{-1}\mathcal{B} = \hat{\tilde{\Psi}}(z) \ [\hat{M}(z)^* \ I]^*$, then finding the robust performance for the uncertain system is achieved by solving the following semidefinite program (SDP):

$$\begin{aligned} &\text{minimize } \gamma^2 \\ &\text{subject to } P = P^T \\ &\begin{bmatrix} \mathcal{A}^T P \mathcal{A} - P + \mathcal{C}^T \tilde{S} \mathcal{C} & \mathcal{A}^T P \mathcal{B} + \mathcal{C}^T \tilde{S} \mathcal{D} \\ \mathcal{B}^T P \mathcal{A} + \mathcal{D}^T \tilde{S} \mathcal{C} & \mathcal{B}^T P \mathcal{B} + \mathcal{D}^T \tilde{S} \mathcal{D} \end{bmatrix} \prec 0. \end{aligned} \tag{2.14}$$

The parameterizations we use for the IQC multipliers $\hat{\Psi}^{\sim} S \hat{\Psi}$ employed herein are extensively exposited in [20]. $\hat{\Psi}$ is defined by an appropriate structure and basis function $\hat{B}$, while S consists of decision variables satisfying convex constraints. The basis function

$$\hat{B}(z) = \left[1, \frac{1}{z-\lambda}, \ldots, \frac{1}{(z-\lambda)^{b-1}}\right]^T \tag{2.15}$$

is determined by its pole location λ and basis length b. For clarity, we include the parameterizations and constraints for each considered multiplier in Tables 2.3 and 2.4. In the sequel, such multipliers will be characterizing (possibly nonlinear and/or time-varying) norm-bounded (NB) uncertainties, static LTV (SLTV) uncertainties, static LTI (SLTI) uncertainties, dynamic LTI (DLTI) uncertainties, and rate-bounded SLTV (RB-SLTV) uncertainties.

This work also uses signal IQCs to characterize the disturbance signals. Though novel time-varying signal IQCs will be given in Chapter 5, the work in Chapters 3 and 4 relies on two signal IQCs inspired by [17]. These two signal IQCs were originally derived for continuous-time systems, and this work derives their discrete-time counterparts. The "banded white" subset $\mathcal{D}_w \subset \ell_2^1$ consists of signals that satisfy

$$|\hat{d}(e^{j\omega})|^2 = \begin{cases} \frac{\pi}{\omega_0}\|d\|^2, & |\omega| \leq \omega_0 \\ 0, & |\omega| \in (\omega_0, \pi] \end{cases} \tag{2.16}$$

where $\omega_0 \in (0, \pi)$; for $\omega_0 = \pi$, $|\hat{d}(e^{j\omega})| = \|d\|$ for all $|\omega| \leq \pi$.

Lemma 2.2. *The signal set $\mathcal{D}_w$ satisfies the signal IQC defined by $\hat{\Phi} = \hat{\Phi}^{\sim} \in \mathcal{RL}_\infty^{1\times 1}$ if*

$$\int_{-\omega_0}^{\omega_0} \hat{\Phi}(e^{j\omega}) d\omega \geq 0. \tag{2.17}$$

Furthermore, such a $\hat{\Phi}$ can be constructed by

$$\hat{\Phi}(z) = \underbrace{\begin{bmatrix} \frac{1}{z+a_1} \\ \vdots \\ \frac{1}{z+a_N} \\ 1 \end{bmatrix}^{\sim}}_{\hat{\Theta}^{\sim}(z)} \underbrace{\begin{bmatrix} 0 & \dots & 0 & x_1 \\ \vdots & \ddots & \vdots & \vdots \\ 0 & \dots & 0 & x_N \\ x_1 & \dots & x_N & 2x_0 \end{bmatrix}}_{R} \underbrace{\begin{bmatrix} \frac{1}{z+a_1} \\ \vdots \\ \frac{1}{z+a_N} \\ 1 \end{bmatrix}}_{\hat{\Theta}(z)}, \text{ where } a_i \in (-1,1) \text{ and} \tag{2.18}$$

$$\omega_0 x_0 + \sum_{i=1}^{N} \frac{x_i}{a_i} \tan^{-1}\left(\frac{a_i \sin\omega_0}{1 + a_i \cos\omega_0}\right) \geq 0. \tag{2.19}$$

Proof. To prove the first part of the lemma, we see that

$$\begin{aligned} \int_{-\pi}^{\pi} \hat{d}(e^{j\omega})^* \hat{\Phi}(e^{j\omega}) \hat{d}(e^{j\omega}) d\omega &= \int_{-\pi}^{\pi} \hat{d}(e^{j\omega})^* \hat{d}(e^{j\omega}) \hat{\Phi}(e^{j\omega}) d\omega \\ &= \frac{\pi}{\omega_0} \|d\|^2 \int_{-\omega_0}^{\omega_0} \hat{\Phi}(e^{j\omega}) d\omega \geq 0 \end{aligned} \tag{2.20}$$

where the last inequality arises from (2.17) and the previous equality is due to (2.16). To prove the last part of the lemma, define the parameterization $\hat{\Phi} = \hat{Y} + \hat{Y}^{\sim}$, where $\hat{Y}(z) = x_0 + \sum_{i=1}^{N} \frac{x_i}{z + a_i}$. Therefore

$$\begin{aligned} \int_{-\omega_0}^{\omega_0} \hat{\Phi}(e^{j\omega}) d\omega &= \int_{-\omega_0}^{\omega_0} 2x_0 + \sum_{i=1}^{N} \frac{x_i}{e^{j\omega} + a_i} + \sum_{i=1}^{N} \frac{x_i}{e^{-j\omega} + a_i} d\omega \\ &= 4\omega_0 x_0 + \sum_{i=1}^{N} x_i \int_{-\omega_0}^{\omega_0} \frac{1}{e^{j\omega} + a_i} + \frac{1}{e^{-j\omega} + a_i} d\omega \\ &= 4\omega_0 x_0 + \sum_{i=1}^{N} \left[\frac{2x_i}{j a_i} (\ln(a_i e^{j\omega} + 1) - \ln(a_i e^{-j\omega} + 1))\right] \\ &= 4\omega_0 x_0 + 4 \sum_{i=1}^{N} \frac{x_i}{a_i} \tan^{-1}\left(\frac{a_i \sin\omega_0}{1 + a_i \cos\omega_0}\right) \end{aligned} \tag{2.21}$$

where the last equality can be obtained via standard trigonometric identities and the defi-

nition of the complex logarithm. Hence, if (2.19) holds with $a_i \in (-1, 1)$, then (2.17) holds, thereby concluding the proof. □

A similar signal IQC multiplier $\hat{\Phi}_{n_d} \in \mathcal{RL}^{n_d \times n_d}$ may be defined by modifying $\hat{\Theta}(z)$ to be $[\frac{1}{z+a_1}I, \ldots, \frac{1}{z+a_N}I, I]^T$, modifying R in (2.18) by replacing every scalar x_i with $X_i \in \mathbb{R}^{n_d \times n_d}$, and modifying the constraint (2.19) by replacing every instance of x_i with trace(X_i). By doing so, the constraint (2.17) is modified by replacing $\hat{\Phi}(e^{j\omega})$ with trace$(\hat{\Phi}(e^{j\omega})$, and the disturbance signals satisfy a so-called "average" signal IQC (see [17]). This notion is not immediately useful, as the IQC analysis procedure would instead produce a notion of the uncertain system's worst-case "average" performance. However, in Section 3.4.1 we use this multiplier to simplify the IQC analysis SDP while tuning controllers.

We also define "banded" signals $d \in \mathcal{D}_b \subset \ell_2$, which satisfy

$$\text{supp}(\hat{d}(e^{j\omega})) \subseteq [-\omega_b, -\omega_a] \cup [\omega_a, \omega_b] \tag{2.22}$$

where $0 \leq \omega_a < \omega_b \leq \pi$. The set $\mathcal{D}_b$ satisfies the signal IQC (2.12) for multipliers $\hat{\Phi} \in \hat{\Phi}_b \subset \mathcal{L}_\infty$ subject to

$$\hat{\Phi}(e^{j\omega}) = \begin{cases} 0, & \omega \in [-\omega_b, -\omega_a] \cup [\omega_a, \omega_b] \\ -\chi I, & \text{otherwise} \end{cases} \tag{2.23}$$

where $\chi \gg 0$. Rational approximations for $\hat{\Phi} \in \hat{\Phi}_b$ can be obtained with appropriate low/high/band-pass filters. In this work, we consider signals $d \in \mathcal{D}_b$ where $\text{supp}(\hat{d}(e^{j\omega})) = [-\omega_b, \omega_b]$. An appropriate approximation for $\hat{\Phi} \in \hat{\Phi}_b$ is obtained by constructing a Butterworth low-pass filter (LPF) $\hat{F}_{\tilde{\omega}_b}$ having a cut-off frequency $\tilde{\omega}_b > \omega_b$. The MATLAB command `butter` is useful in this regard. Defining a *close* rational approximation $\hat{F}_{\tilde{\omega}_b}$ to (2.23) requires placing the filter cut-off frequency $\tilde{\omega}_b$ further out than ω_b (see [57] for further discussion). The construction of the multipliers $\hat{\Phi} \in \hat{\Phi}_b$ is given in Tables 2.3 and 2.4.

Table 2.3: Parameterizations of multipliers for uncertainties and signal sets

Uncertainty or Signal	$\hat{\Psi}(z)$ or $\hat{\Theta}(z)$	S or R
NB $\vartheta = \Delta(\varphi)$ $\|\Delta\|_{\ell_2\to\ell_2} \le \alpha$	$\begin{bmatrix} I_{n_\varphi} & 0 \\ 0 & I_{n_\vartheta} \end{bmatrix}$	$\begin{bmatrix} \alpha^2 x I_{n_\varphi} & 0 \\ 0 & -x I_{n_\vartheta} \end{bmatrix}$
DLTI $\hat{\vartheta}(z) = \hat{\Delta}(z)\hat{\varphi}(z)$ $\|\hat{\Delta}\|_\infty \le \alpha$	$\begin{bmatrix} \hat{B}(z) \otimes I_{n_\varphi} & 0 \\ 0 & \hat{B}(z) \otimes I_{n_\vartheta} \end{bmatrix}$	$\begin{bmatrix} \alpha^2 X \otimes I_{n_\varphi} & 0 \\ 0 & -X \otimes I_{n_\vartheta} \end{bmatrix}$
SLTI $\vartheta(k) = \Delta\varphi(k)$ $\|\Delta\| \le \alpha$	$\begin{bmatrix} \hat{B}(z) & 0 \\ 0 & \hat{B}(z) \end{bmatrix} \otimes I_{n_\varphi}$	$\begin{bmatrix} \alpha^2 X & Y \\ Y^T & -X \end{bmatrix}$
SLTV $\vartheta(k) = \Delta(k)\varphi(k)$ $\|\Delta(k)\| \le \alpha$	$\begin{bmatrix} I_{n_\varphi} & 0 \\ 0 & I_{n_\varphi} \end{bmatrix}$	$\begin{bmatrix} \alpha^2 X & Y \\ Y^T & -X \end{bmatrix}$
RB-SLTV $\vartheta(k) = \Delta(k)\varphi(k)$ $\|\Delta(k)\| \le \alpha$ $\|\Delta(k{+}1){-}\Delta(k)\| \le \beta$	$\left[\begin{array}{cc\|ccc} A_B & 0 & B_B & 0 & 0 \\ 0 & A_B & 0 & B_B & I_{b-1} \\ \hline C_B & 0 & D_B & 0 & 0 \\ A_B & 0 & B_B & 0 & 0 \\ 0 & C_B & 0 & D_B & 0 \\ 0 & 0 & 0 & 0 & I_{b-1} \end{array}\right] \otimes I_{n_\varphi}$	$\begin{bmatrix} \alpha^2 X_\alpha & 0 & Y_\alpha & 0 \\ 0 & \beta^2 X_\beta & 0 & Y_\beta \\ Y_\alpha^T & 0 & -X_\alpha & 0 \\ 0 & Y_\beta^T & 0 & -X_\beta \end{bmatrix}$
$\mathcal{D}_w \subseteq \ell_2^1$ See (2.16)	$\left[\frac{1}{z+a_1}, \dots, \frac{1}{z+a_N}, 1\right]^T$ $a_i \in (-1, 1)$	$\begin{bmatrix} 0 & C_w^T \\ C_w & 2x_0 \end{bmatrix}$ $C_w := [x_1, \dots, x_N]$
$\mathcal{D}_b \subseteq \ell_2^{n_d}$ See (2.22)	$\begin{bmatrix} \hat{F}_{\tilde{\omega}_b}(z) I_{n_d} \\ I_{n_d} \end{bmatrix}$ $\hat{F}_{\tilde{\omega}_b}$ is an LPF constructed by `butter`	$\begin{bmatrix} x_b I_{n_d} & 0 \\ 0 & -d_b I_{n_d} \end{bmatrix}$

Table 2.4: Constraints on multipliers for uncertainties and signal sets

Uncertainty or Signal	Constraints
NB	$x \ge 0$
DLTI	$X = X^T \succeq 0$
SLTI	$X = X^T \succeq 0, \quad Y = -Y^T$
SLTV	$X = X^T \succeq 0, \quad Y = -Y^T$
RB-SLTV	$X_\alpha = X_\alpha^T \succeq 0, \quad X_\beta = X_\beta^T \succeq 0, \quad Y_\alpha = -Y_\alpha^T, \quad Y_\beta = -Y_\beta^T$
$\mathcal{D}_w$	$\omega_0 x_0 + \sum_{i=1}^N \frac{x_i}{a_i} \tan^{-1}\left(\frac{a_i \sin\omega_0}{1 + a_i \cos\omega_0}\right) \ge 0$
$\mathcal{D}_b$	$x_b \ge 0, \ d_b \ge 0, \ x_b \lvert\hat{F}_{\tilde{\omega}_b}(e^{j\omega_b \tau})\rvert^2 - d_b \ge 0$

Chapter 3

Validation of an IQC-based uncertain UAS framework

This chapter details the implementation of an uncertain UAS framework originally derived in [12] on a Senior Telemaster Plus (94-inch wingspan) aircraft. Section 3.1 discusses the controller synthesis procedure we employ. In Section 3.2 we detail the uncertain UAS framework that is utilized throughout Chapters 3 and 4. We enhance the framework in Section 3.3 by developing a controller tuning routine which relies on IQC analysis to improve the robustness of the controlled UAS. In Section 3.4 we demonstrate the validity of this framework by comparing the predictions afforded from this framework with those obtained in simulation and with observations from flight tests. The work from [13] constitutes the results of this chapter.

3.1 Controller synthesis

To synthesize a linear controller for the UAS, we first select a trim point about which (2.7) is linearized. In this chapter we analyze the performance of the UAS flying a level right-turning circle with a 100m radius. This pertains to a trim point of

$$(\Omega_{bI}^{b})^{\star} = [-0.0005,\ 0.0288,\ 0.147]^{T} \text{ rad/s}$$

$$(V_{bI}^{b})^{\star} = [15,\ 0,\ 0.1]^{T} \text{ m/s}$$

$$(\Lambda_{bI})^\star = [0.193,\ 0.035,\ 0]\ \text{rad}$$

$$(\delta^c)^\star = [0.122,\ -0.022,\ 0.037,\ 0.474]\ \text{ms PWM}.$$

By linearizing (2.7) about $x^\star$ and $u^\star$ and discretizing via Euler's method with the sampling time $\tau = 0.04\,\text{s}$, we obtain a linear, discrete-time, state-space model G_{nom} of the UAS defined by the equations

$$\begin{bmatrix} \bar{x}(k+1) \\ e(k) \\ \bar{y}(k) \end{bmatrix} = \begin{bmatrix} A & B_1 & B_2 \\ C_1 & D_{11} & D_{12} \\ C_2 & D_{21} & 0 \end{bmatrix} \begin{bmatrix} \bar{x}(k) \\ d(k) \\ \bar{u}(k) \end{bmatrix}, \quad \bar{x}(0) = 0. \tag{3.1}$$

We can then solve for an LTI $\mathcal{H}_\infty$ controller K defined as

$$\begin{bmatrix} x^K(k+1) \\ \bar{u}(k) \end{bmatrix} = \begin{bmatrix} A^K & B^K \\ C^K & D^K \end{bmatrix} \begin{bmatrix} x^K(k) \\ \bar{y}(k) \end{bmatrix}, \ x^K(0) = 0$$

by following the procedure set forth in [59] and Section 2.2.2 of [60]. This controller is used to obtain the nominal closed-loop system M_{nom}

3.2 The uncertain UAS

Although the model M_{nom} is useful in control design and analysis, it is quickly apparent that there are many discrepancies between its dynamics and the true behavior of the controlled UAS. We will generally refer to these discrepancies as model uncertainties. The genesis of these uncertainties differs. For example, the nonlinear dynamics in (2.1), (2.2), (2.3), and (2.4) are known and *purposefully* ignored in (3.1) to simplify the controller design. Alternatively, uncertainties occur in the aerodynamic model because model fitting fails to perfectly express physical phenomena. Regardless of how these uncertainties accrue, the

uncertain UAS framework proposed in [13] is a flexible, modular, and powerful method for reinserting the effect of these uncertainties on the UAS performance. Notably, this framework does not capture *all* uncertainties, but it allows systems engineers to incorporate a large number of uncertainties in the linear model, obtaining a much better representation of the physical UAS.

The uncertainties considered in this work address (1) aerodynamic model uncertainties, (2) actuator model uncertainties, (3) actuator saturation, and (4) UAS nonlinear dynamics. Each individual uncertainty is incorporated into a subsystem of the UAS and the subsystems are connected together as shown in Fig. 3.1, producing the closed-loop LFT (M, Δ), where Δ is a structured uncertainty. By setting $\Delta = 0$, the LFT (M, Δ) recovers the nominal closed-loop UAS linearized about trim. When Δ is allowed to vary within some predefined set $\mathbf{\Delta}$, analysis on (M, Δ) applies to the uncertain UAS operating about its specified trim point. Hence, the uncertain UAS is modeled as

$$\begin{bmatrix} \varphi \\ e \end{bmatrix} = \begin{bmatrix} M_{11} & M_{12} \\ M_{21} & M_{22} \end{bmatrix} \begin{bmatrix} \vartheta \\ d \end{bmatrix} \tag{3.2}$$
$$\vartheta = \Delta\varphi, \quad \text{for } \Delta \in \mathbf{\Delta}.$$

3.2.1 Aerodynamic uncertainties

Aerodynamic model uncertainties are characterized by six RB-SLTV perturbations: Δ_{C_x}, Δ_{C_y}, Δ_{C_z}, Δ_{C_l}, Δ_{C_m}, and Δ_{C_n}. The operators Δ_{C_i} represent uncertainties in the aerodynamic coefficients C_i and are added to the nominal aerodynamic coefficient model detailed in Section 2.2 (i.e., $C_i = C_i^{\text{nom}}(V_{bw}^b, \Omega_{bI}^b, \delta) + \Delta_{C_i}$). This treatment of aerodynamic uncertainty covers both the errors in the estimation of the parameters for the aerodynamic coefficient model and the inexactness of the postulated structure of each aerodynamic coefficient model.

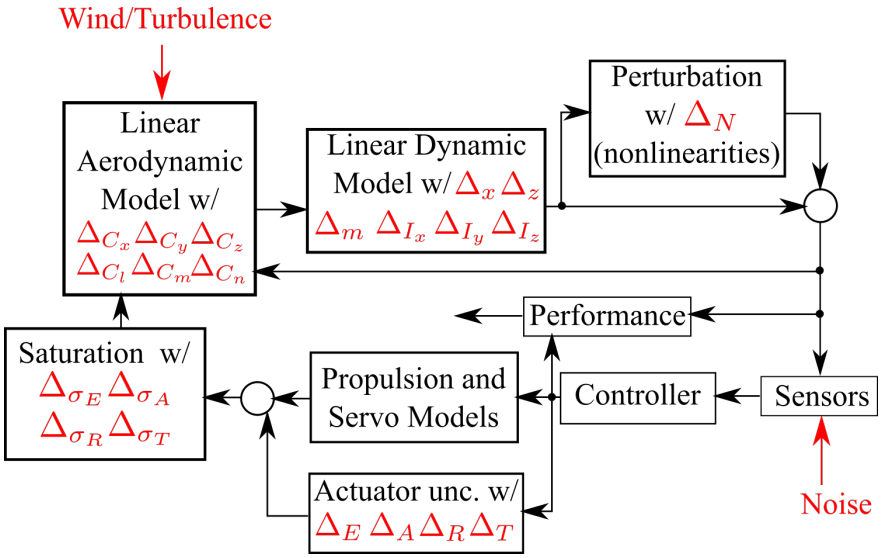

Figure 3.1: The fixed-wing UAS uncertainty framework

Bounds and rate-bounds on each Δ_{C_i} are obtained by conducting flight tests and comparing the disparity between the observed aerodynamic coefficient values and those predicted by the linearized aerodynamic model (see Fig. 3.2).

Because the magnitude error distribution had large outliers, the resulting bounds led to unrealistic worst-case aerodynamics. To remove such outliers, a modified version of ellipsoidal peeling [61] is used. In this approach, the calculated error of each aerodynamic coefficient at a particular time constitutes a single point in $\mathbb{R}^6$. Then, the smallest volume ellipsoid which encapsulates the set of error data points is constructed, and the furthest point from the ellipsoid center is removed from the data set. The process continues until there ceases to be a dramatic decrease of the ellipsoid's volume. Though this is a heuristic approach, it is particularly fitting in this context because the detection of outliers is insensitive to the scaling and bias of each coordinate in the data set. Removing 10% of the error data set by ellipsoidal peeling produces an ellipsoid whose volume is 35% of the original ellipsoid's volume. Noting that the decrease in ellipsoidal volume is much less after peeling 10% of the error data set (Fig. 3.3) suggests that the peeled points were set outliers.

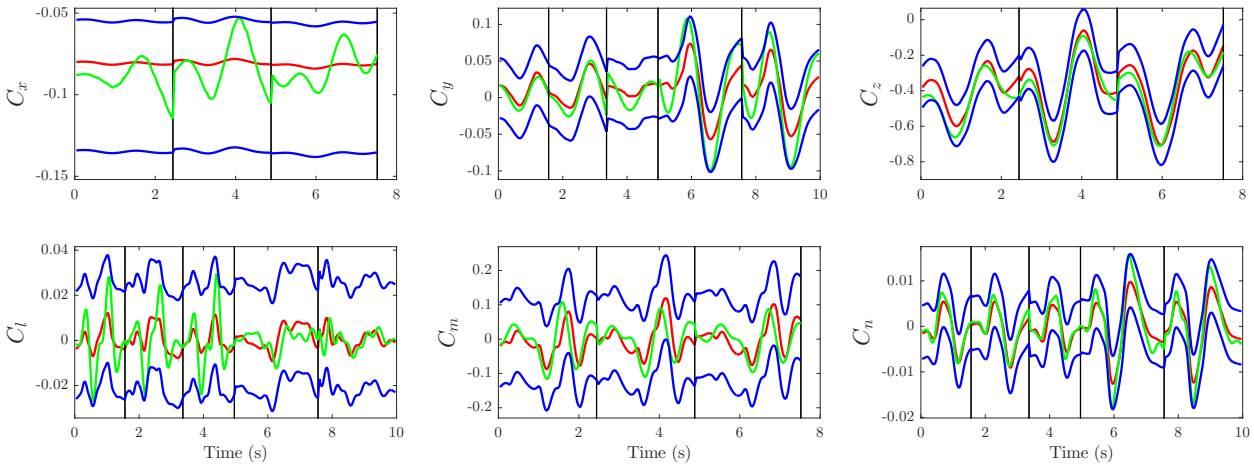

Figure 3.2: Coefficient histories obtained from the linearized aerodynamic model (red) are compared with those from accelerometer data (green) in a validation flight test to obtain uncertainty magnitude bounds (blue).

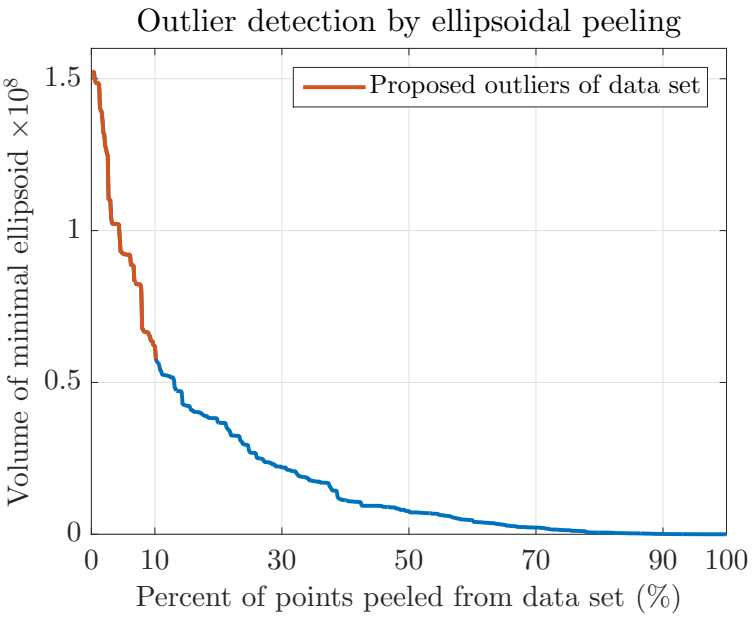

Figure 3.3: Volume of ellipsoids during ellipsoidal peeling routine.

Table 3.1: Aero model values and uncertainty bounds, where $\Delta_{C_i}(k) \in [\Delta_{C_i}^-,\ \Delta_{C_i}^+]$ and $(\Delta_{C_i}(k+1) - \Delta_{C_i}(k)) \in [\nu_{C_i}^-,\ \nu_{C_i}^+]$

Term	Value	Term	Value	Term	Value
$\Delta_{C_x}^+$	0.0259	$\Delta_{C_z}^+$	0.1191	$\Delta_{C_m}^+$	0.1250
$\Delta_{C_x}^-$	-0.0542	$\Delta_{C_z}^-$	-0.1129	$\Delta_{C_m}^-$	-0.1203
$\nu_{C_x}^+$	0.0061	$\nu_{C_z}^+$	0.0239	$\nu_{C_m}^+$	0.0352
$\nu_{C_x}^-$	-0.0142	$\nu_{C_z}^-$	-0.0417	$\nu_{C_m}^-$	-0.0457
$\Delta_{C_y}^+$	0.0370	$\Delta_{C_l}^+$	0.0256	$\Delta_{C_n}^+$	0.0061
$\Delta_{C_y}^-$	-0.0448	$\Delta_{C_l}^-$	-0.0221	$\Delta_{C_n}^-$	-0.0056
$\nu_{C_y}^+$	0.0101	$\nu_{C_l}^+$	0.0092	$\nu_{C_n}^+$	0.0031
$\nu_{C_y}^-$	-0.0117	$\nu_{C_l}^-$	-0.0117	$\nu_{C_n}^-$	-0.0015

It is important to note that this method of quantifying aerodynamic uncertainties carries an implicit assumption; the analysis applies only to flights which remain in the envelope that was tested during the quantification of uncertainties. If the UAS flies beyond this envelope, the resulting IQC analysis is no longer valid. The envelope tested in this chapter consists of straight and level flight, circular turns, and dynamic responses to mode excitations from the UAS actuators [56].

3.2.2 Actuator uncertainties

Actuator model uncertainties are characterized by four DLTI perturbations: Δ_E, Δ_A, Δ_R, and Δ_T. These perturbations are added to the nominal actuator models (i.e., $\hat{G}_{\text{act},i}(z) = \hat{G}_{\text{act},i}^{\text{nom}}(z) + \hat{\Delta}_i(z)$). For the servomotors, $\hat{G}_{\text{act},i}^{\text{nom}}(z)$ is the discretization of the second-order model (2.6), whose parameters ω_{ns} and ζ_s are obtained by measuring the servomotor frequency response. The discrepancy between the modeled and observed frequency response then determines the bound on $\|\hat{\Delta}_i\|_\infty$. Similar to the aerodynamic model case, this approach encapsulates the errors in both the parameter estimation and the assumed structure of the actuator model. Discrepancies between the modeled and observed frequency response of the

servomotors are shown in [13]. Because the nominal throttle model is static and utilizes lookup tables, the bound associated with $\|\Delta_T\|_\infty$ is 0.2, greater than the bound for the servomotor uncertainties $\|\Delta_E\|_\infty$, $\|\Delta_A\|_\infty$, and $\|\Delta_R\|_\infty$, which is 0.05.

Actuator saturation is encapsulated with four RB-SLTV uncertainties: Δ_{σ_E}, Δ_{σ_A}, Δ_{σ_R}, and Δ_{σ_T}. Saturation is approximated by $\text{sat}(u_i) \approx u_i + u_i\Delta_{\sigma_i}$. The bounds on Δ_{σ_i} determine the saturation tolerance against which the system will be analyzed. In this work, with $\Delta_{\sigma_i} \in [0, 0.1]$, IQC analysis considers a saturation tolerance of 10%. There are well-suited IQC multipliers for odd-monotonic and slope-restricted nonlinearities that would encapsulate saturation entirely. But these multipliers require the open-loop plant to be stable [22], which is typically not the case for 6-DOF aircraft dynamic models, including the one used here.

3.2.3 Uncertainties in UAS dynamics

The UAS dynamic system equations are obtained from linearizing and discretizing (2.5), (2.3), and (2.4), where the system outputs and inputs are $\bar{x}$ and $[\bar{M}^T, \bar{F}^T]^T$, respectively. There are six SLTI uncertainties in the dynamic model corresponding to uncertain CG location (Δ_x, Δ_z), mass (Δ_m), and moments of inertia $(\Delta_{I_x}, \Delta_{I_y}, \Delta_{I_z})$. Per the symmetry assumption of the Telemaster airframe, the lateral CG offset Δ_y is assumed negligible and hence is omitted. Similarly, the I_{xz} and $\Delta_{I_{xz}}$ terms are omitted. All three terms, however, could be incorporated if deemed necessary.

The parametric terms Δ_m, Δ_{I_x}, Δ_{I_y}, and Δ_{I_z} are included by replacing m and J with $m+\Delta_m$ and $J+\text{diag}(\Delta_{I_x}, \Delta_{I_y}, \Delta_{I_z})$. The uncertainty in the UAS CG is already incorporated into (2.5). The resulting linear dynamic LFT is denoted by $(G_{\text{dyn}}, \Delta_{\text{dyn}})$. The parametric uncertainty bounds are given in Table 3.2 and reflect the greatest variations we have observed in the test platform when flying different missions and payloads.

Table 3.2: Parametric uncertainties, where $\Delta_{(\cdot)} \in [\Delta^-_{(\cdot)},\ \Delta^+_{(\cdot)}]$

	Δ_m	Δ_x	Δ_z	Δ_{I_x}	Δ_{I_y}	Δ_{I_z}
$\Delta^-_{(\cdot)}$	$-0.1\,m$	$0\,m$	$-0.03\,m$	$-0.15\,I_x$	$-0.15\,I_y$	$-0.15\,I_z$
$\Delta^+_{(\cdot)}$	$0.1\,m$	$0.03\,m$	$0.03\,m$	$0.15\,I_x$	$0.15\,I_y$	$0.15\,I_z$

Algorithmic methods for formulating LFTs do not always produce LFTs with the smallest dimensions. Constructing the linear dynamic LFT with the aforementioned uncertainties results in a block Δ_{dyn} of size (2498×2498), creating an LFT far too large for IQC analysis. Work done by [62] describes how to obtain a minimal realization of an LFT by eliminating the uncontrollable and unobservable states. By applying these results, the uncertainty block reduces from $\Delta_{\text{dyn}} = \text{diag}(\Delta_m I_{539}, \Delta_x I_{702}, \Delta_z I_{706}, \Delta_{I_x} I_{222}, \Delta_{I_y} I_{107}, \Delta_{I_z} I_{222})$ to $\Delta^{\min}_{\text{dyn}} = \text{diag}(\Delta_m I_{76}, \Delta_x I_{71}, \Delta_z I_{61}, \Delta_{I_x} I_{21}, \Delta_{I_y} I_{24}, \Delta_{I_z} I_{34})$, a (287×287) block. We note that this realization is *equivalent* to the original, there is no error induced by the order reduction.

Though significantly reduced, the size of the minimal LFT $(G^{\min}_{\text{dyn}}, \Delta^{\min}_{\text{dyn}})$ is still too large for IQC analysis. Therefore it is necessary to use model reduction techniques on $(G^{\min}_{\text{dyn}}, \Delta^{\min}_{\text{dyn}})$ to obtain a reduced system $(G^r_{\text{dyn}}, \Delta^r_{\text{dyn}})$, which will introduce some degree of model reduction error. If the linear dynamic LFT were strongly stable [28], then balanced truncation would be an appropriate method for further reducing $(G^{\min}_{\text{dyn}}, \Delta^{\min}_{\text{dyn}})$ to a close approximation while preserving the structure of the uncertainty. Because of the instability of the nonlinear dynamics in the 6-DOF UAS equations of motion (and thereby the linear dynamic LFT), the balanced truncation method is not applicable in this case. However, the LFT under consideration is strongly stabilizable and detectable, and hence the coprime factors reduction method [28, 63, 64], which extends the range of applicability of balanced truncation, can be used. To incorporate the reduction error, we would ideally use an upper bound on $\|(G^r_{\text{dyn}}, \Delta^r_{\text{dyn}}) - (G^{\min}_{\text{dyn}}, \Delta^{\min}_{\text{dyn}})\|_{\ell_2 \to \ell_2}$ supplied by the reduction technique and introduce a dynamic LTI uncertainty Δ_E into the reduced linear dynamic LFT. However, the error LFT

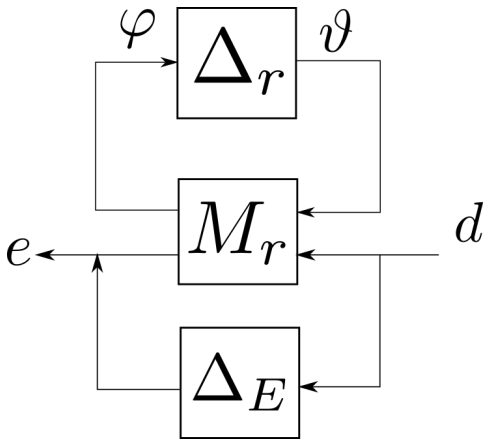

Figure 3.4: Model reduction error is incorporated into the reduced system as the DLTI uncertainty Δ_E.

system in this case is not stable and so the aforementioned norm does not exist. The coprime factors reduction method does provide an upper error bound related to the *coprime factorization* of the linear dynamic LFT; this bound, however, is not useful for our purposes.

Rather than finding the discrepancy between $(G^r_{\text{dyn}}, \Delta^r_{\text{dyn}})$ and $(G^{\min}_{\text{dyn}}, \Delta^{\min}_{\text{dyn}})$, another approach relies on estimating the error between the systems $(M_r, \Delta^r_{\text{dyn}})$ and $(M, \Delta^{\min}_{\text{dyn}})$, where $(M_r, \Delta^r_{\text{dyn}})$ designates the closed-loop LFT system formed by $(G^r_{\text{dyn}}, \Delta^r_{\text{dyn}})$, the linearized aerodynamic and actuator models, and a specific controller; $(M, \Delta^{\min}_{\text{dyn}})$ is similarly defined. This error is captured by a dynamic LTI operator Δ_E which is added to the reduced system. An appropriate bound on $\|\Delta_E\|_{\ell_2 \to \ell_2}$ is obtained by first gridding the space of uncertain parameters and respectively "closing" $(M_r, \Delta^r_{\text{dyn}})$ and $(M, \Delta^{\min}_{\text{dyn}})$ into certain LTI systems $H^{(i)}_r$ and $H^{(i)}$, at each grid point, and then finding the largest $\mathcal{D}$-to-ℓ_2-gain performance level of the error systems $(H^{(i)} - H^{(i)}_r)$. IQC analysis is conducted on the LFT $(M_r, \Delta_r) + \Delta_E$ (see Fig. 3.4), where Δ_r is the same as Δ with the Δ_{dyn} block replaced by Δ^r_{dyn}.

By applying this approach, the uncertainty block reduces from

$$\Delta^{\min}_{\text{dyn}} = \text{diag}(\Delta_m I_{76}, \Delta_x I_{71}, \Delta_z I_{61}, \Delta_{I_x} I_{21}, \Delta_{I_y} I_{24}, \Delta_{I_z} I_{34}) \text{ to}$$

$$\Delta^r_{\text{dyn}} = \text{diag}(\Delta_m I_6, \Delta_x I_4, \Delta_z I_3, \Delta_{I_x} I_1, \Delta_{I_y} I_3, \Delta_{I_z} I_1)$$

which forms an (18×18) block. The error systems closed under Controllers 1, 2, and 3 (which will be later introduced), respectively, yield a maximum $\mathcal{D}$-to-ℓ_2-gain of 0.49, 0.23, and 0.15, respectively. These errors are, respectively, 3%, 2.6%, and 4.6% of the robust $\mathcal{D}$-to-ℓ_2-gain performance level obtained from IQC analysis. Though this is a notable contribution of error, it comes with the benefit of significantly improving the tractability of IQC analysis. Furthermore, by observing the input-output behavior between $H^{(i)}$ and $H_r^{(i)}$, it can be surmised that the reduced LFT accurately reflects the behavior of the original model. Fig. 3.5 shows the worst simulation of the original and the reduced UAS closed under Controller 1 with the worst-case sampling of uncertainties, and demonstrates the close match between the original and reduced closed-loop systems.

The effect of the UAS nonlinear dynamics is expressed with a DLTI uncertainty Δ_N. The matrix $W_N = \text{diag}(1, 1, 1, 3, 1, 1, 0.55, 0.35, 0.2, 5, 10, 10)$ and its inverse pre- and post-multiply Δ_N, respectively, to ensure that the uncertainty is applied on normalized states. The bound $\|\Delta_N\|_\infty \leq 0.01$ was previously chosen in [12] by comparing discrepancies between linear and nonlinear simulations of the UAS.

3.3 An IQC-based tuning routine

A typical approach in controller design relies on obtaining a controller, running Monte Carlo simulations, and studying simulation output to identify which design parameters should be tuned to produce a better controller. These steps are followed by implementing the controller on the physical system to make sure that any discrepancies between the simulation environment and the physical one do not inflict significant performance degradation; otherwise, the design parameters have to be re-tuned. This procedure exists because controller robustness

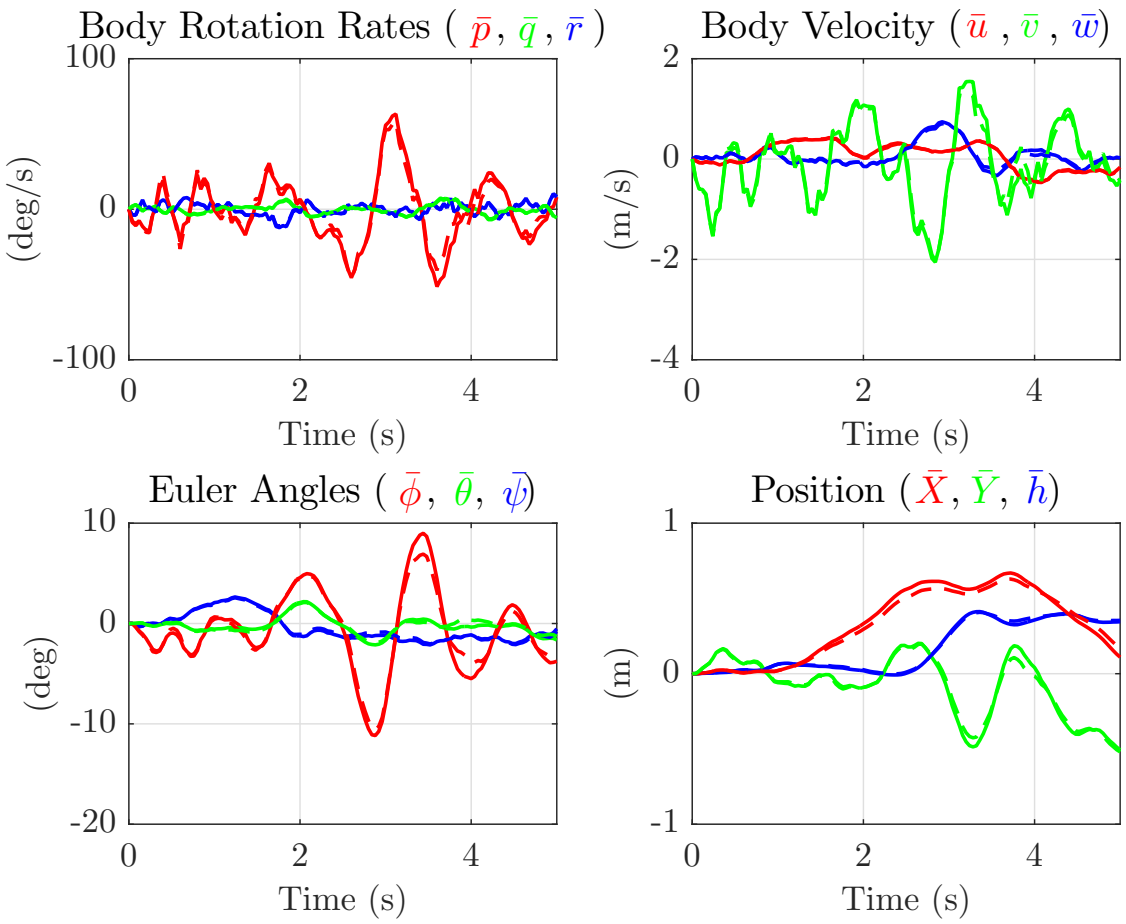

Figure 3.5: State histories for controlled UAS; dashed lines pertain to the reduced LFT, solid lines pertain to the original LFT.

and performance are competing objectives, and so the engineer has to judiciously choose the performance output that gives the appropriate trade-off between these objectives. IQC analysis is capable of condensing what a control engineer might observe from thousands of simulations into a single scalar quantity: the robust $\mathcal{D}$-to-ℓ_2-gain performance level γ.

This chapter proposes using IQC analysis in tuning controller design parameters with a gradient-based steepest descent approach. The following algorithm can guide the control design process for uncertain systems, and is applicable to linear controllers synthesized by a myriad of approaches, not just $\mathcal{H}_\infty$ synthesis techniques. The minimization routine operates on the idea that IQC analysis yields a mapping from uncertain systems to $\mathbb{R}_{++}$. This mapping is annotated by $\mathrm{IQC}(M, \Delta) = \gamma$, where $\mathrm{IQC}(M, \Delta)$ refers to solving the SDP (2.14) for γ with the problem data derived by (M, Δ). Given an open-loop system (G, Δ), and parameters $c \in \mathbb{R}^m$ that specify a controller K (denoted by $\mathrm{DesignCTR}(c)$) which produces a closed-loop system (annotated by $\mathrm{CloseLP}(G, K) = M$), IQC analysis can be loosely considered to provide a nonlinear mapping from $\mathbb{R}^m$ to $\mathbb{R}_{++}$, expressed as $\overline{\mathrm{IQC}}(c, G, \Delta) = \gamma$. Therefore, finding a controller K which yields the closed-loop uncertain system with the smallest possible robust $\mathcal{D}$-to-ℓ_2-gain performance level γ amounts to finding the design parameters which minimize γ. This can be done with numerous nonlinear minimization algorithms, though the gradient-based steepest descent method is employed herein because it is strictly a numerical process which only requires information obtained from evaluating $\overline{\mathrm{IQC}}(c, G, \Delta)$. In this method, for a given $c^{(i)}$, the corresponding robust $\mathcal{D}$-to-ℓ_2-gain performance level is calculated ($\overline{\mathrm{IQC}}(c^{(i)}, G, \Delta) = \gamma$). Then, the gradient of γ at $c^{(i)}$ is estimated by perturbing $c^{(i)}$ in each of its coordinates and calculating the associated robust $\mathcal{D}$-to-ℓ_2-gain performance levels. With the estimated gradient, a new vector $c^{(i+1)}$ is obtained by moving from $c^{(i)}$ in the direction of the steepest descent. This process is repeated until there is little appreciable change in γ. Pseudo-code implementation of the routine can be found

in Algorithm 1. More sophisticated methods for estimating the gradient can be applied, but the method in Algorithm 1 requires the least number of calls to $\overline{\text{IQC}}(c, G, \Delta)$, which may be a time-consuming function. Constraining c in the routine is not explicitly detailed, but can easily be done.

Algorithm 1 Tuning routine via IQC analysis

Inputs: Initial controller parameters $c \in \mathbb{R}^{n_c}$ and open-loop LFT (G, Δ) satisfying the system equations

$$\begin{bmatrix} \varphi \\ e \\ y \end{bmatrix} = \begin{bmatrix} G_{11} & G_{12} & G_{13} \\ G_{21} & G_{22} & G_{23} \\ G_{31} & G_{32} & G_{33} \end{bmatrix} \begin{bmatrix} \vartheta \\ d \\ u \end{bmatrix}, \quad \vartheta = \Delta\varphi$$

Outputs: Final controller parameters c and γ for the closed-loop LFT (M, Δ)

1: Define γ_{tol} and dc (optimization tolerance and step size)
2: $\gamma \leftarrow \overline{\text{IQC}}(c, G, \Delta)$, i.e. $\begin{cases} K \leftarrow \text{DesignCTR}(c) \\ M \leftarrow \text{CloseLP}(G, K) \\ \gamma \leftarrow \text{IQC}(M, \Delta) \end{cases}$
3: **while** 1 **do** # steepest descent algorithm
4: **for** $i = 1 : n_c$ **do** # estimate gradient
5: $c^+ \leftarrow [c_1, \ldots, c_i + dc, \ldots, c_{n_c}]^T$
6: $\gamma_i^+ \leftarrow \overline{\text{IQC}}(c^+, G, \Delta)$
7: $\nabla\gamma \leftarrow [\gamma_1^+ - \gamma, \ldots, \gamma_{n_c}^+ - \gamma]^T$
8: $c \leftarrow c - dc\frac{\nabla\gamma}{\|\nabla\gamma\|}$
9: $\gamma \leftarrow \overline{\text{IQC}}(c, G, \Delta)$
10: **if** $\|\nabla\gamma\|/dc < \gamma_{\text{tol}}$ **then**
11: **exit** while loop

Though the iterative refinement of c is time-consuming, this approach allows the control engineer to use a large variety of synthesis methods to obtain a robust controller. In this chapter, c defines the performance weights used in $\mathcal{H}_\infty$ synthesis, but it may instead define the entries of Q and R matrices for LQR synthesis, or the PID gains for a PID controller. This is especially attractive in controlling the UAS, as oftentimes the systems engineer is required to use specific autopilot computers which have an inflexible controller structure. This method can be applied to tune the controller parameters within a given structure to eventually obtain a robust controller.

Concerning the literature to date, the work in [65], [66], [67], and [68] provides more rigorous approaches to robust synthesis via IQCs. However, each approach synthesizes an *unstructured* controller and does not consider the use of signal IQCs. The work in [69] provides a synthesis method using signal IQCs, but does not allow the incorporation of uncertainties in the system model. The tuning method herein is most akin to the results in [70], which use non-smooth optimization techniques to iteratively find controller parameters that improve the robust performance of a system. Although the work in [70] incorporates signal IQCs and can synthesize structured controllers, the parameter space grows quadratically with the controller size, rapidly increasing the computational complexity of the problem. The approach in this work is capable of tuning large, unstructured controllers without having a prohibitively large parameter space. For example, the 18-state $\mathcal{H}_\infty$ controllers studied in this chapters are tuned with 14 parameters. Additionally, this routine can tune structured controllers, such as the PID controller given in Section 4.2. Perhaps the greatest barrier in this approach is its computational complexity; each iteration requires solving n_c SDPs. However, work in [71, 72] has developed methods for quickly solving IQC analysis problems, which can significantly reduce the computational effort of this routine.

This routine attempts to find a controller which locally minimizes the robust $\mathcal{D}$-to-ℓ_2-gain performance level γ, starting with some initial controller. Also, the mapping $\overline{\text{IQC}}(c, G, \Delta)$ is generally not a function since many synthesis techniques (standard $\mathcal{H}_\infty$, LPV, etc.) produce a non-unique K which satisfies the design parameters. Even for synthesis techniques which provide a one-to-one mapping from c to K (such as PID and LQR), Theorem 2.1 involves an optimization problem which may be infeasible, implying that $\overline{\text{IQC}}(c, G, \Delta)$ is not continuous in c. Nevertheless, this heuristic approach has consistently provided a final controller with robust performance superior to the starting controller. Furthermore, its validation on a UAS demonstrates the effectiveness of IQC analysis in guiding the control design process for

highly uncertain systems.

In the ideal implementation of Algorithm 1, each time the routine synthesizes a new controller it should re-characterize the bound on $\|\Delta_E\|_\infty$. Estimating this bound is computationally expensive (sampling the 6-dimensional parametric uncertainty space and calculating the $\mathcal{D}$-to-ℓ_2-gains), and because of this, we do not incorporate Δ_E in the IQC analysis for our implementation of Algorithm 1. If computation time were not a consideration, Δ_E could easily be added in the routine. In the forthcoming results, after tuned controllers are obtained from Algorithm 1, the bound on Δ_E for each controller is determined and included in the calculations for all γ values. Therein we see that although we do not include the model reduction error while implementing Algorithm 1, the routine still produces controllers which progressively reduce the robust $\mathcal{D}$-to-ℓ_2-gain performance levels, even after reintroducing the perturbation Δ_E and repeating IQC analysis. This suggests that the reduction error has a secondary influence in determining the system's robust $\mathcal{D}$-to-ℓ_2-gain performance level and it is not essential to include it in the tuning routine.

The usefulness of the proposed minimization routine is demonstrated in Section 3.4.1, where the routine starts with a preliminary controller and tunes it to a controller which has a significantly improved robust performance level. The choice of the performance output used in IQC analysis is up to the designer, and typically reflects the outputs that the designer deems critical. For instance, if the position error is most important in a particular application, then the analysis performance output may be chosen as $e = [\bar{X}, \bar{Y}, \bar{h}]^T$. The position error is important in our case; in fact, as will be seen in the following section, our analysis results convey the effects of different uncertainties on the position error. However, achieving a small position error at the expense of large angular rates and displacements is unfavorable, and hence, the performance output used in IQC analysis for tuning controllers is chosen as $e = [\bar{p}_b, \bar{q}_b, \bar{r}_b, \bar{u}_b, \bar{v}_b, \bar{w}_b, \bar{\phi}, \bar{\theta}, \bar{\psi}, \bar{X}, \bar{Y}, \bar{h}]^T$. This choice is simple–$e$ merely contains all of the

UAS's physical states without a complicated weighting scheme. Accounting for the different scales of the UAS's states, we see that the chosen weighting scheme more heavily penalizes position than velocities, angular rates, and angular displacements, which should produce a controller that exhibits desirable position tracking without any erratic behavior in the remaining states. It will be seen that the resulting controllers obtained from the routine not only have improved robust performance in position, but also in the actuation effort (probably since the chosen e accounts for the angular rates). Finally, these claims will be supported with simulation and flight test data, validating the capability of this routine and the utility of IQC analysis.

3.4 Results

In this section, we first demonstrate how Algorithm 1 tunes an initial controller to controllers with improved robust performance. We then present detailed IQC analysis results for the final controller obtained from the algorithm. The analysis results are then compared and validated against flight data from testing each controller in various wind conditions.

The Linear Fractional Representation (LFR) Toolbox for `MATLAB` was used in this work to formulate LFTs from uncertain linear systems [73]. Solving the SDP (2.14) was done through 64-bit MATLAB R2015a, using YALMIP/MOSEK [74, 75] on a computer cluster utilizing 2 Intel Xeon E5-2683 2.10 GHz CPUs (16 cores per CPU) with 128 GB of RAM. Solution times ranged from 2 to 8 minutes, depending on the uncertainty groups analyzed. For comparison, on a Dell desktop using an Intel Xeon W3550 (3.07 GHz) processor with 6 GB of RAM, solution times ranged from 5 to 20 minutes. Producing a numerically well-conditioned SDP depends on the problem parameters used in IQC analysis, namely, the length of the basis functions and the pole locations for $\hat{B}$ in (2.15) and $\hat{\Theta}$ in (2.18). The following results were produced by setting the basis length $b = 2$ in (2.15), since a lower basis length yielded more

conservative results and a larger basis length resulted in a large SDP with poor numerical conditioning. When utilizing the signal IQC for "banded white" signal sets (see (2.18)), we set $\omega_0 = \frac{2\pi}{3}$. To incorporate the impact of signals whose power spectral density is constant over the entire frequency range, ω_0 should be set to π. Also, SeDuMi and SDPT3 were not helpful in obtaining these results, as they were either too slow in solving the resulting SDP or could not make significant progress in reducing the objective value.

As to the locations of the poles in (2.15) and (2.18), there is currently no rigorous treatment for finding the values which yield the best results. However, we intend to demonstrate that the qualitative comparison of robustness between controllers is preserved under different problem parameters. We will show this by initiating the routine in Section 3.3 with certain pole locations for (2.15) and (2.18). Then, with controllers obtained from the routine, detailed IQC analysis is done with different pole locations to obtain less conservative results. It will be seen that if there is a notable decrease in the γ-values between systems using different controllers, a corresponding decrease in the γ-values will typically be observed, even when the analysis is done with different problem parameters. Hence, it is often advantageous to execute the routine in Section 3.3 with problem parameters that result in smaller SDPs (to save computational effort), and later do detailed analysis on the final controller using problem parameters that may yield larger SDPs (to obtain less conservative results).

3.4.1 Tuning controllers with IQC analysis

The minimization routine proposed in Section 3.3 is applied to an initial "Controller 1." The first iteration in the routine yields "Controller 2." After 31 iterations, the routine produces the final controller, "Controller 3." The time to finish an iteration is about 16 to 20 minutes, and the routine takes about 10 hours to reach Controller 3. As mentioned in Section 3.3, the performance output used in IQC analysis during the execution of the routine

Table 3.3: Bounds on average $\mathcal{D}$-to-ℓ_2-gain from Algorithm 1 and penalty weights c_i for Controllers 1, 2 and 3

Cont.	$\gamma_{\text{IQC}}^{\text{Ave}}$ $(\epsilon = 1)$	c_p	c_q	c_r	c_{V_a}	c_ϕ	c_θ	c_ψ	c_X	c_Y	c_z	c_{δ_E}	c_{δ_A}	c_{δ_R}	c_{δ_T}
1	15.5	0.1	0.1	0.1	0	0	0	0	0	0	0.1	0	0	0	0.2
2	8.1	0.1	0.1	0.1	0	0	0	0	0	0.02	0.1	0	0	0	0.2
3	3.4	0.04	0.11	0.05	0.05	0.005	0.01	0.003	0.04	0.02	0.03	0.005	0.003	0	0.2

is $e = [\bar{p}_b, \bar{q}_b, \bar{r}_b, \bar{u}_b, \bar{v}_b, \bar{w}_b, \bar{\phi}, \bar{\theta}, \bar{\psi}, \bar{X}, \bar{Y}, \bar{h}]^T$. We select $\lambda = 0.9$ and $a_1 = -0.5$ for the pole locations in (2.15) and (2.18), and $dc = 0.02$ in the routine. To further simplify the SDP problem, we characterize the 10-channel noise disturbance signal with a single multiplier $\Phi(z) \in \mathcal{RL}_\infty^{10\times 10}$. By so doing, the analysis results correspond to the robust worst-case *average* performance (denoted $\gamma_{\text{IQC}}^{\text{Ave}}$ in Table 3.3), as mentioned in Section 2.3.

The structure of the performance output used to synthesize each of the aforementioned controllers is given by (2.9), with the values of the penalty weights c_i provided in Table 3.3, along with an upper bound on the corresponding average $\mathcal{D}$-to-ℓ_2-gain obtained from the minimization routine. The bounds for Controllers 1, 2, and 3 are 15.5, 8.1 and 3.4, respectively, demonstrating a significant improvement in robust performance. Controller 2 is obtained after one iteration and is selected to demonstrate an important aspect of the algorithm. By inspecting Table 3.3, it can be seen that there is no penalty on the cross track error $\bar{Y}$ in the synthesis performance weights for Controller 1. Intuitively, penalizing $\bar{Y}$ is essential to obtain satisfactory performance in tracking a circular trajectory, and the routine discovers this fact through its gradient calculations. Indeed, for Controller 2, the routine adjusts the synthesis performance output by increasing the penalty on $\bar{Y}$ with the maximum allowable amount for an iteration (dc). As shown in the reconstructed flight tests (Fig. 3.8 and `http://www.dept.aoe.vt.edu/~farhood/iqcFlights.html`), Controller 2 achieves a clear improvement in circular tracking. This manifests the capability of the minimization routine in determining the most advantageous adjustment of the synthesis performance weights to obtain improved robust performance.

3.4.2 Detailed analysis of controller 3

We now make a detailed inspection of IQC analysis results for the UAS using Controller 3 from the previous subsection. It is important to note that in the previous subsection we use a single multiplier $\Phi(z) \in \mathcal{RL}_\infty^{10\times 10}$ for the 10-channel noise disturbance, which signifies that the resulting γ-values pertain to the averaged notion of the $\mathcal{D}$-to-ℓ_2-gain. As a more useful metric, henceforth we use ten multipliers $\Phi(z) \in \mathcal{RL}_\infty^{1\times 1}$, where each $\Phi(z)$ characterizes a single noise disturbance channel. In this case, the upper bounds provided by IQC analysis are the robust $\mathcal{D}$-to-ℓ_2-gain performance levels. To make the results more relatable, the performance output used in IQC analysis from now on is $e = [\bar{X}, \bar{Y}, \bar{h}]^T$. The results in this subsection are obtained by choosing the pole locations in (2.15) and (2.18) as follows: λ is set to either 0.3 or 0.9, and $[a_1, a_2, a_3, a_4]$ is set to either $[-0.9, -0.2, 0.5, 0.9]$ or $[-0.7, -0.1, 0.6, 0.8]$. These choices produce SDPs with better numerical conditioning for MOSEK. We also use a longer basis function for (2.18) than the basis function used in the minimization routine. This comes at a cost of greater computational burden in order to provide less conservative γ-values. After formulating the LFT (M, Δ), Theorem 2.1 is applied to $(M, \epsilon\Delta)$, where $\epsilon \in [0\ 1]$ is a scaling factor, and Δ is composed of uncertainties from the three groups discussed in Section 3.2. When $\epsilon = 1$, the bounds on Δ are the same as recorded in Section 3.2. The analysis results are shown in Fig. 3.6.

When considering all uncertainties, the upper bound γ on the robust $\mathcal{D}$-to-ℓ_2-gain is 3.15, a 75% degradation from 1.8, the $\mathcal{D}$-to-ℓ_2-induced norm of the nominal system. Considering individual sets, the aero group results in the greatest degradation of γ at 34%. The dynamic and control groups cause, respectively, a 23.5% and 16% degradation in γ.

Qualitatively, it is observed that the dependence of γ on ϵ is generally nonlinear with varying degrees. For example, Fig. 3.6 shows that, for the dynamic group, γ increases almost linearly with ϵ, while this increase becomes notably nonlinear in the case of the control group. Indeed,

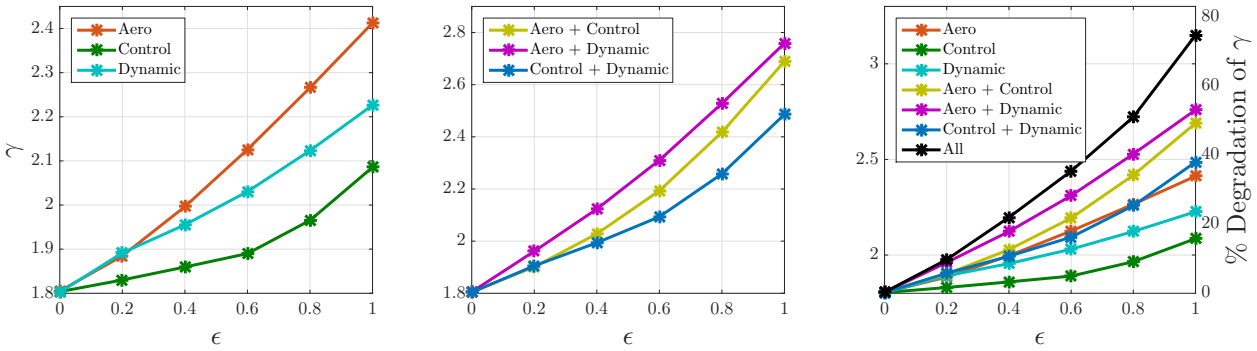

Figure 3.6: IQC upper bounds on $\|(M, \Delta)\|_{\mathcal{D}\to\ell_2}$ for Controller 3 subject to all uncertainty groups.

by increasing ϵ beyond 1, the degradation of γ by the control group would eventually be greater than that produced from the dynamic group. This nonlinear effect on γ also occurs when uncertainties are coupled. For example, the degradation under all uncertainties (75%) is *more* than the sum of degradations from the aero + dynamic group (53%) and the control group (16%). However, this nonlinear effect is not always noticed; the coupling of the aero group and the control group produces a degradation which is the sum of degradations of both groups. Such qualitative observations provide insight towards the most detrimental uncertainties and which combinations have the most impact. Similarly, this information can guide the systems engineer in considering what components of the UAS should be more precisely characterized or tightly restricted.

3.4.3 Validation of IQC analysis results

This subsection provides detailed IQC analysis for Controllers 1, 2, and 3. The noise multipliers, performance output, and problem parameters are the same as those detailed in Section 3.4.2. By consulting the left-most subplot of Fig. 3.7 and Table 3.4, we see that Controllers 1, 2, and 3 have respective robust $\mathcal{D}$-to-ℓ_2-gain performance levels of 2.8, 2.7, and 1.8 for $\epsilon = 0$, and 16.3, 8.7, and 3.15 for $\epsilon = 1$. Here we observe another important aspect of the

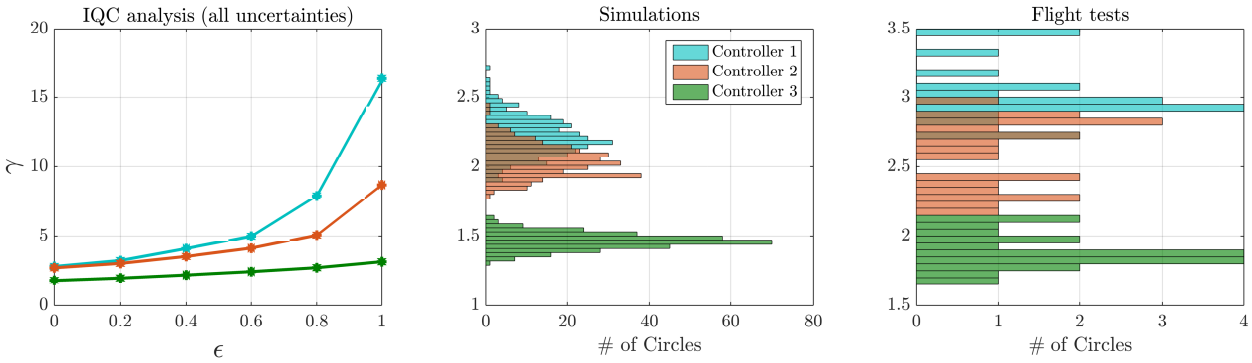

Figure 3.7: $\mathcal{D}$-to-ℓ_2-gains for Controller 1, Controller 2, and Controller 3 using $e = [\bar{X}, \bar{Y}, \bar{h}]^T$ are obtained from IQC analysis, simulations, and flight tests. The $\mathcal{D}$-to-ℓ_2-gain is computed for each completed circle in simulated flight and flight tests.

Table 3.4: Performance bounds from IQC analysis, simulation and flight data for Controllers 1, 2 and 3

#	$\gamma_{\text{IQC}}\,(\epsilon = 0)$	$\gamma_{\text{IQC}}\,(\epsilon = 1)$	$\gamma_{\max}$ (Simulation)	$\gamma_{\max}$ (Flight)
1	2.8	16.3	2.7	3.5
2	2.7	8.7	2.4	3
3	1.8	3.15	1.6	2.2

minimization routine. Even though the routine was executed with different problem parameters and an averaged notion of robust performance (both differences employed to reduce computational complexity), the relative differences between the γ-values obtained from the minimization routine and from the detailed IQC analyses remain the same.

The importance of using signal IQCs to characterize noise disturbances is especially notable in these analyses. Without using signal IQCs, the robust ℓ_2-gain performance levels with Controllers 3 and 2 are, respectively, 5.5 and 15.7, a dramatic increase of conservatism. For Controller 1, the associated SDP was infeasible. Hence, to obtain bounds which more accurately reflect reality, it is important to use signal IQCs.

To support IQC analysis results, nonlinear simulations in `MATLAB` are executed using (2.5), (2.3), (2.4) with randomly generated uncertainties perturbing the state evolution. SLTI uncertainties such as Δ_m, Δ_x, Δ_{I_x}, Δ_{I_y}, and Δ_{I_z} are pseudo-randomly generated with a

uniform distribution and bounds given in Table 3.2. The nominal aerodynamic model is expressed in Section 2.2, and uncertainties are included in each aerodynamic coefficient C_i by adding pseudo-random sequences $\Delta_{C_i}(k)$ generated with a uniform distribution whose bounds and rate-bounds are given in Table 2.2. Each actuator (including the thrust model) has dynamics described by (2.6), and transfer functions with $\mathcal{H}_\infty$ bounds no greater than 0.05 are pseudo-randomly generated (using `rss`) and included in the servo dynamics to incorporate the effect of $\hat{\Delta}_E(z)$, $\hat{\Delta}_A(z)$, and $\hat{\Delta}_R(z)$. Since the simulation environment models thrust with a second-order system and the analysis framework assumes the thrust model to be static, an additional dynamic perturbation is not incorporated to the thrust model. Finally, the simulation environment exactly characterizes the effect of nonlinear dynamics, saturation, and time-delays, removing the necessity to approximate such effects with the perturbations $\Delta_\sigma(k)$, $\hat{\Delta}_N(z)$, and $\hat{\Delta}_E(z)$.

In each simulated flight, the aircraft completes 1 circle under 3-m/s steady winds, and light turbulence generated by the low altitude Dryden model [76]. The aircraft is also exposed to sensor noise pseudo-randomly generated from zero-mean Gaussian distributions with standard deviations for each channel given by (2.8). All psuedo-randomly generated variables (uncertainties, noise, and wind) are different for each simulated flight of a controller, but replicated across the different controllers, allowing appropriate comparisons of controller performance. The resulting $\mathcal{D}$-to-ℓ_2-gain for each simulation can be computed using the given noise, wind (including steady and turbulent forms), and position errors.

For final validation, these controllers are tested in physical flight. Sensor noise is estimated by subtracting filtered sensor data from raw sensor data. Wind speed is the most difficult to estimate, as ground sensors repeatedly underestimate the wind conditions apparent to the UAS. To achieve a closer estimate of the wind speed, the vehicle ground speed at each time instant is estimated using GPS data and subtracted by the measured airspeed to obtain a

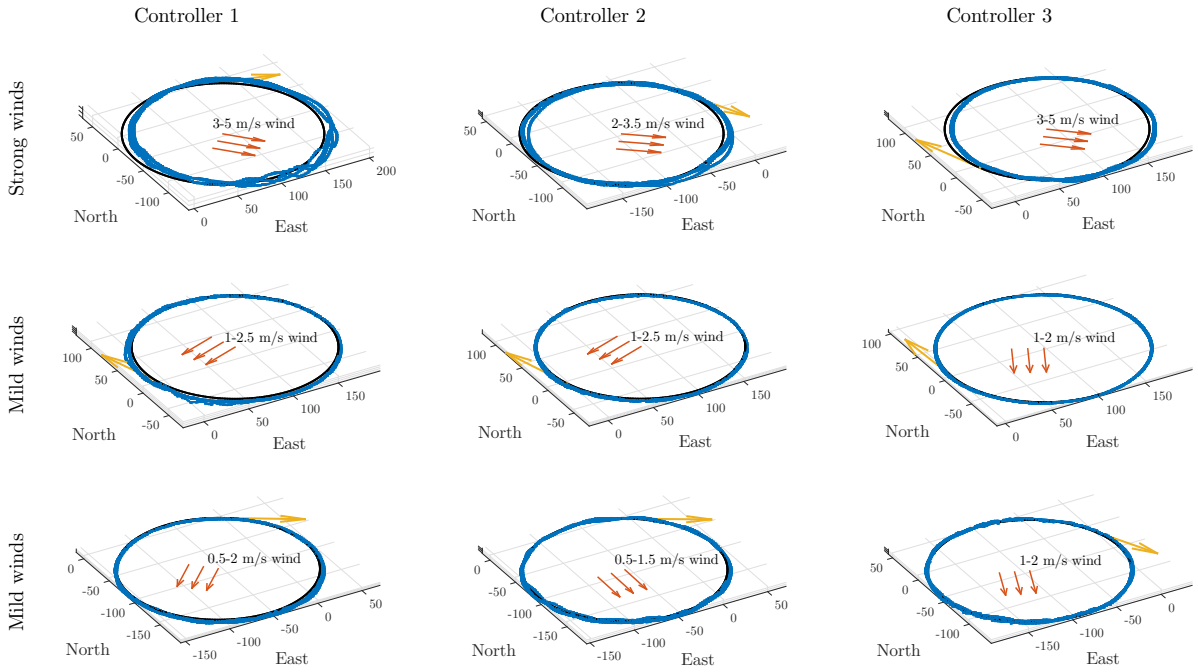

Figure 3.8: Reconstructed flight trajectories of the UAS executing right-turn circles for flight tests. Red arrows indicate wind direction, and yellow arrows indicate direction of flight and initial point of reconstructed trajectory.

lower bound on the wind speed, and ultimately a lower bound on the ℓ_2-norm of the wind velocity. It should therefore be noted that the resulting $\mathcal{D}$-to-ℓ_2-gain from flight data may be an overestimate of the true value. Because of the difficulty in consistently bringing the aircraft to a state close to the trim values , the first 20 seconds of controlled flight segments are not analyzed in these results. Flight segments typically lasted 5-7 minutes, in which 8-10 consecutive circles were executed by the controller. A typical portion of data from flight testing Controller 1 and Controller 3 in strong winds is given in Fig. 3.9.

For both simulations and flight tests, a circular segment consists of 1047 timesteps, or about 42 seconds. Because the $\mathcal{D}$-to-ℓ_2-gains from simulations and flight tests correspond to finite horizon signals, they may be underestimates of the $\mathcal{D}$-to-ℓ_2-gains for infinite horizon signals provided by Theorem 2.1. However, for the simulated and tested systems, the finite horizon length used to calculate the $\mathcal{D}$-to-ℓ_2-gains has not had a notable effect on their mag-

nitudes, suggesting that $\mathcal{D}$-to-ℓ_2-gains calculated with finite horizon signals are a reasonable comparison to analysis results for $\mathcal{D}$-to-ℓ_2-gains corresponding to infinite horizon signals.

The largest calculated $\mathcal{D}$-to-ℓ_2-gains for Controllers 1, 2, and 3 in simulation are, respectively, 2.7, 2.4, and 1.6. The largest calculated $\mathcal{D}$-to-ℓ_2-gains from flight tests are, respectively, 3.5, 3, and 2.2. The two right-most subplots in Fig. 3.7 display a distribution of the calculated $\mathcal{D}$-to-ℓ_2-gains for each completed circle from all flight test and simulation data, regardless of wind condition. In Fig. 3.7 it is quickly apparent that the IQC analysis results are qualitatively consistent with the simulation and flight data. The fact that IQC analysis provides nominal $\mathcal{D}$-to-ℓ_2-gain performance levels ($\epsilon = 0$) which are less than those calculated from flight test data suggests that the uncertainty characterization is necessary to safely describe the physical system. Also, the robust $\mathcal{D}$-to-ℓ_2-gain performance levels from IQC analysis are always greater than the $\mathcal{D}$-to-ℓ_2-gains obtained from simulation and flight data, suggesting that the true uncertainty is captured by the framework in Section 3.2.

The overestimation of IQC performance levels for ϵ=1 as compared to the induced gains from flight tests may suggest that the uncertainty characterization is overly conservative. However, it should be noted that IQC analysis provides *worst-case* robust performance bounds; there may still exist configurations of the true uncertainties and disturbances untested in simulations and physical flights which would yield poorer performance. When consulting Figures 3.8, 3.9, and the reconstructed flight videos (`http://www.dept.aoe.vt.edu/~farhood/iqcFlights.html`), it is readily apparent that Controller 1 and Controller 2 produce erratic and unsafe behavior, especially in strong winds. It is possible that this volatile behavior is reflected in IQC analysis by producing greater robust performance bounds. It is also interesting to note that the simulations indicate far better performance than what is experienced in flight. This highlights the fact that uncertain and nonlinear simulation environments do not fully capture the physical system, and IQC analysis is a helpful tool in bridging the

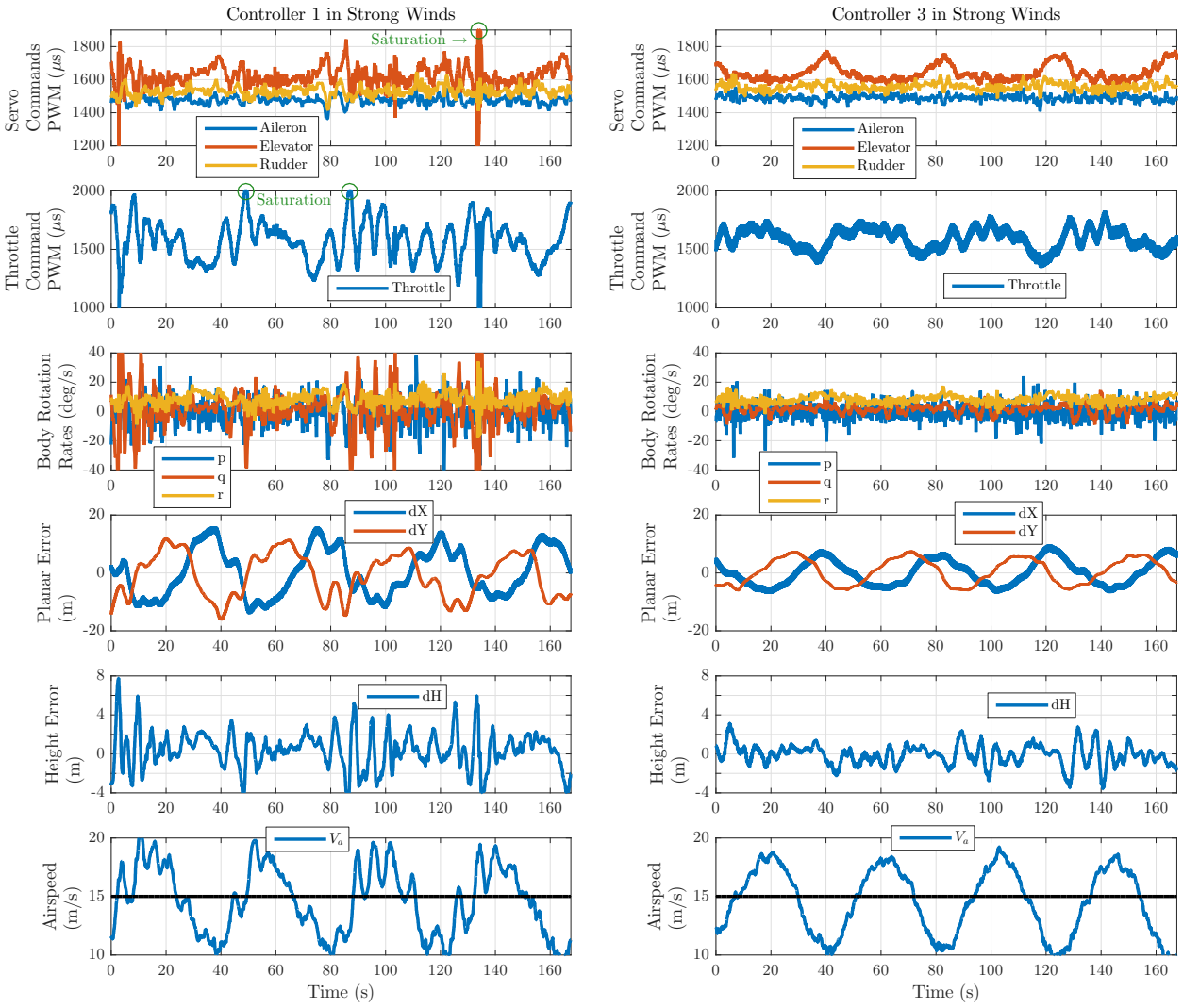

Figure 3.9: Comparison of UAS states under Controllers 1 and 3.

gap. Finally, it is encouraging that in each step from Controller 1 to 3 there is a marked improvement in actuation effort and the response of all UAS states, supporting the utility of IQC analysis in guiding controller design.

Flight tests also demonstrate another advantage of IQC analysis. As seen from Fig. 3.7, when all uncertainties are incorporated, IQC analysis yields a significant decrease in the robust $\mathcal{D}$-to-ℓ_2-gain performance level between Controller 1 and Controller 2 (from $\gamma = 16.3$ to $\gamma = 8.7$). However, when analyzing the nominal system, there is only a slight decrease in the

$\mathcal{D}$-to-ℓ_2-gain performance level (from $\gamma = 2.8$ to $\gamma = 2.7$). Flight tests reflect this significant decrease in $\mathcal{D}$-to-ℓ_2-gains, suggesting the importance of assessing robust performance rather than nominal performance (e.g., $\mathcal{H}_\infty$ analysis) in order to understand the physical system behavior.

Chapter 4

Further development of the uncertain UAS framework

This chapter details a number of improvements on and further validates the uncertain UAS framework discussed in Chapter 3. In Section 4.1 a path-following and trajectory-tracking formulation is derived, wherein the radius of curvature for the desired UAS path can be expressed as an uncertainty amenable to IQC analysis. While the IQC analysis results of Chapter 3 pertained only to flight about a level, circular trajectory, the forthcoming results apply to flight about any level path whose inverse radius of curvature is bounded. Section 4.2 details the three types of controllers synthesized in this chapter: $\mathcal{H}_\infty$, $\mathcal{H}_2$, and PID. These different controller types, alongside the path-following/trajectory-tracking schemes, are employed to demonstrate the utility and validity of the uncertain UAS framework for a variety of controller architectures. Section 4.3 provides a brief summary of the changes in the uncertain UAS framework and Section 4.4 discusses some improvements made to the IQC-based tuning routine. In Section 4.5 we demonstrate the efficacy of the uncertain UAS framework by tuning five different controllers (trajectory-tracking $\mathcal{H}_\infty/\mathcal{H}_2$ and path-following $\mathcal{H}_\infty/\mathcal{H}_2$/PID) and comparing the performance predicted by IQC analysis and simulation with that experienced in flight tests. The results in this chapter originate from [14].

4.1 Path following and trajectory tracking

Whereas the derivations of the nominal UAS in Section 2.2 consider the evolution of the UAS body frame $\mathcal{F}_b$ with respect to an inertial frame $\mathcal{F}_I$, the following equations of motion define the attitude and position of $\mathcal{F}_b$ with respect to the desired *virtual vehicle* frame $\mathcal{F}_v$. To this end, consider a path $\mathcal{P} : \mathbb{R}_+ \to \mathbb{R}^3$, where $\mathcal{P}(\ell)$ represents the position of a virtual vehicle found at a length ℓ along the path $\mathcal{P}$. To denote the dependence of the virtual vehicle position on time, we use P^I_{vI}; in other words, $P^I_{vI}(t) = \mathcal{P}(\ell(t))$. Following the definition of the parallel transport frame [77, 78], the orientation of $\mathcal{F}_v$ is defined by three orthonormal vectors $T(\ell)$, $N_1(\ell)$, and $N_2(\ell)$, which satisfy the following differential equation:

$$\frac{d}{d\ell}\begin{bmatrix} T(\ell) \\ N_1(\ell) \\ N_2(\ell) \end{bmatrix} = \begin{bmatrix} 0 & k_1(\ell) & k_2(\ell) \\ -k_1(\ell) & 0 & 0 \\ -k_2(\ell) & 0 & 0 \end{bmatrix} \begin{bmatrix} T(\ell) \\ N_1(\ell) \\ N_2(\ell) \end{bmatrix}. \tag{4.1}$$

Relying on (4.1) and using simple kinematic relations, the angular velocity of the virtual vehicle is expressed as

$$\Omega^v_{vI} = \dot{\ell} \begin{bmatrix} 0 & -k_2 & k_1 \end{bmatrix}^T. \tag{4.2}$$

The error angles $\Lambda_{bv} = [\phi_E, \theta_E, \psi_E]^T$ define the rotation matrix $\mathcal{R}^v_b$ and satisfy the equations

$$\begin{aligned} \dot{\Lambda}_{bv} &= \mathcal{E}(\phi_E, \theta_E)\Omega^b_{bv} \\ &= \mathcal{E}(\phi_E, \theta_E)(\Omega^b_{bI} - \Omega^b_{vI}) \\ &= \mathcal{E}(\phi_E, \theta_E)(\Omega^b_{bI} - \mathcal{R}^b_v\Omega^v_{vI}). \end{aligned} \tag{4.3}$$

The position error $P^v_{bv} = [X_E, Y_E, z_E]^T$ satisfies the equations

$$P^v_{bv} = \mathcal{R}^v_I P^I_{bv}$$

$$\begin{aligned}\dot{P}_{bv}^{v} &= \dot{\mathcal{R}}_{I}^{v} P_{bv}^{I} + \mathcal{R}_{I}^{v} \dot{P}_{bv}^{I} \\ &= \mathcal{R}_{I}^{v}(\Omega_{Iv}^{I} \times P_{bv}^{I}) + \mathcal{R}_{I}^{v}(\dot{P}_{bI}^{I} - \dot{P}_{vI}^{I}) \\ &= -\Omega_{vI}^{v} \times P_{bv}^{v} + \mathcal{R}_{b}^{v}\mathcal{R}_{I}^{b}\dot{P}_{bI}^{I} - \begin{bmatrix} \dot{\ell} & 0 & 0 \end{bmatrix}^{T} \\ &= -\Omega_{vI}^{v} \times P_{bv}^{v} + \mathcal{R}_{b}^{v} V_{bI}^{b} - \begin{bmatrix} \dot{\ell} & 0 & 0 \end{bmatrix}^{T}. \end{aligned} \tag{4.4}$$

To complete the equations of motion for the UAS path-following dynamics, we constrain the progress of the virtual vehicle along its path with

$$\dot{\ell} = \kappa X_E + \begin{bmatrix} 1 & 0 & 0 \end{bmatrix} \mathcal{R}_{b}^{v} V_{bI}^{b}. \tag{4.5}$$

There are many suitable equations for $\dot{\ell}$. Constraining $\dot{\ell}$ with (4.5) can have the following interpretation: for any path, when the aircraft has no height or cross track errors ($Y_E = z_E = 0$) but bears a non-zero X_E, the evolution of X_E becomes

$$\begin{bmatrix} 1 & 0 & 0 \end{bmatrix} \dot{P}_{bv}^{v} = \dot{X}_E = -\kappa X_E. \tag{4.6}$$

Hence, $X_E = 0$ is an exponentially stable equilibrium point for (4.6) when $\kappa > 0$. Essentially, when there is a forward/backward error between the aircraft and the virtual vehicle, the virtual vehicle will smoothly speed up or slow down to reach the position of the aircraft. Such flexibility is important for an aircraft; in the presence of wind, an aircraft cannot both achieve its desired position while matching the other desired trim states. Allowing the virtual vehicle to accommodate such errors in X_E lends greater stability for the aircraft and provides improved performance in the remaining aircraft states.

The derivations previously given are inspired from the work in [29]. However, there is a crucial difference between these results and those from [29]. Therein, the position and angle

errors are defined to be between the virtual vehicle frame and a $\mathcal{W}'$ frame, which is *not* the body frame. The frame $\mathcal{W}'$ is defined by performing a vaguely specified rotation of the wind frame. Expressing the dynamics of the angle errors between $\mathcal{W}'$ and $\mathcal{F}_v$ requires rotation rates $[q_{\mathcal{W}'}, r_{\mathcal{W}'}]^T$ of $\mathcal{W}'$, quantities which cannot physically be measured. When the angle of attack and sideslip angle are small, $\mathcal{W}'$ approximates the body frame transformed by a roll rotation and $[q_{\mathcal{W}'}, r_{\mathcal{W}'}]^T$ approximates $[q_b, r_b]^T$. However, it is not our experience that the angle of attack and sideslip angle are negligible.

Commendably, the approach taken in [29] still produces working results in flight tests (see also [1]). Our work requires a model as accurate as reasonably possible to the true UAS dynamics. In our use of the model in [29], we found that the robustness results were sensitive to the controller design parameters and sometimes did not predict control failures which were observed in the simulation environment.

Given a virtual vehicle frame defined by (4.1), the path-following dynamics previously expressed hold for any 3D path. In this work, our case studies will be based off a 2D "racetrack" path. For planar paths, the dynamic equations simplify; $k_2(\ell)$ is identically zero, $k_1(\ell)$ can be interpreted as the inverse radius of curvature of the path at ℓ, and $[\phi_E, \theta_E, \psi_E]^T = [\phi, \theta, \psi - \psi_v]^T$, where ψ_v is the heading angle of the virtual vehicle. A straight line in the path is specified as $k_1(\ell) = 0$, and a turn in the path occurs when $k_1(\ell)$ is non-zero.

Following the works [1,29], we "inflate" the UAS error angles with approach angle functions. Specifically, we define

$$\theta_e = \theta_E - \theta_m \tanh\left(\frac{z_E}{C_\theta}\right) \qquad \psi_e = \psi_E - \psi_m \tanh\left(-\frac{Y_E}{C_\theta}\right) \tag{4.7}$$

The values for the parameters θ_m, C_θ, ψ_m, and C_ψ differ for the various controller schemes

studied in Section 4.5 (see Table 4.2).

Hence, the full path-following dynamic equations are

$$\dot{x}_p = f_p(x_p, d, u, k_1), \quad e = g(x_p, d, u), \quad y = h(x_p, d, u)$$

where $x_p := [(\Omega_{bI}^b)^T, (V_{bI}^b)^T, \Lambda_{bv}^T, (P_{bv}^v)^T, x_a^T]^T$, $d := [(V_{wI}^b)^T, \eta^T]^T$ is the exogenous disturbance composed of wind velocities and sensor noise η, $u = [u_E, u_A, u_R, u_T]^T := \delta^c$ is the control input, e is the performance output, and y is the sensor output. The state function $f_p(\cdot)$ is defined by (2.1), (2.2), (4.3), (4.4), and (4.5). The sensor output function is defined as

$$\begin{aligned} h(x, d, u) &= \Big[p_b, q_b, r_b, V_a, \phi_E, \theta_e, \psi_e, X_E, Y_E, z_E\Big]^T + W_\eta \eta \\ \eta &:= \Big[\eta_p, \eta_q, \eta_r, \eta_V, \eta_\phi, \eta_\theta, \eta_\psi, \eta_X, \eta_Y, \eta_z\Big]^T \\ W_\eta &:= \mathrm{diag}(0.01 I_3, 2, 0.01 I_3, 2 I_3) \end{aligned}$$

where W_η is a weighting matrix expressing the standard deviations of the measurement noise. The performance output function is defined as

$$\begin{aligned} g(x, d, u) &= W_e [x^T, u^T]^T \\ W_e &:= \mathrm{diag}(c_p, c_q, c_r, c_u, c_v, c_w, c_\phi, c_\theta, c_\psi, c_X, c_Y, c_z, c_{\delta_E}, c_{\delta_A}, c_{\delta_R}, c_{\delta_T}). \end{aligned}$$

Obtaining a linear parameter-varying (LPV) model parameterized by k_1 can be done following the approach in [1]. We first determine the trim states $x^\star(k_1)$ and $u^\star(k_1)$ such that

$$f_p(x^\star(k_1), 0, u^\star(k_1), k_1) = 0, \ (P_{bv}^v)^\star = 0, \ \& \ \psi_E^\star = 0. \tag{4.8}$$

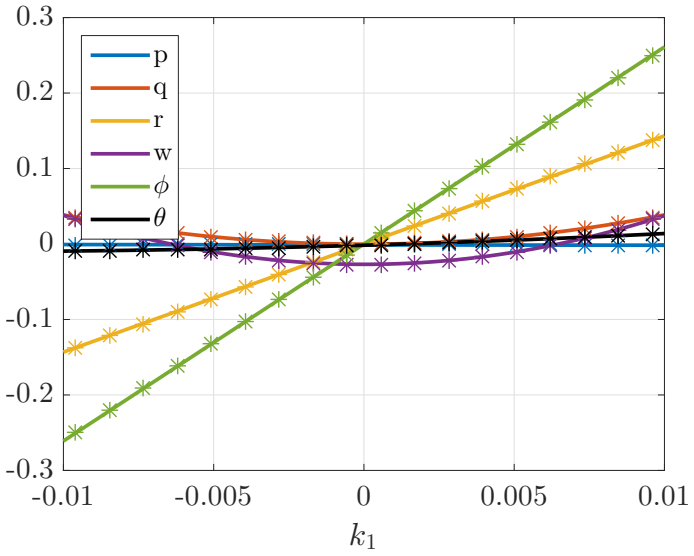

Figure 4.1: Gridded values ($*$) for $x^\star(k_1)$ and their fitted functions

Solving (4.8) for $x^\star(k_1)$ and $u^\star(k_1)$ is done using the MATLAB command `fsolve` for a grid of k_1 values. Polynomials are then fit to the gridded values for $x^\star(k_1)$ and $u^\star(k_1)$. By inspecting Fig. 4.1 and Fig. 4.2, it is apparent that the variables with significant dependence on k_1 are $\phi_E^\star(k_1)$, $r_b^\star(k_1)$, $\delta_A^\star(k_1)$, and $\delta_R^\star(k_1)$. Assuming the remaining variables are constant, the polynomial equations for $x_p^\star(k_1)$ and $u_p^\star(k_1)$ are

$$\begin{aligned}
\begin{bmatrix} p_b^\star & q_b^\star & r_b^\star(k_1) \end{bmatrix} &= \begin{bmatrix} 0 & 0 & 14.3k_1 \end{bmatrix} \text{ rad/s} \\
\begin{bmatrix} u_b^\star & v_b^\star & w_b^\star \end{bmatrix} &= \begin{bmatrix} 15.98 & 0.724 & -0.027 \end{bmatrix} \text{ m/s} \\
\begin{bmatrix} \phi_E^\star(k_1) & \theta_E^\star & \psi_E^\star \end{bmatrix} &= \begin{bmatrix} 26.1k_1 & -0.0017 & 0 \end{bmatrix} \text{ rad} \\
\begin{bmatrix} \delta_E^\star & \delta_A^\star(k_1) \end{bmatrix} &= \begin{bmatrix} 0.113 & -1.11k_1{+}0.004 \end{bmatrix} \text{ ms PWM} \\
\begin{bmatrix} \delta_R^\star(k_1) & \delta_T^\star \end{bmatrix} &= \begin{bmatrix} 1.17k_1{-}0.008 & 0.559 \end{bmatrix} \text{ ms PWM.}
\end{aligned}$$

An LPV model can now be defined for the path-following dynamics by the parameter-

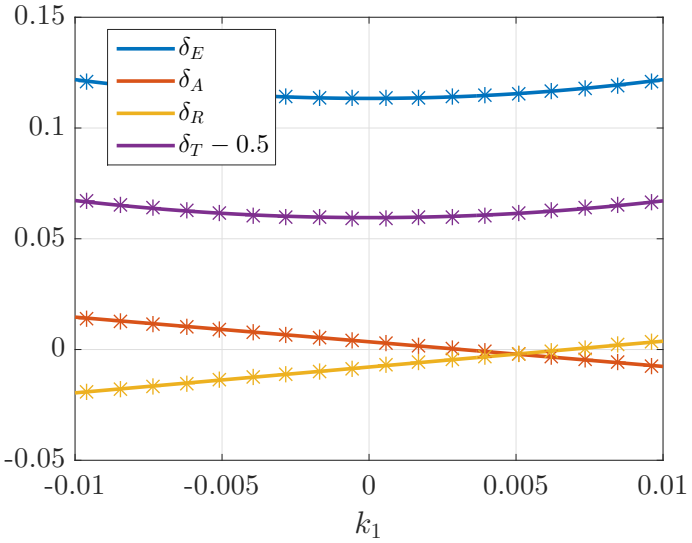

Figure 4.2: Gridded values ($*$) for $u^\star(k_1)$ and their fitted functions

dependent matrix-valued functions $A^c(k_1) := \frac{\partial f_p}{\partial x_p}\big|_{(x^\star,0,u^\star)}$, $B_1^c(k_1) := \frac{\partial f_p}{\partial d}\big|_{(x^\star,0,u^\star)}$, $B_2^c(k_1) := \frac{\partial f_p}{\partial u}\big|_{(x^\star,0,u^\star)}$, and so on. To express this LPV system as an LFT on k_1, each parameter-varying function must have rational dependence on k_1. This requirement is not exactly satisfied as $f_p(\cdot)$ has trigonometric functions on Λ_{bv}. However, given the bounds on the trim values $(\phi_E^\star, \theta_E^\star)$, these trigonometric functions can be adequately replaced in the parameter-varying matrices by the truncated Taylor series $\cos(\lambda^\star(k_1)) \approx 1 - \frac{1}{2}\lambda^\star(k_1)^2$ and $\sin(\lambda^\star(k_1)) \approx \lambda^\star(k_1)$ for $\lambda^\star = \phi_E^\star,\ \theta_E^\star$. By discretizing the continuous-time system with a sampling time $\tau = 0.04\,\mathrm{s}$ via Euler's method, the discrete-time LFT representation for the UAS path-following error dynamics can be expressed by

$$\begin{bmatrix} \bar{x}_p(k+1) \\ \varphi(k) \\ e(k) \\ \bar{y}(k) \end{bmatrix} = \begin{bmatrix} A_{ss} & A_{sp} & B_{1s} & B_{2s} \\ A_{ps} & A_{pp} & B_{1p} & B_{2p} \\ C_{1s} & C_{1p} & D_{11} & D_{12} \\ C_{2s} & C_{2p} & D_{21} & 0 \end{bmatrix} \begin{bmatrix} \bar{x}_p(k) \\ \vartheta(k) \\ d(k) \\ \bar{u}(k) \end{bmatrix} \tag{4.9}$$

$$\vartheta(k) = k_1 \varphi(k), \qquad \bar{x}_p(0) = 0.$$

Up to this point we have discussed the dynamics of a path-following UAS. Trajectory tracking occurs when the path progression $\ell(t)$ for the virtual vehicle is *explicitly* defined. A common trajectory-tracking expression for $\ell(t)$ is $\ell(t) = V_g t$, meaning the virtual vehicle progresses at a constant, desired ground speed regardless of the UAS position, thereby incorporating a known a priori timing constraint on the desired aircraft states and control inputs. With this perspective, trajectory tracking becomes a special case of path following, enforcing more stringent requirements on $\ell(t)$. Therefore, the UAS trajectory-tracking dynamics are

$$\dot{x}_t = f_t(x_t, d, u, k_1), \quad e = g(x_t, d, u), \quad y = h(x_t, d, u)$$

where $x_t := [(\Omega_{bI}^b)^T, (V_{bI}^b)^T, \Lambda_{bv}^T, (P_{bv}^v)^T, x_a^T]^T$, the state function $f_t(x_t, d, u, k_1)$ is defined by (2.1), (2.2), (4.3), (4.4), and $\dot{\ell} = V_g$. By linearizing $f_t(\cdot)$, $h(\cdot)$, and $g(\cdot)$ about $x^\star$ and $u^\star$ and following the same steps described previously for the path-following problem, an LFT representation of the UAS trajectory-tracking error dynamics can be obtained.

4.2 Controller synthesis and design methods

This subsection presents different controllers that are employed on the UAS. We apply $\mathcal{H}_\infty$ and $\mathcal{H}_2$ synthesis techniques for the path-following and trajectory-tracking models (4.9) when k_1 is set to zero. We also apply a PID controller for the path-following model.

Given an open-loop system G_{nom} defined by the equations

$$\begin{bmatrix} \bar{x}(k+1) \\ e(k) \\ \bar{y}(k) \end{bmatrix} = \begin{bmatrix} A & B_1 & B_2 \\ C_1 & D_{11} & D_{12} \\ C_2 & D_{21} & 0 \end{bmatrix} \begin{bmatrix} \bar{x}(k) \\ d(k) \\ \bar{u}(k) \end{bmatrix}, \quad \bar{x}(0) = 0 \tag{4.10}$$

and a controller K satisfying the equations

$$\begin{bmatrix} x^K(k+1) \\ \bar{u}(k) \end{bmatrix} = \begin{bmatrix} A^K & B^K \\ C^K & D^K \end{bmatrix} \begin{bmatrix} x^K(k) \\ \bar{y}(k) \end{bmatrix}, \; x^K(0) = 0$$

the corresponding closed-loop system M_{nom} is a mapping from the disturbances exhibited on the controlled UAS to the performance output of the controlled UAS. Using the work in [79], SDPs can be solved to obtain A^K, B^K, C^K, and D^K such that $\|\hat{M}_{\text{nom}}\|_\infty$ or $\|\hat{M}_{\text{nom}}\|_2$ is minimized. For completeness, the synthesis method is presented herein.

With matrix variables $P_f \in \mathbb{S}^n$, $P_g \in \mathbb{S}^n$, $W_f \in \mathbb{R}^{m\times n}$, $W_g \in \mathbb{R}^{n\times p}$, $W_h \in \mathbb{R}^{m\times p}$, and $L \in \mathbb{R}^{n\times n}$, define the matrices

$$\bar{P} := \begin{bmatrix} P_f & I \\ I & P_g \end{bmatrix}, \ \bar{A} := \begin{bmatrix} AP_f+B_2W_f & A+B_2W_hC_2 \\ L & P_gA+W_gC_2 \end{bmatrix}, \ \bar{B} := \begin{bmatrix} B_1+B_2W_hD_{21} \\ P_gB_1+W_gD_{21} \end{bmatrix}$$
$$\bar{C} := \begin{bmatrix} C_1P_f+D_{12}W_f & C_1+D_{12}W_hC_2 \end{bmatrix}, \ \bar{D} := \begin{bmatrix} D_{11}+D_{12}W_hD_{21} \end{bmatrix}.$$

An $\mathcal{H}_\infty$-optimal controller is obtained by solving the SDP

$$\begin{aligned} &\text{minimize } \mu \\ &\text{subject to} \\ &\qquad \begin{bmatrix} \bar{P} & 0 & \bar{A} & \bar{B} \\ 0 & \mu I & \bar{C} & \bar{D} \\ \bar{A}^T & \bar{C}^T & \bar{P} & 0 \\ \bar{B}^T & \bar{D}^T & 0 & \mu I \end{bmatrix} \succ 0 \end{aligned}$$

and setting

$$\begin{bmatrix} D^K & C^K \\ B^K & A^K \end{bmatrix} = \begin{bmatrix} I & 0 \\ B_2 & -P_g^{-1} \end{bmatrix} \begin{bmatrix} W_h & W_f \\ W_g & L-P_gAP_f \end{bmatrix} \begin{bmatrix} I & -C_2P_fS_f^{-1} \\ 0 & S_f^{-1} \end{bmatrix}. \tag{4.11}$$

The resulting closed-loop system M_{nom} satisfies $\|\hat{M}_{\text{nom}}\|_\infty = \mu$.

An $\mathcal{H}_2$-optimal controller is obtained by solving

$$\begin{aligned}&\text{minimize } \mu\\ &\text{subject to } \operatorname{trace}(R) \le \mu\\ &\qquad \begin{bmatrix} \bar{P} & \bar{A} & \bar{B} \\ \bar{A}^T & \bar{P} & 0 \\ \bar{B}^T & 0 & I \end{bmatrix} \succ 0, \quad \begin{bmatrix} R & \bar{C} & \bar{D} \\ \bar{C}^T & \bar{P} & 0 \\ \bar{D}^T & 0 & I \end{bmatrix} \succ 0\end{aligned}$$

and defining the controller state space matrices with (4.11). The resulting closed loop system M_{nom} satisfies $\|\hat{M}_{\text{nom}}\|_2^2 = \mu$. As a standard procedure for obtaining controller robustness, after solving the appropriate optimization SDP, μ is increased and the corresponding feasibility SDP is re-solved with the relaxed μ (see, for example, the discussion in [80]). In this chapter μ is relaxed such that the corresponding norm on M_{nom} is 250% that of the optimal value. The controller ultimately used is defined by (4.11) after solving the feasibility problem with the relaxed μ.

To demonstrate the uncertain UAS framework on a more popular control architecture, we also consider a PID controller for the path-following UAS. This follows from the architecture proposed by [81], with some slight modifications. The following controller is formed by successive loop closure of separate PID controllers for the lateral and longitudinal dynamics. For the ailerons, the states $\bar{\psi}_e$, $\bar{\phi}_E$, and $\bar{p}_b$ determine the control effort $\bar{\delta}_A$ by the equation

$$\hat{\bar{\delta}}_A(s) = \begin{bmatrix} -\left(K_\psi^p + \dfrac{K_\psi^i}{s}\right) K_\phi^p & -K_\phi^p & -K_\phi^d \end{bmatrix} \begin{bmatrix} \hat{\bar{\psi}}_e(s) \\ \hat{\bar{\phi}}_E(s) \\ \hat{\bar{p}}_b(s) \end{bmatrix}.$$

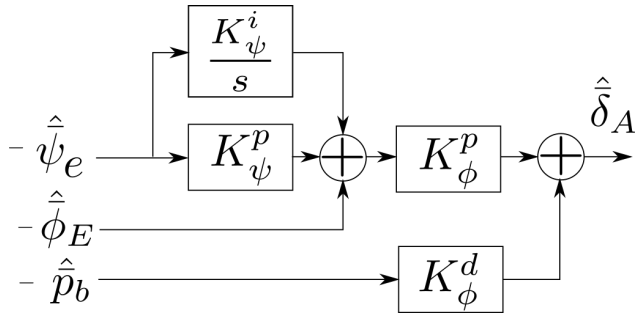

Figure 4.3: Continuous-time PID aileron control

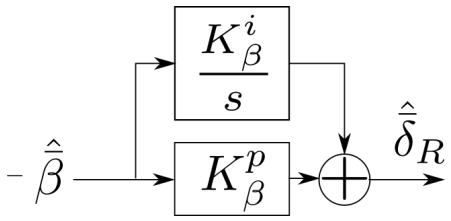

Figure 4.4: Continuous-time PI rudder control

The UAS sideslip angle β determines the control effort $\bar{\delta}_R$ by

$$\hat{\bar{\delta}}_R(s) = -\left(K_\beta^p + \frac{K_\beta^i}{s}\right)\hat{\bar{\beta}}(s).$$

Defining the UAS total energy as $E := gh + 1/2V_a^2$, the control effort $\bar{\delta}_T$ is determined with

$$\hat{\bar{\delta}}_T(s) = -\left(K_E^p + \frac{K_E^i}{s} + \frac{sK_E^d}{d_c s + 1}\right)\hat{\bar{E}}(s)$$

where $d_c = 0.1$ is a constant used to define a causal derivate in continuous-time. Defining the UAS energy distribution as $\varepsilon := gh - 1/2V_a^2$, the control effort $\bar{\delta}_E$ is determined from $\bar{\varepsilon}$, $\bar{\theta}_E$, and $\bar{q}$ with the equation

$$\hat{\bar{\delta}}_E(s) = \left[-\left(K_\varepsilon^p + \frac{K_\varepsilon^i}{s}\right)\left(K_\theta^p + \frac{K_\theta^i}{s}\right), \; -\left(K_\theta^p + \frac{K_\theta^i}{s}\right), \; -K_\theta^d\right] \begin{bmatrix} \hat{\bar{\varepsilon}}(s) \\ \hat{\bar{\theta}}_E(s) \\ \hat{\bar{q}}_b(s) \end{bmatrix}.$$

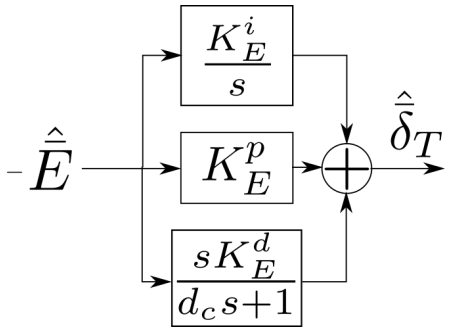

Figure 4.5: Continuous-time PID throttle control

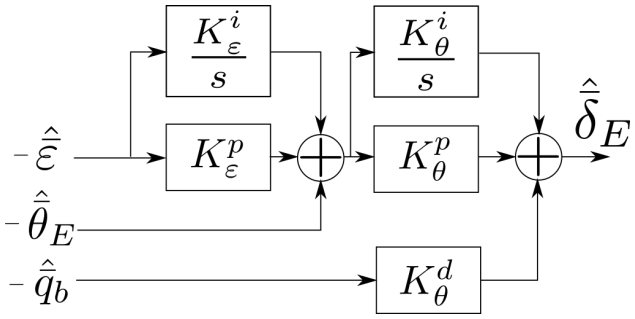

Figure 4.6: Continuous-time PID elevator control

Diagrams of these control laws are found in Figs. 4.3, 4.4, 4.5 and 4.6. As these control laws must be implemented in discrete-time, the bilinear transformation is applied to each Laplace equation. In state space form, the PID controllers for the elevator, aileron, rudder, and throttle are, respectively,

$$\hat{K}_E = \left[\begin{array}{c|ccc} 1 & -1 & 0 & 0 \\ \hline K_\varepsilon^i K_\theta^p \tau & -K_\theta^p\left(K_\varepsilon^p + \frac{K_\varepsilon^i \tau}{2}\right) & -K_\theta^p & -K_\theta^d \end{array}\right]$$

$$\hat{K}_A = \left[\begin{array}{cc|ccc} 1 & K_\psi^i & -K_\psi^p - \frac{K_\psi^i \tau}{2} & -1 & 0 \\ 0 & 1 & -1 & 0 & 0 \\ \hline K_\phi^i \tau & K_\psi^i\left(K_\phi^p + \frac{K_\phi^i \tau}{2}\right) & -\left(K_\phi^p + \frac{K_\phi^i \tau}{2}\right)\left(K_\psi^p + \frac{K_\psi^i \tau}{2}\right) & -K_\phi^p - \frac{K_\phi^i \tau}{2} & -K_\theta^d \end{array}\right]$$

$$\hat{K}_R = \left[\begin{array}{c|c} 1 & -1 \\ \hline K_\beta^i \tau & K_\beta^p + \dfrac{K_\beta^i \tau}{2} \end{array}\right]$$

$$\hat{K}_T = \left[\begin{array}{cc|c} 1 & \dfrac{2\tau d_c}{2d_c+\tau} & \dfrac{\tau d_c}{2d_c+\tau} \\ 0 & \dfrac{2d_c-\tau}{2d_c+\tau} & \dfrac{2d_c}{2d_c+\tau} \\ \hline -\dfrac{K_E^i \tau}{d_c} & \dfrac{2K_E^d \tau}{2d_c^2+\tau d_c} - K_E^i \tau & -K_E^p + \dfrac{K_E^i \tau}{2} + \dfrac{2K_E^d}{\tau+2d_c} \end{array}\right].$$

The final PID controller K mapping $\bar{y}$ to $\bar{u}$ is expressed as $\hat{K} = \text{diag}(\hat{K}_E, \hat{K}_A, \hat{K}_R, \hat{K}_T)$.

Finding a "good" set of penalty weights $[c_p, c_q, \ldots, c_{\delta_T}]$ for $\mathcal{H}_\infty$ and $\mathcal{H}_2$ controllers or gains $[K_\varepsilon^p, K_\varepsilon^i, \ldots, K_E^d]$ for PID controllers is a significant task for the controls engineer, and in Section 4.4 we will discuss improvements made to the tuning routine detailed in Section 3.3 in order to help tune these parameters such that the resulting controller has acceptable performance and robustness.

4.3 Modifications to uncertain UAS framework

The uncertain UAS considered in this chapter follows closely with that presented in 3.2. Similar to the approach in Chapter 3, uncertainties specific to certain subsystems are characterized, and the combination of these subsystems constitutes the closed-loop uncertain UAS (see Fig. 4.7). However, we make some modifications to the subsystem which expresses the UAS 6-DOF equations of motion.

The most significant change to the framework in this chapter is that the linear dynamic

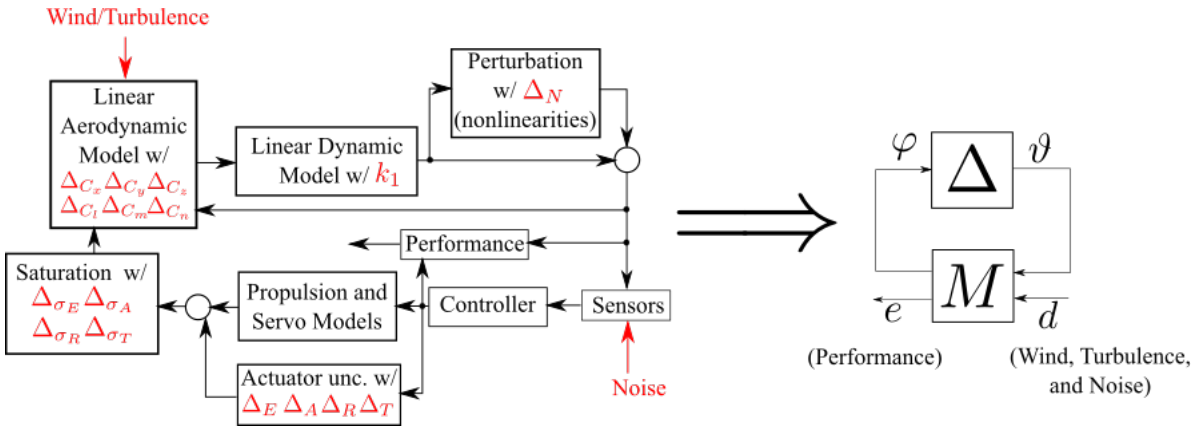

Figure 4.7: The uncertain UAS

Table 4.1: Type and bounds for UAS uncertainties

	Name	Type	Bounds
Actuator Model	Δ_E	DLTI	$\|\Delta_E\|_\infty \leq 0.05$
	Δ_A	DLTI	$\|\Delta_A\|_\infty \leq 0.05$
	Δ_R	DLTI	$\|\Delta_R\|_\infty \leq 0.05$
	Δ_T	DLTI	$\|\Delta_T\|_\infty \leq 0.2$
Saturation	Δ_{σ_E}	RB-SLTV	$0 \leq \Delta_{\sigma_E}(k) \leq 0.1, \quad -0.1 \leq \Delta_{\sigma_E}(k+1)-\Delta_{\sigma_E}(k) \leq 0.1$
	Δ_{σ_A}	RB-SLTV	$0 \leq \Delta_{\sigma_A}(k) \leq 0.1, \quad -0.1 \leq \Delta_{\sigma_A}(k+1)-\Delta_{\sigma_A}(k) \leq 0.1$
	Δ_{σ_R}	RB-SLTV	$0 \leq \Delta_{\sigma_R}(k) \leq 0.1, \quad -0.1 \leq \Delta_{\sigma_R}(k+1)-\Delta_{\sigma_R}(k) \leq 0.1$
	Δ_{σ_T}	RB-SLTV	$0 \leq \Delta_{\sigma_T}(k) \leq 0.1, \quad -0.1 \leq \Delta_{\sigma_T}(k+1)-\Delta_{\sigma_T}(k) \leq 0.1$
Aerodynamic Model	Δ_{C_x}	RB-SLTV	$-0.054 \leq \Delta_{C_x}(k) \leq 0.026, \quad -0.014 \leq \Delta_{C_x}(k+1)-\Delta_{C_x}(k) \leq 0.006$
	Δ_{C_y}	RB-SLTV	$-0.045 \leq \Delta_{C_y}(k) \leq 0.037, \quad -0.01 \leq \Delta_{C_y}(k+1)-\Delta_{C_y}(k) \leq 0.01$
	Δ_{C_z}	RB-SLTV	$-0.113 \leq \Delta_{C_z}(k) \leq 0.119, \quad -0.042 \leq \Delta_{C_z}(k+1)-\Delta_{C_z}(k) \leq 0.024$
	Δ_{C_l}	RB-SLTV	$-0.022 \leq \Delta_{C_l}(k) \leq 0.026, \quad -0.012 \leq \Delta_{C_l}(k+1)-\Delta_{C_l}(k) \leq 0.009$
	Δ_{C_m}	RB-SLTV	$-0.12 \leq \Delta_{C_m}(k) \leq 0.125, \quad -0.046 \leq \Delta_{C_m}(k+1)-\Delta_{C_m}(k) \leq 0.035$
	Δ_{C_n}	RB-SLTV	$-0.006 \leq \Delta_{C_n}(k) \leq 0.006, \quad -0.001 \leq \Delta_{C_n}(k+1)-\Delta_{C_n}(k) \leq 0.003$
UAS Dyn.	Δ_N	NB	$\|\Delta_N\|_{\ell_2\to\ell_2} \leq 0.01$
	k_1	SLTV	$-0.005 \leq k_1(k) \leq 0.005$

equations of motion are derived in part from (4.3) and (4.4), rather than (2.3) and (2.4). This is to enable the analysis of path-following dynamics as derived in Section 4.1. Furthermore, by relying on (4.3) and (4.4) we can easily incorporate the effect of the desired path's inverse radius of curvature k_1 on the UAS dynamics. This introduces a new uncertainty that was not considered in Chapter 3. As an additional change, we do not incorporate the parametric uncertainties Δ_m, Δ_x, Δ_z, Δ_{I_x}, Δ_{I_y}, Δ_{I_z} in the UAS dynamics. Though they theoretically may be incorporated, all six uncertainties along with k_1 formulated an LFT which presented too large of a computational burden to apply the coprime factors reduction method discussed in Section 3.2.3. We anticipate that as computational capabilities increase, all seven uncertainties may be considered together. However, for the present work we find it more valuable to enable analysis of the UAS conducting a *suite* of maneuvers, which is accomplished by incorporating k_1 as an SLTV uncertainty.

As an additional change to the uncertainties in the UAS dynamics, we modify the uncertainty Δ_N to be a (possibly time-varying and/or nonlinear) NB uncertainty, rather than a DLTI uncertainty. This is more fitting, as Δ_N represents the nonlinear effects lost when linearizing the UAS equations of motion. Along with this change, we modify the matrix W_N introduced in Section 3.2.3 to be $W_N = \text{diag}(1, 1, 1, 5, 5, 5, 0.4, 0.4, 0.4, 10, 10, 2)$, since the UAS in this chapter is flying at trim points different from the one utilized in Chapter 3. In light of these modifications to the uncertain UAS framework, Table 4.1 presents all the uncertainties, their types, and their bounds.

4.4 Improvements to tuning routine

This section discusses improvements that have been made to the tuning routine proposed in Section 3.3. As mentioned previously, the proposed routine is not to be viewed as a math-

ematically rigorous IQC synthesis method. It is a heuristic algorithm that has repeatedly been shown in simulation and flight tests to provide a controller with improved robust performance. This routine applies gradient-based optimization of the robust performance of an interconnection, where (M, Δ) is parameterized by the controller design parameters $c \in \mathbb{R}^{n_c}$. For $\mathcal{H}_\infty$ and $\mathcal{H}_2$ synthesis problems, the controller design parameters are

$$c = [c_p,\ c_q,\ c_r,\ c_{V_a},\ c_\phi,\ c_\theta,\ c_\psi,\ c_X,\ c_Y,\ c_z,\ c_{\delta_E},\ c_{\delta_A},\ c_{\delta_R},\ c_{\delta_T}]^T$$

which denote the penalty weights in W_e defining the UAS performance output e in (4.10). For PID control, the parameters are

$$c = [K_\varepsilon^p,\ K_\varepsilon^i,\ K_\theta^p,\ K_\theta^i,\ K_\theta^d,\ K_\psi^p,\ K_\psi^i,\ K_\phi^p,\ K_\phi^d,\ K_\beta^p,\ K_\beta^i,\ K_E^p,\ K_E^i,\ K_E^d]^T.$$

Given the control parameters c, the controller design procedure $\text{DesignCTR}(c) = K$ outlined in Section 4.2, and the open-loop interconnection (G, Δ) satisfying

$$\begin{bmatrix} \varphi \\ e \\ \bar{y} \end{bmatrix} = \begin{bmatrix} G_{11} & G_{12} & G_{13} \\ G_{21} & G_{22} & G_{23} \\ G_{31} & G_{32} & G_{33} \end{bmatrix} \begin{bmatrix} \vartheta \\ d \\ \bar{u} \end{bmatrix}, \quad \vartheta = \Delta\varphi \tag{4.12}$$

this routine seeks control parameters c such that the closed-loop interconnection $(M, \Delta) = (\text{CloseLP}(G, K), \Delta)$ has locally optimal robust performance. Achieving this objective is attempted by iteratively estimating the gradient* of the robust performance over the controller parameter space and then traveling in a direction of descent. The gradient for the robust performance is numerically estimated by solving for the robust performance of the intercon-

*We recognize that in many cases the mapping from c to γ is not a function, much less smooth. Our references to its gradient and Hessian are informal.

nection at small variations of c and conducting finite difference approximations.

This chapter implements some additional subroutines that improve on the algorithm in Section 3.3. These include stepping in an improved descent direction by estimating the Hessian of the robust performance (lines 10-13 in Algorithm 2), and conducting a line search to find the best step size given a certain direction (line 15 in Algorithm 2). Whereas Algorithm 1 is a steepest-descent algorithm with fixed step size, this chapter implements the quasi-Newton BFGS method with a line search for finding the locally optimal robust performance [82]. The essential modifications to Algorithm 1 consist of replacing line 8 with the lines 8-16 in Algorithm 2. The line search algorithm is not explicitly given in Algorithm 2, as a variety of subroutines might be used. In this chapter, the line search is accomplished by calculating the γ-value for a variety of step sizes $\widetilde{dc}$ which are less than the maximum step $\widetilde{dc}_{\max}$ and selecting the step size which yields the greatest reduction of γ. Though this is computationally expensive, this work employs parallel processing across multiple CPUs, thereby providing many γ-values within the same time it would take to calculate one γ-value. This approach also guarantees that each iteration will either reduce the subsequent γ-value or become the final iteration. These enhancements aid in decreasing the solution time and improving the robustness of the final controller.

In order to conduct IQC analysis, the nominal closed-loop system M must be stable. Though $\mathcal{H}_\infty$ and $\mathcal{H}_2$ controllers guarantee a stabilized system (as far as the LMIs can be satisfied), the PID controller may not stabilize the nominal system. It is then problematic if the tuning routine seeks to make a step in the parameter space such that the closed-loop system is unstable. This is one reason why we implement a line search and query multiple step sizes once the direction of descent is determined.

Because the tuning routine must solve many SDPs, the definition of (M, Δ) and the problem parameters used in IQC analysis (such as pole locations λ, a_i or basis lengths of the multipliers

Algorithm 2 Tuning routine via IQC analysis

Inputs: Initial controller parameters $c \in \mathbb{R}^{n_c}$ and open-loop LFT (G, Δ) satisfying the system equations

$$\begin{bmatrix} \varphi \\ e \\ y \end{bmatrix} = \begin{bmatrix} G_{11} & G_{12} & G_{13} \\ G_{21} & G_{22} & G_{23} \\ G_{31} & G_{32} & G_{33} \end{bmatrix} \begin{bmatrix} \vartheta \\ d \\ u \end{bmatrix}, \quad \vartheta = \Delta\varphi$$

Outputs: Final controller parameters c and γ for the closed-loop LFT (M, Δ)

Define γ_{tol} and dc (optimization tolerance and gradient step size)

$\gamma \leftarrow \overline{\text{IQC}}(c, G, \Delta)$, i.e. $\begin{cases} K \leftarrow \text{DesignCTR}(c) \\ M \leftarrow \text{CloseLP}(G, K) \\ \gamma \leftarrow \text{IQC}(M, \Delta) \end{cases}$

while 1 **do**
  for $i = 1 : n_c$ **do** # estimate gradient
    $c^+ \leftarrow [c_1, \ldots, c_i + dc, \ldots, c_{n_c}]^T$
    $\gamma_i^+ \leftarrow \overline{\text{IQC}}(c^+, G, \Delta)$
  $\nabla\gamma \leftarrow [\gamma_1^+ - \gamma, \ldots, \gamma_{n_c}^+ - \gamma]^T$
  if first iteration **then**
    $H \leftarrow I_{n_c}$
  else # estimate Hessian
    $s \leftarrow \nabla\gamma - \nabla\gamma_0$
    if $s^T \widetilde{dcp} > 0$ **then**
      $H \leftarrow H + \frac{ss^T}{s^T \widetilde{dcp}} - \frac{Hpp^T H}{p^T H p}$
  $\widetilde{p} \leftarrow -H^{-1}\nabla\gamma$ # find step direction
  $\widetilde{dc} \leftarrow \text{LineSearch}(p, c, G, \Delta)$
  $c \leftarrow c + \widetilde{dcp}$
  $\gamma^+ \leftarrow \overline{\text{IQC}}(c, G, \Delta)$
  if $\gamma^+ - \gamma < \gamma_{\text{tol}}$ **then**
    exit while loop
  $\nabla\gamma_0 \leftarrow \nabla\gamma$
  $\gamma = \gamma^+$

$\hat{\Psi}$ and $\hat{\Theta}$) are selected to reduce the computational complexity of the SDP (2.14). After the tuning routine is finished, IQC analysis is repeated with modified problem data and parameters to reflect the most accurate model of the uncertain UAS and obtain the least conservative robust performance result. To ensure consistency, both the tuning routine and final analysis construct (M, Δ) with the same uncertain open-loop system (G, Δ). Though (G, Δ) remains unchanged, M may be defined differently to express different performance outputs or disturbance inputs.

It cannot be overstated that this work employs different penalty weights W_e to define the performance output e in (3.2) and (4.10). In the final certification of a UAS, IQC analysis is conducted by defining

$$e = e_{\text{ce}} := \begin{bmatrix} \bar{X}_E & \bar{Y}_E & \bar{z}_E \end{bmatrix}^T. \tag{4.13}$$

Tuning a controller to minimize the robust performance with e_{ce} has been found to produce a final controller with good position tracking, but at the expense of executing undesirably aggressive maneuvers. To address this issue, the performance output defined while *tuning* a controller via IQC analysis is

$$e = e_{\text{tu}} := \begin{bmatrix} \bar{p}_b & \bar{q}_b & \bar{r}_b & \bar{u}_b & \bar{v}_b & \bar{w}_b & \bar{\phi}_E & \bar{\theta}_E & \bar{\psi}_E & \bar{X}_E & \bar{Y}_E & \bar{z}_E \end{bmatrix}^T. \tag{4.14}$$

The added penalties on the remaining states of the UAS ensure that close position tracking is still achieved while reducing deviations in the other states. Finally, the tuning routine for $\mathcal{H}_2$ and $\mathcal{H}_\infty$ controllers searches for the penalty weights defining e to synthesize a controller which yields an interconnection with improved robust performance. Hence, the definition of e for (4.10) changes at each iteration in the tuning routine.

Table 4.2: Approach angle parameters for each controller type

Controller type	θ_m	C_θ	ψ_m	C_ψ
PFH_2	20 deg	14	30 deg	20
PFH_∞	20 deg	14	30 deg	20
TTH_2	0	—	0	—
TTH_∞	0	—	0	—
PFpid	—	—	20 deg	30

4.5 Results

This section explores how the tuning routine previously described produced TT$\mathcal{H}_\infty$, TT$\mathcal{H}_2$, PF$\mathcal{H}_\infty$, PF$\mathcal{H}_2$, and PFpid controllers. We then present how subsequent IQC analysis on each controlled UAS can be used to compare their performance. These predictions are then validated with data from simulations and flight tests. Finally, the relative merits and weaknesses of each controller scheme (trajectory-tracking/path-following and $\mathcal{H}_\infty$/$\mathcal{H}_2$/PID) are discussed by inspecting IQC analysis, simulation, and flight test results.

For the ensuing results, the IQC analysis SDP (2.14) was solved using YALMIP/CSDP [74, 83] via 64-bit MATLAB R2015a on a computer with 128GB of RAM and 2 Intel Xeon E5-2683 2.10 GHz CPUs (16 cores per CPU). Solution times were from 2-4 min. For a standard Dell desktop with 6GB of RAM and an Intel Xeon W3550 (3.07GHz), solution times ranged from 3 to 8 min. Two factors determined our choice of CSDP to solve the IQC analysis SDP. First, CSDP efficiently handles moderately sized SDPs; the IQC analysis SDPs in this chapter have 9,000-13,000 decision variables and take longer for SeDuMi or SDPT3 to solve than CSDP. Second, the resulting SDPs were not always numerically well-conditioned and, unlike MOSEK, CSDP was capable of consistently returning feasible solutions in the presence of poorly conditioned problems.

Table 4.3: IQC analysis results and number of iterations when tuning all five controller types. All ϵ values for final IQC analysis results are 1 (i.e., $\epsilon^{\text{final}} = 1$)

Type	PFH_2	PFH_∞	PFpid	TTH_2	TTH_∞
ϵ^{init}	0.1	0.15	0.12	0.1	0.3
$\gamma_{\text{IQC}}^{\text{init}}$	5.64	10.69	6.97	3.49	81.6
Iterations	79	44	36	68	83
$\gamma_{\text{IQC}}^{\text{final}}$	7.52	3.0	34.5	7.43	3.38

Table 4.4: Controller parameters before and after the tuning routine

Type	Init/ Final	c_p/K_ψ^p	c_q/K_ψ^i	c_r/K_ϕ^p	c_{V_a}/K_ϕ^i	c_ϕ/K_ϕ^d	c_θ/K_ε^p	c_ψ/K_ε^i	c_X/K_θ^p	c_Y/K_θ^d	c_z/K_E^p	c_{δ_E}/K_E^i	c_{δ_A}/K_E^d	c_{δ_R}/K_β^p	c_{δ_T}/K_β^i
PFH_2	Init	0	0	0.2	0	0	0	0	1	1	1	0.01	0.01	0.01	0.1
	Final	0	0	0	0.1	0.16	0.01	0.14	0.7	0.11	0.01	0.01	0.03	0.02	0.21
PFH_∞	Init	0	0	0.2	0	0	0	0	1	1	1	0.01	0.01	0.01	0.1
	Final	0.13	0.34	0.22	0.22	0.06	0.1	0.09	0.83	0.13	0.16	0.02	0.17	0.13	0.19
PFpid	Init	0.75	0.01	0.5	0	0	0.5	0.05	0.3	0	0.2	0.05	0	-0.02	-0.01
	Final	0.79	0.08	0.62	0.08	0.1	0.37	0.01	0.48	0.04	0.2	0.09	0	-0.03	0
TTH_2	Init	0	0	0.2	0	0	0	0	1	1	1	0	0	0	0.1
	Final	0	0	0.11	0	0.23	0.17	0.03	1.0	0.2	0.01	0.12	0.14	0.01	0.32
TTH_∞	Init	0	0	0.2	0	0	0	0	1	1	1	0.01	0.01	0.01	0.1
	Final	0.25	0.71	0.41	0.26	0.19	0.03	0.16	0.2	0.14	0.15	0.06	0.01	0.21	0.25

Along with the aforementioned controller design parameters, it would have been possible to tune the parameters defining the approach angle functions (4.7). However, including these additional parameters in the tuning routine would increase the computational complexity. Since the previously mentioned controller design parameters already directly effect the UAS position error, we opted not to tune the parameters in (4.7) when executing Algorithm 2. The values of these parameters pertaining to each controller scheme are provided in Table 4.2.

4.5.1 Tuning results

As previously discussed, the IQC tuning routine is concerned with finding optimal values for the parameters c that define a controller. For $\mathcal{H}_\infty$ and $\mathcal{H}_2$ synthesis problems, c defines

the penalty weights W_e which specify e in (4.10). For PID controllers, c determines the PID gains in $\hat{K}_E$, $\hat{K}_A$, $\hat{K}_R$, and $\hat{K}_T$. After obtaining a controller and closing the loop in the routine, we set the performance output $e = e_{\text{tu}}$ in (3.2), as given in (4.14), and then conduct IQC analysis. In the tuning routine, all uncertainties described in Section 4.3 and Table 4.1 are considered, the disturbance d is defined as $d := [(V_{wI}^b)^T, \eta^T]^T$, and each scalar noise signal η_i that composes η is characterized as an element of $\mathcal{D}_w$. In other words, we apply 10 "banded white" signal IQC multipliers for the disturbance d, one multiplier to each sensor noise channel. To reduce the computational complexity, we do not characterize the wind disturbances u_w, w_w, or v_w with signal IQC multipliers, although this characterization is incorporated in Section 4.5.2. The IQC analysis problem parameters are set as $b = 2$, $\lambda = -0.6$, $\omega_0 = \pi$, and $[a_1, a_2, a_3, a_4] = [-0.9, -0.2, 0.5, 0.9]$, where a_i are the poles of the basis function in (2.18). The $\mathcal{H}_2$ and $\mathcal{H}_\infty$ synthesis SDPs are solved using SeDuMi [84].

Unlike the initial controller in Chapter 3, all five initial controllers in this work produced an interconnection (M, Δ) such that the SDP (2.14) was infeasible. In order to start the tuning routine, we first applied Algorithm 2 to an initial controller parameterized by c, the nominal system G, and a *scaled back* uncertainty block $\epsilon\Delta$, with $\epsilon < 1$. Once the routine converged to a controller, ϵ was then increased and Algorithm 2 was restarted. This process repeated until $\epsilon = 1$, in which the final controller provided improved robust performance for the uncertainty bounds previously given in Table 4.1. The initial ϵ (ϵ^{init}) and the robust performance for each controller type are given in Table 4.3. The controller parameters before and after running the tuning routine are shown in Table 4.4.

While implementing the tuning routine, it became clear that the PID controller gave relatively poor robust performance. As a result, we had to relax the problem in the PID controller case by constraining k_1 to be within the interval $[-0.0035, 0.0035]$, rather than the interval previously given in Table 4.1. Thus, the IQC analysis results for the PID controller

pertain to an uncertain UAS flying any level path whose radius of curvature is no less than 285 m, rather than 200 m.

4.5.2 Predicting flight performance via IQCs and simulations

In this section, we demonstrate how IQC analysis can be used in the certification process of a UAS flight controller. We conduct detailed IQC analysis on, run simulations of, and perform flight tests for the UAS interconnected with a specified controller. The resulting robust $\mathcal{D}$-to-ℓ_2-gain performance level for each controller is compared with the $\mathcal{D}$-to-ℓ_2 induced gains calculated in simulation and flight tests. The performance output e in this section is defined as $e = e_{\text{ce}}$ from (4.13), relating to the certification of the UAS controller's position tracking performance. The problem parameters in Section 4.5.1 are also used for IQC analysis in this section, except that λ is set to either 0.932 or 0.53.

As noted previously, the tuning routine conducted IQC analysis on (M, Δ) without characterizing wind disturbances via signal IQCs. This is akin to finding the degradation in performance when the wind disturbance can be any ℓ_2 signal. Unless users desire that the controlled flight persists indefinitely, such an assumption is quite broad and considers wind disturbances that are not reflected in reality. An accepted approach consists of dividing atmospheric disturbances into a constant portion and turbulent form [85], where the turbulent form is specified by the output of a Dryden turbulence model injected by white Gaussian noise with unit variance. Specifically, given the Dryden turbulence models H_u, H_v, and H_w from [86], we characterize the wind disturbances as

$$\begin{bmatrix} \hat{u}_w(z) \\ \hat{v}_w(z) \\ \hat{w}_w(z) \end{bmatrix} = \begin{bmatrix} \hat{H}_u(z) & 0 & 0 \\ 0 & \hat{H}_v(z) & 0 \\ 0 & 0 & \hat{H}_w(z) \end{bmatrix} \begin{bmatrix} \hat{u}_t(z) \\ \hat{v}_t(z) \\ \hat{w}_t(z) \end{bmatrix} + \begin{bmatrix} \hat{u}_c(z) \\ \hat{v}_c(z) \\ 0 \end{bmatrix}$$

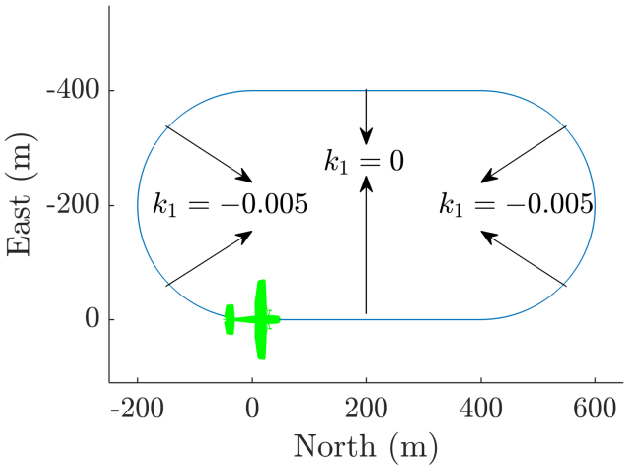

Figure 4.8: Racetrack path for simulation and flight tests

where $H_{\text{dry}} := \text{diag}(H_u, H_v, H_w)$, $V_t = H_{\text{dry}}[u_t,\ v_t,\ w_t]^T$ represents wind turbulence, and $[u_c,\ v_c]^T$ represent disturbances due to constant wind. We do not include a steady wind in the vertical direction, which is reasonable for low altitude flights with paths that are hundreds of meters long. The Dryden turbulence models are characterized at low altitude with the scale length, wind velocity, and airspeed defined by $L_u = 250\,\text{ft}$, $u_{20} = 30\,\text{knots}$, and $V = 52.5\,\text{ft/s}$, respectively. The steady wind disturbances u_c and v_c can be approximately characterized with the "banded" signal IQC multipliers Φ_b that have a narrow frequency band centered at $\omega = 0$. In the following results, we set $\omega_b = 0.015\,\text{Hz}$. The Dryden model inputs u_t, v_t, and w_t can be characterized with the "banded white" signal IQC multipliers Φ_w whose band is defined by $\omega_0 = \pi$. This is the same characterization used for sensor noise disturbances. By redefining the disturbance input as $d := [u_c, v_c, u_t, v_t, w_t, \eta^T]^T$ and using two IQC multipliers $\Phi \in \Phi_b$ to characterize u_c and v_c and thirteen IQC multipliers $\Phi \in \Phi_w$ to characterize the remaining channels in d, we repeat IQC analysis on the closed-loop UAS for each controller.

Along with IQC analysis, we conduct nonlinear simulations of the UAS flying a racetrack path (see Fig. 4.8). This is done by calling `ode23` in MATLAB to solve (2.1), (2.2), (2.3),

(2.4) and implementing a discrete-time controller. The virtual vehicle position and attitude are defined by the racetrack path and evolve with time by applying Euler's method on the pertinent $\dot{\ell}$ equation. The error states ϕ_E, θ_E, ψ_E, X_E, y_E, and z_E are calculated by the difference between the simulated UAS and the virtual vehicle position and Euler angles. Uncertainty in each aerodynamic coefficient C_i is included by adding a pseudo-random sequence $\Delta_{C_i}(k)$, generated with a uniform distribution, whose bounds and rate limits are shown in Table 4.1. Each actuator is modeled using the second-order system (2.6), and each servo includes a pseudo-randomly generated transfer function whose $\mathcal{H}_\infty$ norm respects the bounds previously given in Table 4.1. Wind disturbance is generated with a steady 3 m/s component and the aforementioned Dryden turbulence model. A simulated flight consists of executing a single racetrack, which is approximately 2 min of flight time. For a simulation with N_k time steps, the associated γ-value is calculated by

$$\gamma_{\text{sim}}^2 = \left(\sum_{k=0}^{N_k-1} e(k)^T e(k) \right) / \left(\sum_{k=0}^{N_k-1} d(k)^T d(k) \right)$$

having an obvious relation to the finite-horizon $\mathcal{D}$-to-ℓ_2 induced gain.

As a final comparison to the predictions from IQC analysis, we conduct flight tests using the Senior Telemaster Plus (94 in wingspan) aircraft—see Fig. 4.9. The test platform autopilot consists of a Gumstix Overo Fire [87] and 3DR Pixhawk [88]. The Gumstix calculates the controller's commanded actuation, propagates the virtual vehicle, and stores flight data, while the Pixhawk performs sensor fusion, task management, and communication interfaces. The Gumstix sends the commanded actuation to and receives sensor data from the Pixhawk via a serial link. Along with the Pixhawk internal sensors, the Telemaster uses a u-blox NEO-7 GNSS module to measure position and velocities, a differential pressure sensor (4525DO) to measure airspeed, and an in-house five-hole probe to measure the angle of attack and sideslip angle. Using this sensor suite, all the states necessary to implement the controller and

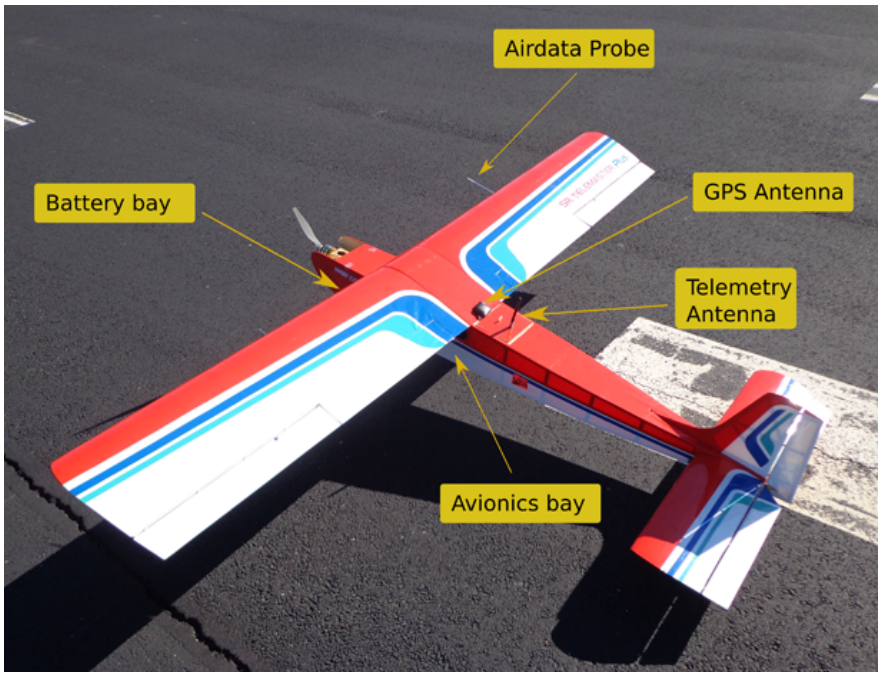

Figure 4.9: UAS test platform (photo credit [1])

propagate the virtual vehicle are measured. Videos pertaining to flight tests implementing each controller can be found at `http://www.dept.aoe.vt.edu/~farhood/ctrFlight.html`.

Calculating the γ-value in the simulation environment is relatively simple since the signals d and e are precisely known. In contrast, during flight tests the wind disturbance and signal noise cannot be exactly known. We therefore obtain an estimated γ-value from flight by

$$\gamma_{\text{flt}}^2 = \rho_e^2/(\rho_n^2 + \rho_c^2 + \rho_t^2)$$

where ρ_e, ρ_n, ρ_c, and ρ_t are, respectively, the finite-horizon ℓ_2 norms of the estimated UAS performance output, sensor noise, steady wind disturbance, and inputs to the Dryden turbulence model. The performance output is estimated by filtering the position error calculated in flight, and the sensor noise is calculated by taking the difference of filtered and raw sensor data. Though we do not have a clean measurement of the wind vector at each time step,

we can still calculate ρ_c and ρ_t by inferring the constant wind component and the energy of the turbulent wind component. Since the flight path is periodic and conducted multiple times in a single flight, the magnitude, direction, and energy of the constant wind V_c can be estimated.

The energy of the input to the Dryden turbulence model is determined by the duration of the flight segment for each γ-value. The Dryden turbulence model assumes that the input signals u_t, v_t, w_t to $\hat{H}_u(z)$, $\hat{H}_v(z)$, and $\hat{H}_w(z)$ are of unit variance. Given a flight segment with N_{flt} time steps, as N_{flt} becomes large, we can approximate the ℓ_2 norm of each input signal by $\|u_t\|_{\ell_2} = \|v_t\|_{\ell_2} = \|w_t\|_{\ell_2} = \sqrt{N_{\text{flt}}}$, providing the approximation $\rho_t = \sqrt{3N_{\text{flt}}}$. This is a suitable approximation, as a single racetrack loop consists of thousands of time steps. Another method of approximating the energy of $[u_t, v_t, w_t]^T$ would consist of lower bounding the norm of the turbulent wind V_t via the inequality

$$\|V_{bw}^b\| - \|V_{bI}^b - V_c\| \leq \|V_t\|$$

to calculate a lower bound on the energy of the input signal $[u_t, v_t, w_t]^T$ via the equation

$$\|V_t\| = \frac{\|\hat{H}_{\text{dry}}\|_2}{\sqrt{3}} \| \begin{bmatrix} u_t & v_t & w_t \end{bmatrix}^T \|.$$

However, even though V_c can be reliably estimated and our platform can measure $\|V_{bw}^b\|$ and V_{bI}^b with an airspeed sensor and a GNSS module, we found that the resulting lower bound on ρ_t was dependent on the orientation of the aircraft with respect to the constant wind. We believe this is due to the utilization of a single airspeed sensor located on the right wing. The aircraft body then produces an asymmetric distortion of wind measurements, thereby asymmetrically affecting our approximations of ρ_t. For this reason, we choose to utilize the former approximation to ρ_t, which is consistent with the assumptions implemented in IQC

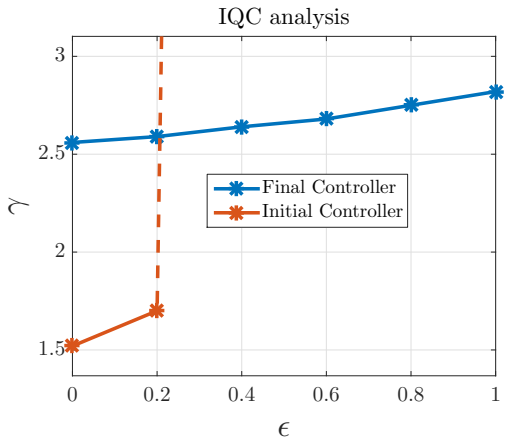

Figure 4.10: Robust $\mathcal{D}$-to-ℓ_2-gain performance levels for PF$\mathcal{H}_\infty$ controllers

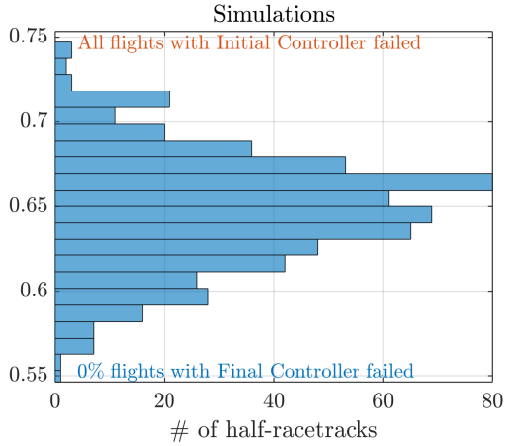

Figure 4.11: Distribution of $\mathcal{D}$-to-ℓ_2 induced gains for PF$\mathcal{H}_\infty$ controllers in an uncertain simulation environment

analysis and the uncertain simulation environment.

Given one of the controllers from Section 4.5.1, we are now ready to compare the performance predicted by IQC analysis and simulations with that experienced in flight tests. We first step through observations from the PF$\mathcal{H}_\infty$ controllers. The IQC analysis results for both the initial and final PF$\mathcal{H}_\infty$ controllers are given in Fig. 4.10. Distributions of the calculated γ-values from simulation and flight tests are shown in Fig. 4.11 and Fig. 4.12, respectively.

Observing Fig. 4.10, we see that the initial controller's nominal $\mathcal{D}$-to-ℓ_2-gain performance

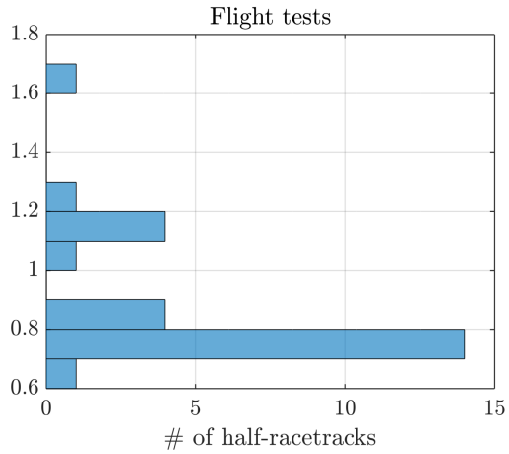

Figure 4.12: Distribution of $\mathcal{D}$-to-ℓ_2 induced gains for a PF$\mathcal{H}_\infty$ controller during flight tests

level (the robust $\mathcal{D}$-to-ℓ_2-gain performance level when $\epsilon = 0$) is superior to that of the final controller. This makes sense, as the performance output used to synthesize the initial controller almost exclusively penalizes position error. However, as the effect of uncertainties increases, the initial controller's performance rapidly degrades until (at $\epsilon = 0.4$) analysis cannot provide a robust $\mathcal{D}$-to-ℓ_2-gain performance level. Conversely, the final controller has a robust performance of 2.82 when $\epsilon = 1$. With these observations, a systems engineer can surmise that the final controller is ultimately superior to the initial controller, and the initial controller should not be used in flights. These conclusions are confirmed via results from the uncertain simulation environment. When simulating the initial controller, every flight eventually diverged from the path and ultimately resulted in loss of control. In contrast, every simulated flight with the final controller was stabilized, and the maximum γ-value was 0.75 (See Fig. 4.11). Since the initial controller repeatedly failed in simulation, we did not implement it during physical flight tests. However, the final controller successfully completed each flight, and Fig. 4.12 shows that the maximum γ-value came to be 1.64. Here we reach the observation that the simulation environment provides optimistic predictions on performance compared to that experienced from flight tests. This reflects the common understanding that simulation environments oftentimes predict fairer results than reality

prefers to bear. Alternatively, the robust performance from IQC analysis pertaining to the final controller is greater than that seen in flight tests.

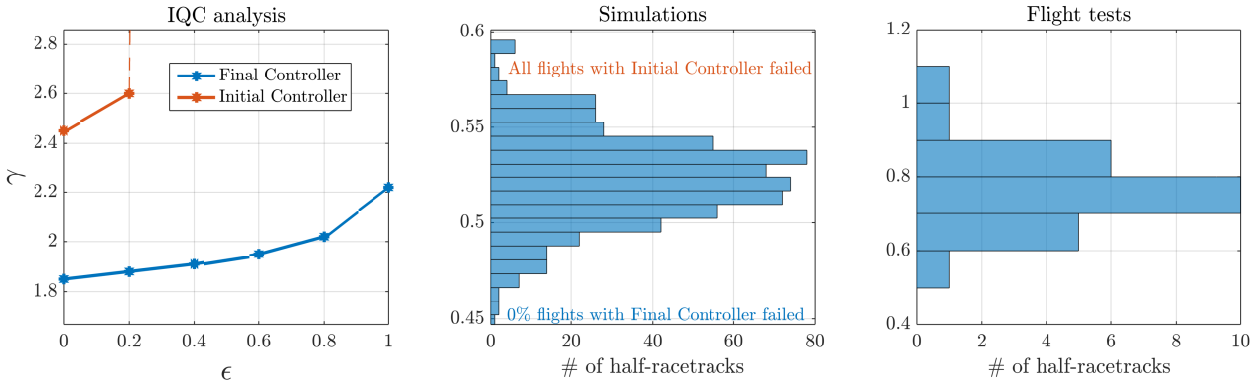

Figure 4.13: $\mathcal{D}$-to-ℓ_2 induced gains from IQC analysis, simulations, and flight tests with PF$\mathcal{H}_2$ controllers

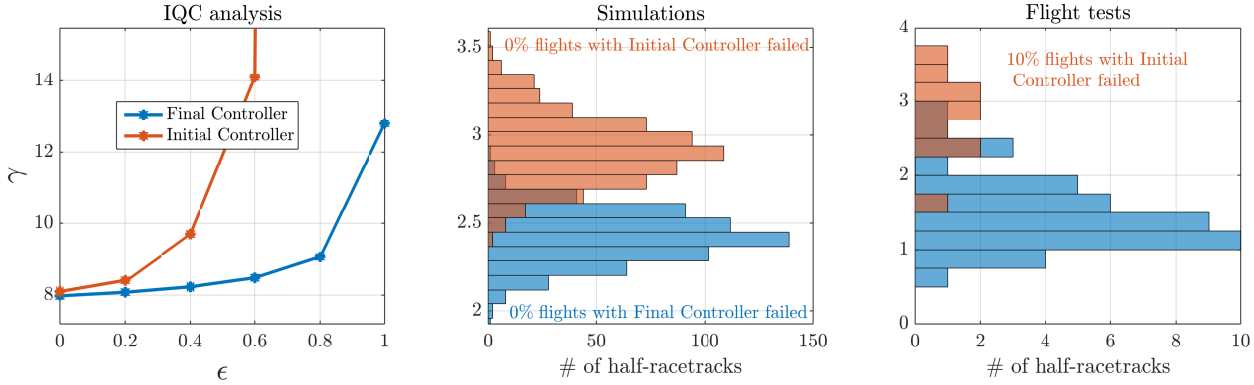

Figure 4.14: $\mathcal{D}$-to-ℓ_2 induced gains from IQC analysis, simulations, and flight tests with PFpid controllers

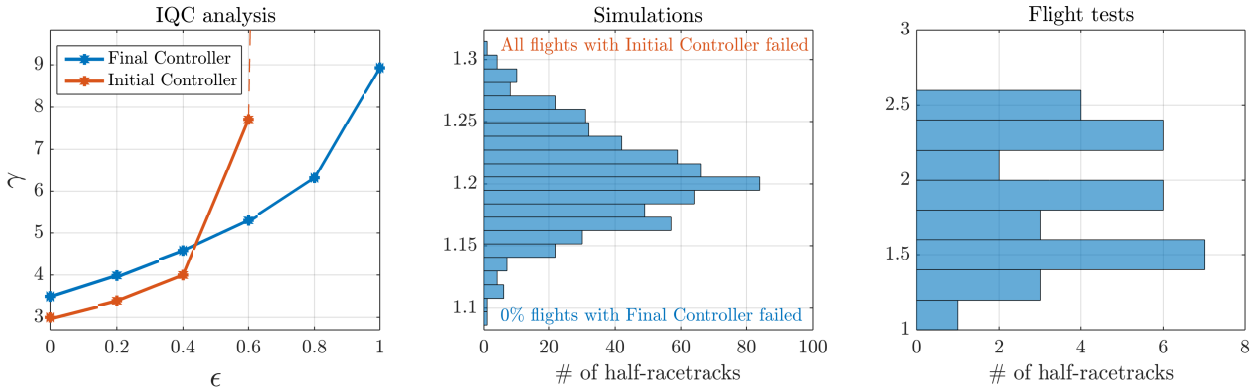

Figure 4.15: $\mathcal{D}$-to-ℓ_2 induced gains from IQC analysis, simulations, and flight tests with TT$\mathcal{H}_2$ controllers

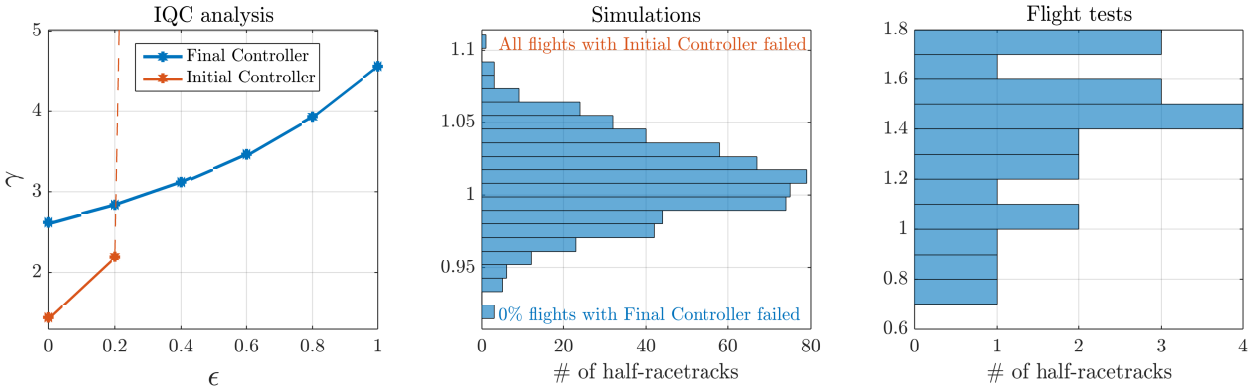

Figure 4.16: $\mathcal{D}$-to-ℓ_2 induced gains from IQC analysis, simulations, and flight tests with TT$\mathcal{H}_\infty$ controllers

Similar observations may be made for the PF$\mathcal{H}_2$, PFpid, TT$\mathcal{H}_2$, and TT$\mathcal{H}_\infty$ controllers. Figs. 4.13, 4.14, 4.15, and 4.16, respectively, display the IQC analysis, simulations, and flight test results for each controller. As previously noted, the IQC analysis, simulations, and flight tests for the PFpid controller assume $|k_1| \leq 0.0035$, resulting in a larger track.

4.5.3 Observations from IQC analysis, simulations, and flight tests

Predicting failures via IQCs

From Table 4.5, we see that if IQC analysis cannot obtain a robust performance level, then simulations nearly always exhibit loss of control. Since the uncertain simulation environment is oftentimes over-optimistic, we can reasonably conclude that controllers which fail in simulation will fail in flight tests. This demonstrates that IQC analysis can be used to indicate loss of control. This point is further confirmed by inspecting the PFpid controller's performance in Fig. 4.14. Interestingly, IQC analysis predicts the initial PFpid controller will fail, while simulations do not give such an indication. Flight tests proved contrary to the prediction from the simulation environment; the initial controller oftentimes exhibited

Table 4.5: Comparison of measures on UAS performance, with performance output $e = [\bar{X}_E, \bar{Y}_E, \bar{z}_E]^T$ and disturbance input $d = [u_c, v_c, u_t, v_t, w_t, \eta^T]^T$

Type	Init/ Final	$\|\hat{M}_{22}\|_2$	$\|\hat{M}_{22}\|_\infty$	γ_{sim}	$\gamma_{\text{IQC}}^{\text{nom}}$ $(\epsilon = 0)$	γ_{IQC} $(\epsilon = 1)$	γ_{flt}
PF$\mathcal{H}_2$	Init	0.488	8.69	∞	2.45	∞	–
	Final	0.505	6.60	0.60	1.85	2.22	1.01
PF$\mathcal{H}_\infty$	Init	0.425	5.45	∞	1.52	∞	–
	Final	0.531	9.11	0.75	2.56	2.82	1.64
TT$\mathcal{H}_\infty$	Init	0.87	5.09	∞	1.45	∞	–
	Final	0.81	10.3	1.10	2.62	4.56	1.78
TT$\mathcal{H}_2$	Init	0.797	11.7	∞	3.0	∞	–
	Final	0.875	13.8	1.31	3.50	8.93	2.57
PFpid	Init	1.41	28.6	3.58	8.10	∞	∞
	Final	1.39	28.3	2.87	7.98	12.8	2.95

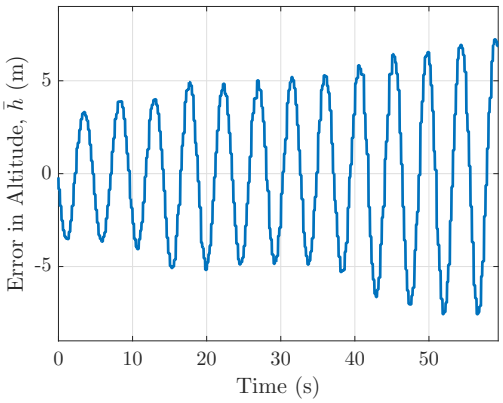

Figure 4.17: Vertical oscillations induced by initial PFpid controller

drastic vertical oscillations, with approximately 10% of the flight segments leading to aggressive dives (see Fig. 4.17). This case study provides the compelling conclusion that IQC analysis is capable of predicting failures for certain controllers when an uncertain simulation environment does not.

Comparing controllers via IQCs

There are many measures to assess a controller's performance. These results indicate that applying IQC analysis on the uncertain UAS framework is a valid tool in making depend-

able comparisons. To illustrate this point, Table 4.5 displays a variety of measures of the UAS performance: the robust $\mathcal{D}$-to-ℓ_2-gain performance level, the nominal $\mathcal{D}$-to-ℓ_2-gain performance level, the nominal system's $\mathcal{H}_\infty$ norm, the nominal system's $\mathcal{H}_2$ norm, and the worst-case performance levels observed from the uncertain simulation environment. Among all of these, the uncertain simulation environment and the uncertain system's robust performance consistently predict the ranking for each controller's worst-case performance level observed during flight.

Notably, the remaining metrics do not bear comparisons consistent with physical flight for numerous controllers. This outcome is probably because these metrics are for nominal system analysis, which does not truly reflect the degradation in performance during physical flight. This observation supports the notion that treating uncertainties in analysis leads to a more realistic picture.

Using signal IQCs in analysis

Since Theorem 2.1 provides only a sufficient condition for finding the robust performance, IQC analysis is inherently conservative. However, if applicable, signal IQCs are capable of significantly reducing the resulting γ-values. By inspecting Table 4.5, there are many controllers where the *nominal* system's $\mathcal{H}_\infty$ norm is greater than the *uncertain* system's robust performance. This observation follows from the fact that IQC analysis is constraining the allowable disturbances to lie in $\mathcal{D}$.

Beyond reducing conservatism, signal IQCs give a better characterization of the system's performance. This finding is further demonstrated by inspecting the γ-values pertaining to the PF$\mathcal{H}_2$ and PF$\mathcal{H}_\infty$ controllers. To reduce computational complexity, the tuning routine did not characterize the wind disturbance channels with signal IQCs; each wind channel

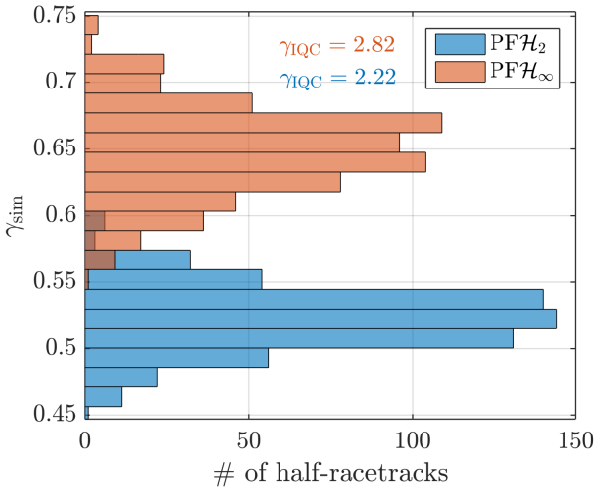

Figure 4.18: $\mathcal{D}$-to-ℓ_2 induced gains from IQC analysis and simulations with wind appropriately constrained

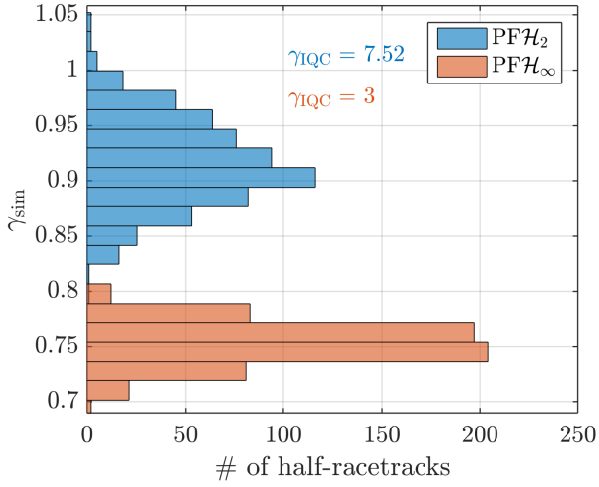

Figure 4.19: $\mathcal{D}$-to-ℓ_2 induced gains from IQC analysis and simulations where wind is any ℓ_2 signal

could be any ℓ_2 signal. The γ-values from the tuning routine in Table 4.3 report that the PF$\mathcal{H}_2$ controller yields significantly worse performance than the PF$\mathcal{H}_\infty$ controller, with respective robust performance levels of 7.52 and 3.0. Conversely, by characterizing wind disturbances with appropriate signal IQCs, the IQC analysis results in Section 4.5.2 reflect what is observed in simulations and flight tests; the PF$\mathcal{H}_2$ controller has better performance than the PF$\mathcal{H}_\infty$ controller, with respective performance levels of 2.22 and 2.82. Interestingly, when simulating both controlled systems with wind disturbances that are not composed of steady wind and Dryden turbulence, the PF$\mathcal{H}_\infty$ controller has better performance than the PF$\mathcal{H}_2$ controller, as suggested by the γ-values from IQC analysis when wind disturbances are not properly constrained (see Figs. 4.18 and 4.19).

Qualitative comparison of controller types

By comparing the performance of trajectory-tracking controllers with their counterpart path-following controllers, it is immediately apparent that the path-following scheme pro-

vides better performance. Nearly all the measures given in Table 4.5 also predict the same phenomenon; path following has reduced position tracking error. An obvious reason is that path-following UAS, by construction, oftentimes have zero error in X_E. This point aside, the tested trajectory-tracking controllers were much more aggressive in flight and had greater vertical oscillations than the path-following controllers (see flight videos at `http://www.dept.aoe.vt.edu/~farhood/ctrFlight.html`). Even though trajectory tracking had poorer performance and handling, this control approach should not be entirely rejected; many times it is essential that an aircraft follows a plan with explicit timing constraints, such as in dynamic obstacle avoidance applications. In these cases, performance may need to be sacrificed to have timeliness addressed in the control effort.

In comparing between the $\mathcal{H}_2$, $\mathcal{H}_\infty$, and PID controllers, the outstanding observation is that PID control bore considerably worse performance than the remaining controllers. Though trajectory-tracking controllers typically have worse performance than path-following controllers, the path-following PID controller did not perform as well as either trajectory-tracking controllers. This was in addition to the PID controller conducting less aggressive turns at 285 m radius rather than 200 m. These performance characteristics were especially reflected in IQC analysis, where the tuning routine also struggled to tune the controller as proficiently as the other controllers.

The $\mathcal{H}_2$ and $\mathcal{H}_\infty$ controllers had mixed results. The TT$\mathcal{H}_\infty$ controller has better robust performance than the TT$\mathcal{H}_2$ controller, and the PF$\mathcal{H}_2$ controller has improved robust performance over the PF$\mathcal{H}_\infty$ controller. The latter observation illustrates the benefit of using IQC analysis to tune different controllers. Though $\mathcal{H}_2$ controllers do not have system-independent robustness guarantees [89], tuning with IQC analysis helps find appropriate controller parameters that yield adequate robustness given the prespecified uncertain plant.

To be clear, the previous discussion points are specific to the five initial and five final

controllers studied in this chapter. Though we hope many of these observations (such as the consistency and reliability of this framework) extend beyond the controllers we have studied, this work can only make such conclusions for the cases at hand. However, our objective in applying this framework to a wide variety of controllers is to determine its validity across multiple test cases, which has been met with encouraging results.

Chapter 5

Robustness analysis for time-varying systems with time-varying IQC multipliers

This chapter presents novel IQC-based robustness analysis theorems. Whereas the IQC theorem given in [11] makes the assumption that both the nominal system G and the IQC multiplier Π are time-invariant, the main result of this chapter demonstrates that either may be time-varying and that G may have a non-zero initial condition. Furthermore, if both are eventually-periodic, then robustness analysis may be conducted by solving a finite dimensional SDP. In Section 5.1 we develop the necessary operator theoretic machinery. Section 5.2 presents the IQC-based robustness analysis theorems. We detail a number of time-varying IQC multipliers in Section 5.3. Section 5.4 demonstrates the utility of these results by applying them to two examples: a UAS flying a Split-S maneuver and an inverted pendulum. The papers on which this chapter is based are [38, 49, 50, 52].

5.1 Operators of interest

To properly approach the results of this chapter, we first define the operators used herein. These definitions are adapted from [48, 90]. Given a sequence of matrices $A = (A(k))_{k\in 0_+}$, $A(k) \in \mathbb{R}^{n\times n}$, we define the *memoryless* operator $A : \ell_2 \to \ell_2$ by the operation $y = Ax$, where

$y(k) = A(k)x(k)$ for all $k \in 0_+$. The slight abuse of notation from using A for a sequence of matrices and a memoryless operator can easily be resolved by context. The operation $y = Ax$ is expressed by the infinite dimensional matrix (IDM) representation as

$$\begin{bmatrix} y(0) \\ y(1) \\ y(2) \\ \vdots \end{bmatrix} = \begin{bmatrix} A(0) & & & & \\ & A(1) & & & \\ & & A(2) & & \\ & & & \ddots & \end{bmatrix} \begin{bmatrix} x(0) \\ x(1) \\ x(2) \\ \vdots \end{bmatrix}$$

A blank entry in the IDM representation corresponds to a zero matrix. A is a bounded operator on ℓ_2 if and only if $\sup_k \|A(k)\| < \infty$. In the following, any given memoryless operator is assumed to be bounded. The operator $F = \begin{bmatrix} A & B \\ C & D \end{bmatrix} : \ell_2^n \times \ell_2^m \to \ell_2^n \times \ell_2^p$ is a *partitioned memoryless* operator if A, B, C, D are memoryless operators. We use the notation

$$\left[\!\!\left[\begin{array}{cc} A & B \\ C & D \end{array} \right]\!\!\right] = \operatorname{diag}\left(\begin{bmatrix} A(0) & B(0) \\ C(0) & D(0) \end{bmatrix}, \begin{bmatrix} A(1) & B(1) \\ C(1) & D(1) \end{bmatrix}, \ldots \right) \tag{5.1}$$

to express the *memoryless realization* of F, which maps $\ell_2^{(n+m)}$ to $\ell_2^{(n+p)}$. It can be shown that the mapping $[\![\cdot]\!]$ is an isometric homomorphism from the space of partitioned memoryless operators to memoryless operators [90].

We also introduce the delay operator $Z : \ell_2 \to \ell_2$, defined as $Zv = Z(v(0), v(1), \ldots) = (0, v(0), v(1), \ldots)$. Its IDM representation is

$$Z = \begin{bmatrix} 0 & & \\ I & 0 & \\ & I & \ddots \\ & & \ddots \end{bmatrix}.$$

When the Hilbert space of interest is $\prod_{i=1}^{r}\ell_2$, the operator $\tilde{Z}:\prod_{i=1}^{r}\ell_2\to\prod_{i=1}^{r}\ell_2$ is defined as $\tilde{Z}\{\!\{u_1,\ldots,u_r\}\!\}=\{\!\{Zu_1,\ldots,Zu_r\}\!\}$. For simplicity, the sequel abuses notation slightly by using the symbol Z to represent either the operator on ℓ_2 or the operator on $\prod_{i=1}^{r}\ell_2$. This same abuse of notation is applied with the symbols $\mathbb{P}_N^+$ and $\mathbb{P}_N^-$. With these definitions, consider the difference equations

$$x^+(k+1)=A(k)x^+(k)+B(k)u(k) \tag{5.2a}$$

$$y^+(k)=C(k)x^+(k)+D(k)u(k) \tag{5.2b}$$

$$x^-(k)=A(k)x^-(k+1)+B(k)u(k) \tag{5.3a}$$

$$y^-(k)=C(k)x^-(k+1)+D(k)u(k). \tag{5.3b}$$

Assuming $x(0)=0$, equations (5.2a)-(5.2b) may be written in operator form as

$$x^+=ZAx^++ZBu \tag{5.4a}$$

$$y^+=Cx^++Du. \tag{5.4b}$$

Equations (5.3a)-(5.3b) also have an operator expression, which is

$$x^-=AZ^*x^-+Bu \tag{5.5a}$$

$$y^-=CZ^*x^-+Du. \tag{5.5b}$$

Assuming that $(I-ZA)^{-1}$ is well-defined on ℓ_2, we define the operator $G^+:=C(I-ZA)^{-1}ZB+D$ and note that $y^+=G^+u$. G^+ has the following IDM representation:

$$G^+=\begin{bmatrix} D(0) & & & \\ C(1)B(0) & D(1) & & \\ C(2)A(1)B(0) & C(2)B(1) & D(2) & \\ \vdots & \vdots & \vdots & \ddots \end{bmatrix}. \tag{5.6}$$

In like manner, assuming $(I - AZ^*)^{-1}$ is well-defined on ℓ_2, we see that $y^- = G^- u$, where $G^- := CZ^*(I - AZ^*)^{-1}B + D$. The IDM representation for G^- is

$$G^- = \begin{bmatrix} D(0) & C(0)B(1) & C(0)A(1)B(2) & \cdots \\ & D(1) & C(1)B(2) & \cdots \\ & & D(2) & \cdots \\ & & & \ddots \end{bmatrix}. \tag{5.7}$$

It is clear that the IDM representation of G^+ is lower-triangular, which corresponds to the operator being causal. In like manner, the IDM representation of G^- is upper-triangular, indicating that the operator is anticausal. For G^+ and G^- to be well-defined and bounded, we must have $(I - ZA)^{-1}$ and $(I - AZ^*)^{-1}$ well-defined and bounded, respectively.

Definition 5.1. The memoryless operator A is *causally stable* if there exist positive scalars μ, ν, and ρ and a memoryless operator $P = P^*$ such that $\rho I \preceq P \preceq \mu I$ and

$$A^* Z^* P Z A - P \preceq -\nu I. \tag{5.8}$$

A is *anticausally stable* if there exist positive scalars μ, ν, and ρ and a memoryless operator $P = P^*$ such that $\rho I \preceq P \preceq \mu I$ and

$$A^* P A - Z^* P Z \preceq -\nu I. \tag{5.9}$$

If A is a partitioned memoryless operator, then it may be causally stable and/or anticausally stable if there exists a partitioned memoryless operator $P = P^*$ satisfying the pertinent aforementioned conditions.

Proposition 5.2. *Given a possibly partitioned memoryless operator A, the operator $(I - ZA)^{-1}$ ($(I - AZ^*)^{-1}$) is well-defined and bounded on ℓ_2 if and only if A is causally stable (anticausally stable).*

Proof. This is a standard result (see [48]). □

Proposition 5.2 gives conditions for asserting if G^+ or G^- is a bounded operator on ℓ_2. We now introduce the notion of nodes, a class of operators to which G^+ and G^- belong.

Definition 5.3. A quadruple of memoryless operators (A, B, C, D) define a

- *causal node* $G^+ = D + C(I - ZA)^{-1}ZB$ if A is causally stable,
- *anticausal node* $G^- = D + CZ^*(I - AZ^*)^{-1}B$ if A is anticausally stable.

The denotation $[A, B, C, D]_+$ ($[A, B, C, D]_-$) indicates a causal node (anticausal node). An octuple of memoryless operators (A, B, C, D, E, U, V, W), where A is causally stable and E is anticausally stable, define a

- *dichotomic node* $G^d = [A, B, C, D]_+ + [E, U, V, W]_-$.

We use $[A, B, C, D, E, U, V, W]$ to denote a dichotomic node.

Remark 5.4. A causal node (anticausal node) is a dichotomic node with $[A, B, C, D]_+ = [A, B, C, D, 0, 0, 0, 0]$ ($[A, B, C, D]_- = [0, 0, 0, 0, A, B, C, D]$).

Remark 5.5. If the operators A, B, C, D are conformably partitioned memoryless operators, then a *partitioned causal/anticausal/dichotomic node* is defined by analogous operator equations.

It can be shown that the adjoint of a causal node is an anticausal node and vice versa. Also, all three types of nodes are bounded operators on ℓ_2. If these nodes were defined for the bi-infinite signal space (i.e. $\ell_2(\mathbb{Z})$), the space of dichotomic nodes would be considered a time-varying analog to $\mathcal{RL}_\infty$, while the space of causal (anticausal) nodes would be analogous

to $\mathcal{RH}_\infty$ ($\mathcal{RH}_\infty^\perp$). The notion of dichotomicity introduced here differs from that in [48] in that we classify *nodes* as dichotomic. This approach allows us to analyze a broader class of operators on ℓ_2.

For example, consider the transfer function

$$\hat{L}(z) = 1/z + z. \tag{5.10}$$

This LTI system can be expressed as the dichotomic node $L = [0, I, I, 0, 0, I, I, 0]$. Though (5.10) has a simple operator expression given the previous definitions, the definition of dichotomicity discussed in [48] (which we are not pursuing) cannot be applied to such an operator.

This work is also concerned with LTV systems having non-zero initial conditions.

Definition 5.6. Given a node $G = [A, B, C, D]_+$ and $N \in 0_+$, we define the *zero-input* operator $\mathcal{S}_N^G : \mathbb{R}^n \to \ell_2^n(N_+)$ as

$$(\mathcal{S}_N^G \xi)(k) = \Phi_A(k, N)\xi \text{ for } k \geq N \tag{5.11}$$

$$\text{where } \Phi_A(k, N) = \begin{cases} I, & k = N \\ A(k-1)A(k-2)\dots A(N), & k > N. \end{cases}$$

Definition 5.7. The causal node $G = [A, B, C, D]_+$ defines an *IC node* $G^{ic} : \ell_2^m \times \mathbb{R}^n \to \ell_2^p$, by the equation

$$G^{ic}\{\!\{u, \xi\}\!\} = Gu + C\mathcal{S}_0^G \xi. \tag{5.12}$$

A *partitioned IC node* is defined analogously by a partitioned causal node. The expression $[A, B, C, D]_+^{ic}$ is used to denote a (possibly partitioned) IC node. If $G = [A, B, C, D]_+$, then $[A, B, C, D]_+^{ic} = \begin{bmatrix} G & G_\xi \end{bmatrix}$, where $G_\xi = C\mathcal{S}_0^G$.

In IQC analysis, asserting the robust performance of an uncertain system $(G, \mathbf{\Delta})$ revolves around a self-adjoint multiplier Π, which serves as a functional separator between the graph of G and the inverse graph Δ. When G is an LTI system, Π is assumed to be LTI as well. Recent work in [38] demonstrates that IQC analysis can be extended to systems where G is LTV. This raises the natural question on whether Π can also be LTV for IQC analysis. The following affirms that Π may be considered as LTV, as far as it satisfies relatively general conditions on its signature. To proceed, we must discuss factorizations of self-adjoint dichotomic nodes.

Lemma 5.8. *Any self-adjoint dichotomic node* Π *can be factorized as* $\Pi = \Psi^* S \Psi$*, where* Ψ *is a partitioned causal node, and* $S = S^*$ *is a partitioned memoryless operator.*

Proof. As Π is dichotomic, there exist operators A, B, C, D, E, U, V, W such that $\Pi = \bar{\Psi}^+ + \bar{\Psi}^-$, where $\bar{\Psi}^+ = [A, B, C, D]_+$ and $\bar{\Psi}^- = [E, U, V, W]_-$. Furthermore, $\bar{\Psi}^+ + \bar{\Psi}^- = (\bar{\Psi}^+)^* + (\bar{\Psi}^-)^*$. Subtracting $\bar{\Psi}^-$ and $(\bar{\Psi}^-)^*$ from both sides produces $\bar{\Psi}^+ - (\bar{\Psi}^-)^* = (\bar{\Psi}^+)^* - \bar{\Psi}^-$. As the left-hand side of the last equation is a causal node and the right-hand side is an anticausal node, both sides are equal to a self-adjoint memoryless operator, say, T. Hence, $\bar{\Psi}^- = (\bar{\Psi}^+)^* - T$. Therefore, $\Pi = \bar{\Psi}^+ + (\bar{\Psi}^+)^* - T$. The right-hand side of the last equation is restated as $\Psi^* S \Psi$, where

$$\Psi = \begin{bmatrix} (I - ZA)^{-1} ZB \\ I \end{bmatrix}, \quad S = \begin{bmatrix} 0 & C^* \\ C & D + D^* - T \end{bmatrix}.$$

It can easily be seen that both blocks in Ψ are causal nodes, while all four blocks of S are memoryless operators. □

Remark 5.9. Following a similar proof, the conclusions of Lemma 5.8 hold for a self-adjoint partitioned dichotomic node.

For notational ease, if Π is a dichotomic node, the *factors* (Ψ, S) of Π denote the (possibly partitioned) causal node Ψ and memoryless operator $S = S^*$ such that $\Pi = \Psi^* S \Psi$. It turns out that the factorization for Π in Lemma 5.8 is not unique; there are many different pairs (Ψ, S) such that $\Psi^* S \Psi = \Pi$. We are interested in finding a special factorization $(\bar{\Psi}, \bar{S})$ for Π that is useful in IQC analysis.

Definition 5.10. The (possibly partitioned) causal node $\Psi = [A, B, C, D]_+$ and memoryless operator $S = S^*$, time-index $N \geq 0$, initial condition $\xi \in \mathbb{R}^n$, and input $u \in \ell_2(N_+)$ define the *Popov index*,

$$J^{\Psi,S}(N, \xi, u) := \left\langle \begin{bmatrix} x \\ u \end{bmatrix}, \begin{bmatrix} {}^N Q & {}^N L \\ ({}^N L)^* & {}^N R \end{bmatrix} \begin{bmatrix} x \\ u \end{bmatrix} \right\rangle, \text{ subject to:}$$

$$x(k+1) = A(k)x(k) + B(k)u(k) \ \forall k \in N_+, \ x(N) = \xi, \ x \in \ell_2(N_+) \tag{5.13}$$

$$\text{where } \ Q := C^* S C, \ L := C^* S D, \ R := D^* S D. \tag{5.14}$$

Additionally, given time-index $T \geq N$, define the *truncated Popov index*

$$J_T^{\Psi,S}(N, \xi, u) := \left\langle \begin{bmatrix} x \\ u \end{bmatrix}, \begin{bmatrix} {}_T^N Q & {}_T^N L \\ ({}_T^N L)^* & {}_T^N R \end{bmatrix} \begin{bmatrix} x \\ u \end{bmatrix} \right\rangle, \text{ subject to (5.13).}$$

Furthermore, when Π is partitioned and has 2 inputs and outputs, the *lower Popov index* is

$$\underline{J}^{\Psi,S}(N, \xi) = \sup_{\vartheta \in \ell_2(N_+)} \inf_{\varphi \in \ell_2(N_+)} J^{\Psi,S}\left(N, \xi, \{\!\!\{ \varphi, \vartheta \}\!\!\}\right)$$

and the *upper Popov index* is

$$\bar{J}^{\Psi,S}(N, \xi) = \inf_{\varphi \in \ell_2(N_+)} \sup_{\vartheta \in \ell_2(N_+)} J^{\Psi,S}\left(N, \xi, \{\!\!\{ \varphi, \vartheta \}\!\!\}\right).$$

The equation (5.13) is not written in operator form, as the evolution depends on the initial

condition ξ. However, the solution $x \in \ell_2(N_+)$ of (5.13) also satisfies

$$\mathbb{P}_N^+ Z^* x = Ax + Bu. \tag{5.15}$$

For context, given a dichotomic node Π with factors (Ψ, S), we have

$$J^{\Psi,S}(N, 0, u) = \langle u, \Psi^* S \Psi u \rangle = \langle u, \Pi u \rangle \text{ for all } u \in \ell_2(N_+).$$

Because causal nodes enforce the initial condition $x(N) = \xi = 0$, in general the previous inner products do not equal the Popov index if $\xi \neq 0$. Indeed, given the same N, u, and $\xi \neq 0$, the Popov indices pertaining to two different factors of Π are generally different. If $\xi = 0$, then the two Popov indices are necessarily equal.

Given $\Psi = [A, B, C, D]_+$, we define the *zero-state operator* $\mathcal{L}_N^\Psi : \ell_2^m(N_+) \to \ell_2^n(N_+)$ as

$$\mathcal{L}_N^\Psi = [A, B, I, 0]_+ \mathbb{P}_{\mathbb{N}}^+. \tag{5.16}$$

The solution of the equation (5.13) can be expressed by the operator $\Upsilon_N^\Psi : \mathbb{R}^n \times \ell_2^m(N_+) \to \ell_2^n(N_+)$, where $\Upsilon_N^\Psi(\xi, u) = \mathcal{S}_N^\Psi \xi + \mathcal{L}_N^\Psi u$. We can now formulate the Popov index as

$$\begin{aligned}
J^{\Psi,S}(N, \xi, u) &= \left\langle \begin{bmatrix} \Upsilon_N^\Psi(\xi, u) \\ u \end{bmatrix}, \begin{bmatrix} {}^N Q & {}^N L \\ ({}^N L)^* & {}^N R \end{bmatrix} \begin{bmatrix} \Upsilon_N^\Psi(\xi, u) \\ u \end{bmatrix} \right\rangle \\
&= \left\langle \begin{bmatrix} \xi \\ u \end{bmatrix}, \begin{bmatrix} (\mathcal{S}_N^\Psi)^* & 0 \\ (\mathcal{L}_N^\Psi)^* & I \end{bmatrix} \begin{bmatrix} {}^N Q & {}^N L \\ ({}^N L)^* & {}^N R \end{bmatrix} \begin{bmatrix} \mathcal{S}_N^\Psi & \mathcal{L}_N^\Psi \\ 0 & I \end{bmatrix} \begin{bmatrix} \xi \\ u \end{bmatrix} \right\rangle \\
&= \left\langle \begin{bmatrix} \xi \\ u \end{bmatrix}, \begin{bmatrix} \mathcal{X}_N^{\Psi,S} & \mathcal{P}_N^{\Psi,S} \\ (\mathcal{P}_N^{\Psi,S})^* & \mathcal{R}_N^{\Psi,S} \end{bmatrix} \begin{bmatrix} \xi \\ u \end{bmatrix} \right\rangle, \text{ where} \\
\mathcal{X}_N^{\Psi,S} &:= (\mathcal{S}_N^\Psi)^* {}^N Q \mathcal{S}_N^\Psi, \quad \mathcal{P}_N^{\Psi,S} := (\mathcal{S}_N^\Psi)^* ({}^N Q \mathcal{L}_N^\Psi + {}^N L), \text{ and} \\
\mathcal{R}_N^{\Psi,S} &:= {}^N R + {}^N L^* \mathcal{L}_N^\Psi + (\mathcal{L}_N^\Psi)^* {}^N L + (\mathcal{L}_N^\Psi)^* {}^N Q \mathcal{L}_N^\Psi.
\end{aligned} \tag{5.17}$$

It can be shown by the definitions that if Π has factors (Ψ, S), then $\mathcal{R}_N^{\Psi,S} =^N \Pi$.

Definition 5.11. The possibly partitioned causal node $\Psi = [A, B, C, D]_+$ and the possibly partitioned memoryless operator $S = S^*$ define the *Discrete Difference Riccati Equation* $(DDRE(\Psi, S))$

$$X = A^*Z^*XZA + Q - (A^*Z^*XZB + L)(R + B^*Z^*XZB)^{-1}(L^* + B^*Z^*XZA) \tag{5.18}$$

where Q, R, and L are defined in (5.14), $X = X^*$ is a bounded memoryless operator, and $(R + B^*Z^*XZB)^{-1}$ is well-defined and bounded. Given a *feedback operator* $F := -(R + B^*Z^*XZB)^{-1}(L^* + B^*Z^*XZA)$, the solution X to (5.18) is said to be a *stabilizing solution* if $A + BF$ is causally stable.

It is well-known that the stabilizing solution X is unique [48]. For context, the $DDRE(\Psi, S)$ can be equivalently expressed with the sequence of equations

$$\begin{aligned} X(k) = A(k)^T X(k{+}1)A(k){+}Q(k){-}\big(A(k)^T X(k{+}1)B(k){+}L(k)\big) \\ \times \big(R(k) + B(k)^T X(k{+}1)B(k)\big)^{-1}\big(L(k)^T + B(k)^T X(k{+}1)A(k)\big) \end{aligned}$$

which, when the given operators are time-invariant, recover the Discrete Riccati Equation

$$X = A^T XA{+}Q{-}(A^T XB{+}L)(R + B^T XB)^{-1}(L^T + B^T XA).$$

5.2 Integral quadratic constraints

Our application of integral quadratic constraint theory addresses the uncertain system $(G^{ic}, \mathbf{\Delta})$ in Fig. 5.1, where

$$G^{ic} = \left[A^G, \begin{bmatrix} B^{G1} & B^{G2} \end{bmatrix}, \begin{bmatrix} C^{G1} \\ C^{G2} \end{bmatrix}, \begin{bmatrix} D^{G11} & D^{G12} \\ D^{G21} & D^{G22} \end{bmatrix} \right]_+^{ic} \tag{5.19a}$$

$$= \begin{bmatrix} G_{11} & G_{12} & G_{1\xi} \\ G_{21} & G_{22} & G_{2\xi} \end{bmatrix} \tag{5.19b}$$

is a partitioned IC node, $A^G(k) \in \mathbb{R}^{n_G \times n_G}$, $\Delta \in \mathbf{\Delta}$, $\mathbf{\Delta}$ is a set of causal operators on ℓ_{2e} bounded on ℓ_2 , and the interconnection equations are

$$\begin{bmatrix} \varphi \\ e \end{bmatrix} = \begin{bmatrix} G_{11} & G_{12} & G_{1\xi} \\ G_{21} & G_{22} & G_{2\xi} \end{bmatrix} \begin{bmatrix} \vartheta \\ d \\ \xi^G \end{bmatrix}, \quad \vartheta = \Delta(\varphi). \tag{5.20}$$

For the remainder of this chapter, we make an additional assumption on $\mathbf{\Delta}$ in that there exists a scalar μ such that $\sup_{\Delta \in \mathbf{\Delta}} \|\Delta\|_{\ell_2 \to \ell_2} \leq \mu$. This is not an overly restrictive assumption, since most uncertainty sets described by IQC multipliers in the literature already satisfy this condition [11, 20]. Furthermore, the sets that do not satisfy such a condition may be closely approximated by the subset $\tilde{\mathbf{\Delta}} = \{\Delta \in \mathbf{\Delta} \mid \|\Delta\|_{\ell_2 \to \ell_2} \leq \mu\}$ where μ may be arbitrarily large. For example, no such μ exists for passive nonlinearities, but this set is well-approximated by defining μ to be arbitrarily large and considering only passive nonlinearities whose ℓ_2-induced norm is bounded by μ.

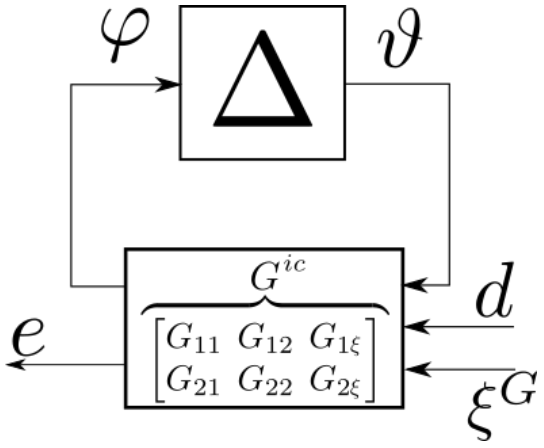

Figure 5.1: The interconnection (G^{ic}, Δ)

Definition 5.12. $(G^{ic}, \mathbf{\Delta})$ defined in (5.20) is *robustly well-posed* if $(I - G_{11}\Delta)$ has a causal inverse on ℓ_{2e} for all $\Delta \in \mathbf{\Delta}$.

The previous definition signifies that, for every $d \in \ell_{2e}$, $\xi^G \in \mathbb{R}^{n_G}$, $\Delta \in \mathbf{\Delta}$, there exist unique signals $\varphi,\ \vartheta,\ e \in \ell_{2e}$ which depend causally on $\{\!\!\{ d, G_{1\xi}\xi, G_{2\xi}\xi \}\!\!\}$ and satisfy (5.20).

Definition 5.13. $(G^{ic}, \mathbf{\Delta})$ defined in (5.20) is *robustly stable* if it is robustly well-posed and $(I - G_{11}\Delta)^{-1}$ is bounded on ℓ_2 for all $\Delta \in \mathbf{\Delta}$.

Similar to Definition 5.12, $(G^{ic}, \mathbf{\Delta})$ being robustly stable signifies that there exist constants $c_{\vartheta d}$, $c_{\vartheta\xi}$, $c_{\varphi d}$, $c_{\varphi\xi}$, c_{ed}, and $c_{e\xi}$ such that, for all $\Delta \in \mathbf{\Delta}$, $d \in \ell_2$, $\xi^G \in \mathbb{R}^{n_G}$,

$$\begin{aligned} \|\vartheta\| &\le c_{\vartheta d}\|d\| + c_{\vartheta\xi}\|\xi^G\| \\ \|\varphi\| &\le c_{\varphi d}\|d\| + c_{\varphi\xi}\|\xi^G\| \\ \|e\| &\le c_{ed}\|d\| + c_{e\xi}\|\xi^G\|. \end{aligned}$$

Many times well-posedness and stability are defined by considering Fig. 5.2 and the equations

$$v = G_{11}w + f \qquad\qquad w = \Delta(v) + q. \tag{5.21}$$

Well-posedness of (5.21) is then asserted if, for every $f, q \in \ell_{2e}$, there exist unique signals $v, w \in \ell_{2e}$ satisfying (5.21) and causally depending on f and q. Similarly, stability is asserted if the system (5.21) is well-posed and the mapping $\{\!\!\{ f, q \}\!\!\} \mapsto \{\!\!\{ v, w \}\!\!\}$ is bounded on ℓ_2. With non-zero initial conditions, we modify (5.21) to be

$$v = G_{11}w + f + G_{1\xi}\underline{\xi}^G \qquad\qquad w = \Delta(v) + q. \tag{5.22}$$

With this alteration, well-posedness of (5.22) is asserted if, for every $f, q \in \ell_{2e}$ and $\underline{\xi}^G \in \mathbb{R}^{n_G}$,

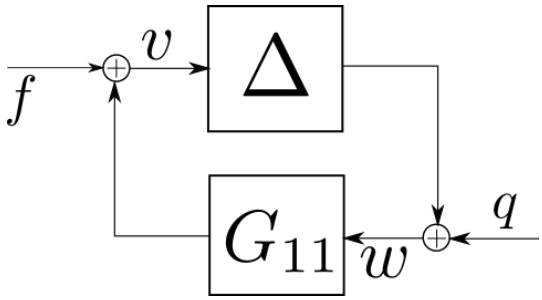

Figure 5.2: System described by (5.21)

there exist unique signals $v, w \in \ell_{2e}$ satisfying (5.22) and causally depending on f, q, and $G_{1\xi}\underline{\xi}^G$. Stability is asserted if (5.22) is well-posed and the mapping $\{\!\{f, q, \underline{\xi}\}\!\} \mapsto \{\!\{v, w\}\!\}$ is bounded. We can make either of these assertions by defining $\underline{d} = \{\!\{f, q\}\!\}$, $\underline{e} = \{\!\{v, w\}\!\}$, the operators

$$\underline{G}^{ic} = \begin{bmatrix} G_{11} & \begin{bmatrix} I & G_{11} \end{bmatrix} & G_{1\xi} \\ \begin{bmatrix} G_{11} \\ I \end{bmatrix} & \begin{bmatrix} I & G_{11} \\ 0 & I \end{bmatrix} & \begin{bmatrix} G_{1\xi} \\ 0 \end{bmatrix} \end{bmatrix} = \begin{bmatrix} \underline{G}_{11} & \underline{G}_{12} & \underline{G}_{1\xi} \\ \underline{G}_{21} & \underline{G}_{22} & \underline{G}_{2\xi} \end{bmatrix} \tag{5.23}$$

$$= \left[\begin{bmatrix} A^G, \begin{bmatrix} B^{G1} & \begin{bmatrix} 0 & B^{G1} \end{bmatrix} \end{bmatrix}, \begin{bmatrix} C^{G1} \\ \begin{bmatrix} C^{G1} \\ 0 \end{bmatrix} \end{bmatrix}, \begin{bmatrix} D^{G11} & \begin{bmatrix} I & D^{G11} \end{bmatrix} \\ \begin{bmatrix} D^{G11} \\ I \end{bmatrix} & \begin{bmatrix} I & D^{G11} \\ 0 & I \end{bmatrix} \end{bmatrix} \right]_+^{ic}$$

$$\underline{G} = \begin{bmatrix} \underline{G}_{11} & \underline{G}_{12} \\ \underline{G}_{21} & \underline{G}_{22} \end{bmatrix} \tag{5.24}$$

and the interconnection

$$\begin{bmatrix} \underline{\varphi} \\ \underline{e} \end{bmatrix} \begin{bmatrix} \underline{G}_{11} & \underline{G}_{12} & \underline{G}_{1\xi} \\ \underline{G}_{21} & \underline{G}_{22} & \underline{G}_{2\xi} \end{bmatrix} \begin{bmatrix} \underline{\vartheta} \\ \underline{d} \\ \underline{\xi}^G \end{bmatrix}, \quad \underline{\vartheta} = \Delta(\underline{\varphi}) \tag{5.25}$$

and verifying that $(\underline{G}^{ic}, \mathbf{\Delta})$ is either robustly well-posed or robustly stable. Clearly, $(\underline{G}^{ic}, \mathbf{\Delta})$

is robustly well-posed if and only if $(G^{ic}, \mathbf{\Delta})$ is robustly well-posed. In like manner, $(\underline{G}^{ic}, \mathbf{\Delta})$ is robustly stable if and only if $(G^{ic}, \mathbf{\Delta})$ is robustly stable.

Naturally following from our discussion on robust stability, we introduce the notion of robust performance.

Definition 5.14. $(G^{ic}, \mathbf{\Delta})$ defined in (5.20) has a robust $(\Xi, \mathcal{D})$-to-ℓ_2 gain performance level of (λ, γ) if it is robustly stable and $\|e\|_{\ell_2} < \gamma\|d\|_{\ell_2} + \lambda$ for all $d \in \mathcal{D} \subseteq \ell_2$, $\xi^G \in \mathcal{E}(\Xi)$, and $\Delta \in \mathbf{\Delta}$. The term "robust $(\Xi, \mathcal{D})$-to-ℓ_2 gain performance level" is parsimoniously referred to as robust performance.

IQC theory provides a powerful means of asserting robust stability and robust performance. This is achieved by means of IQC multipliers.

Definition 5.15. An *IQC multiplier* $\Pi = \begin{bmatrix} \Pi_{11} & \Pi_{12} \\ \Pi_{12}^* & \Pi_{22} \end{bmatrix}$ is a self-adjoint partitioned dichotomic node.

This definition of an IQC multiplier is a time-varying generalization of the typical designation for Π. In [11], the authors state that Π is customarily any Hermitian-valued function in $\mathcal{RL}_\infty$, but it can be any measurable Hermitian-valued function mapping the complex unit circle* to $\mathbb{C}^{(n_\varphi+n_\vartheta)\times(n_\varphi+n_\vartheta)}$, where $\varphi(k) \in \mathbb{R}^{n_\varphi}$ and $\vartheta(k) \in \mathbb{R}^{n_\vartheta}$. Though the latter definition permits IQC multipliers to lie outside $\mathcal{RL}_\infty$, it still does not capture time-varying dynamical systems. With Definition 5.15, new time-varying uncertainties can be better treated.

Definition 5.16. The set $\mathbf{\Delta}$ *satisfies the IQC defined by* Π ($\mathbf{\Delta} \in \mathrm{IQC}(\Pi)$) if

$$\left\langle \begin{bmatrix} \varphi \\ \Delta(\varphi) \end{bmatrix}, \begin{bmatrix} \Pi_{11} & \Pi_{12} \\ \Pi_{12}^* & \Pi_{22} \end{bmatrix} \begin{bmatrix} \varphi \\ \Delta(\varphi) \end{bmatrix} \right\rangle \geq 0, \quad \text{for all } \varphi \in \ell_2,\ \Delta \in \mathbf{\Delta}.$$

*the $j\omega$ axis for continuous-time dynamics

Given the factors (Ψ, S) of Π, where

$$\Psi = \left[A^{\Psi}, \begin{bmatrix} B^{\Psi 1} & B^{\Psi 2} \end{bmatrix}, C^{\Psi}, \begin{bmatrix} D^{\Psi 1} & D^{\Psi 2} \end{bmatrix}\right]_{+} \tag{5.26}$$

the set $\mathbf{\Delta}$ *satisfies the soft IQC defined by* (Ψ, S) ($\mathbf{\Delta} \in \mathrm{SIQC}(\Psi, S)$) if

$$J^{\Psi,S}(0, 0, \{\!\!\{\varphi, \Delta(\varphi)\}\!\!\}) \geq 0, \quad \text{for all } \varphi \in \ell_2,\ \Delta \in \mathbf{\Delta}.$$

The set $\mathbf{\Delta}$ *satisfies the hard IQC defined by the factors* (Ψ, S) ($\mathbf{\Delta} \in \mathrm{HIQC}(\Psi, S)$) if

$$J_T^{\Psi,S}(0, 0, \{\!\!\{\varphi, \Delta(\varphi)\}\!\!\}) \geq 0, \quad \text{for all } \varphi \in \ell_{2e},\ \Delta \in \mathbf{\Delta},\ T \in 0_+.$$

Per the previous discussion on Popov indices, if $\mathbf{\Delta} \in \mathrm{IQC}(\Pi)$, then $\mathbf{\Delta} \in \mathrm{SIQC}(\Psi, S)$ for any factorization (Ψ, S) of Π. However, the same is not true of hard IQCs; $\mathbf{\Delta}$ may satisfy the hard IQC defined by a certain factorization of Π while failing to satisfy the hard IQC defined by another factorization of Π. Though this chapter allows the utilization of time-varying IQC multipliers, the forthcoming results require Π to satisfy an additional condition.

Definition 5.17. The IQC multiplier Π is a *(strictly) positive-negative multiplier on* $\ell_2(N_+)$ if there exists a scalar $\epsilon \geq 0$ ($\epsilon > 0$) such that $\langle u, \Pi_{11} u \rangle \geq \epsilon \|u\|^2$ and $\langle v, \Pi_{22} v \rangle \leq -\epsilon \|u\|^2$ for all $u, v \in \ell_2(N_+)$. If Π is (strictly) positive-negative on ℓ_2, we simply say it is (strictly) positive-negative.

Though positive-negative IQC multipliers are a subclass of the IQC multipliers defined in Definition 5.15, such a subclass is not overly restrictive. Nearly all the IQC multipliers in the literature to date are positive-negative (see, for example, [11, 20]). A noted class of IQC multipliers which are not positive-negative consists of full-block multipliers characterizing repeated sector-bounded nonlinearities [20, 91].

5.2.1 Robust performance of uncertain systems

To assess the robust performance of $(G^{ic}, \mathbf{\Delta})$, we define

$$A^H = \begin{bmatrix} A^G & 0 \\ B^{\Psi 1} C^{G1} & A^\Psi \end{bmatrix}, \quad B^H = \begin{bmatrix} B^{G1} \\ B^{\Psi 1} D^{G11} + B^{\Psi 2} \end{bmatrix}, \quad B^{H2} = \begin{bmatrix} B^{G2} \\ B^{\Psi 1} D^{G12} \end{bmatrix} \tag{5.27}$$

$$C^H = \begin{bmatrix} D^{\Psi 1} C^{G1} & C^\Psi \end{bmatrix}, \quad D^H = D^{\Psi 1} D^{G11} + D^{\Psi 2}, \quad D^{H12} = \begin{bmatrix} D^{\Psi 1} D^{G12} \end{bmatrix} \tag{5.28}$$

$$C^{H2} = \begin{bmatrix} C^{G2} & 0 \end{bmatrix}, \quad D^{H21} = D^{G21}, \quad D^{H22} = D^{G22} \tag{5.29}$$

and note that, for $\vartheta, d \in \ell_{2e}$ $(\vartheta, d \in \ell_2)$ and $\xi^G \in \mathbb{R}^{n_G}$, the signals defined by

$$\begin{bmatrix} \varphi \\ e \end{bmatrix} = G^{ic} \left\{ \begin{bmatrix} \vartheta \\ d \end{bmatrix}, \xi^G \right\}, \qquad r = \Psi \begin{bmatrix} \varphi \\ \vartheta \end{bmatrix}$$

$$x^G = \mathcal{L}_0^G \begin{bmatrix} \vartheta \\ d \end{bmatrix} + \mathcal{S}_0^G \xi^G, \qquad x^\Psi = \mathcal{L}_0^\Psi \begin{bmatrix} \varphi \\ \vartheta \end{bmatrix}, \qquad x^H = \begin{bmatrix} x^G \\ x^\Psi \end{bmatrix}$$

are in ℓ_{2e} (ℓ_2) and satisfy

$$\begin{bmatrix} Z^* \left({}_{T+1} x^H \right) \\ {}_T r \\ {}_T e \end{bmatrix} = \begin{bmatrix} A^H & B^H & B^{H2} \\ C^H & D^H & D^{H12} \\ C^{H2} & D^{H21} & D^{H22} \end{bmatrix} \begin{bmatrix} {}_T x^H \\ {}_T \vartheta \\ {}_T d \end{bmatrix}.$$

Theorem 5.18. *Given the partitioned IC node G^{ic} defined in* (5.19a)-(5.19b)*, the uncertain system $(G^{ic}, \mathbf{\Delta})$ defined by* (5.20) *has a robust (Ξ, ℓ_2)-to-ℓ_2 gain performance level of (λ, γ) if $(G^{ic}, \mathbf{\Delta})$ is robustly well-posed and there exists a positive-negative IQC multiplier Π with factors (Ψ, S) such that*

(a) $\mathbf{\Delta} \in \mathrm{IQC}(\Pi)$*;*

(b) there exist a memoryless operator $P = P^*$, $\epsilon > 0$, and $\gamma > 0$ satisfying

$$\begin{bmatrix} A^H & B^H & B^{H2} \\ C^H & D^H & D^{H12} \\ C^{H2} & D^{H21} & D^{H22} \end{bmatrix}^* \begin{bmatrix} Z^*PZ & 0 & 0 \\ 0 & S & 0 \\ 0 & 0 & I \end{bmatrix} \begin{bmatrix} A^H & B^H & B^{H2} \\ C^H & D^H & D^{H12} \\ C^{H2} & D^{H21} & D^{H22} \end{bmatrix} - \begin{bmatrix} P & 0 & 0 \\ 0 & 0 & 0 \\ 0 & 0 & \gamma^2 I \end{bmatrix} \preceq -\epsilon I \quad (5.30)$$

$$\begin{bmatrix} I_{n_G} & 0 \end{bmatrix} (\llbracket P \rrbracket (0)) \begin{bmatrix} I_{n_G} & 0 \end{bmatrix}^T \preceq \lambda^2 \Xi. \quad (5.31)$$

This theorem gives a sufficient condition for asserting the robust performance of $(G^{ic}, \mathbf{\Delta})$. It is similar to the result in [41], except it incorporates the effect of non-zero initial conditions and allows G and Π to be time-varying in general. The fact that Π has a more general designation allows us to define IQCs more appropriate for uncertainties with time-domain characteristics.

To prove Theorem 5.18, we rely on two central ideas. First, one can assert robust performance using the dissipativity-based Lemma 5.19, which relies on more conservative hypotheses. Second, the conservative hypotheses of Lemma 5.19 hold when using strictly positive-negative multipliers to satisfy hypotheses (a) and (b) in Theorem 5.18.

Lemma 5.19. *Given the partitioned IC node G^{ic} defined in* (5.19a)-(5.19b)*, the uncertain system $(G^{ic}, \mathbf{\Delta})$ defined by* (5.20) *has a robust (Ξ, ℓ_2)-to-ℓ_2 gain performance level of (λ, γ) if $(G, \mathbf{\Delta})$ is robustly well-posed and there exists an IQC multiplier Π with factors (Ψ, S) such that*

(a) $\mathbf{\Delta} \in \mathrm{HIQC}(\Psi, S)$;

(b) there exist $\gamma > 0$, $\epsilon > 0$, and a memoryless operator $P \succeq 0$ satisfying (5.30) *and* (5.31)*.*

Proof. The proof of this lemma makes use of dissipation arguments found in [35,36,38]. Since $(G^{ic}, \mathbf{\Delta})$ is robustly well-posed, then for all $d \in \ell_2$, $\Delta \in \mathbf{\Delta}$, and $\xi^G \in \mathcal{E}(\Xi)$, there are unique

signals $\vartheta,\ \varphi, e \in \ell_{2e}$ which satisfy (5.20). Additionally define the ℓ_{2e} signals $r = \Psi\{\!\{\varphi, \vartheta\}\!\}$, $x^G = \mathcal{L}_0^G\{\!\{\vartheta, d\}\!\} + \mathcal{S}_0^G\xi^G$, $x^\Psi = \mathcal{L}_0^\Psi\{\!\{\varphi, \vartheta\}\!\}$ and $x^H = \{\!\{x^G, x^\Psi\}\!\}$. By (5.30), for all $T \in 0_+$,

$$\left\langle \begin{bmatrix} A^H & B^H & B^{H2} \\ C^H & D^H & D^{H12} \\ C^{H2} & D^{H21} & D^{H22} \end{bmatrix} \begin{bmatrix} {}_Tx^H \\ {}_T\vartheta \\ {}_Td \end{bmatrix}, \begin{bmatrix} Z^*PZ & 0 & 0 \\ 0 & S & 0 \\ 0 & 0 & I \end{bmatrix} \begin{bmatrix} A^H & B^H & B^{H2} \\ C^H & D^H & D^{H12} \\ C^{H2} & D^{H21} & D^{H22} \end{bmatrix} \begin{bmatrix} {}_Tx^H \\ {}_T\vartheta \\ {}_Td \end{bmatrix} \right\rangle$$
$$- \left\langle \begin{bmatrix} {}_Tx^H \\ {}_Td \end{bmatrix}, \begin{bmatrix} P & 0 \\ 0 & \gamma^2 I \end{bmatrix} \begin{bmatrix} {}_Tx^H \\ {}_Td \end{bmatrix} \right\rangle \le -\epsilon(\|{}_Tx^H\|_{\ell_2}^2 + \|{}_T\vartheta\|_{\ell_2}^2 + \|{}_Td\|_{\ell_2}^2) \quad (5.32)$$

which simplifies to

$$\begin{aligned}
&(\gamma^2 - \epsilon)\|{}_Td\|_{\ell_2}^2 - \epsilon(\|{}_T\vartheta\|_{\ell_2}^2 + \|{}_Tx^H\|_{\ell_2}^2) \\
&\quad \ge \left\langle {}_{T+1}x^H, ZZ^*PZZ^*\ {}_{T+1}x^H \right\rangle - \left\langle {}_Tx^H, P\ {}_Tx^H \right\rangle + \|{}_Te\|_{\ell_2}^2 + \langle {}_Tr, S\ {}_Tr \rangle \\
&\quad = x^H(T)^T \left([\![P]\!](T) \right) x^H(T) - \left[(\xi^G)^T, 0 \right] \left([\![P]\!](0) \right) \left[(\xi^G)^T, 0 \right]^T \\
&\qquad\qquad + \|{}_Te\|_{\ell_2}^2 + J_T^{\Psi,S}(0, 0, \{\!\{\varphi, \Delta(\varphi)\}\!\}) \\
&\quad \ge \|{}_Te\|_{\ell_2}^2 - \left[(\xi^G)^T, 0 \right] \left([\![P]\!](0) \right) \left[(\xi^G)^T, 0 \right]^T \qquad (5.33)
\end{aligned}$$

where the last inequality is obtained because $P \succeq 0$ and $\mathbf{\Delta} \in \mathrm{HIQC}(\Psi, S)$. The inequality (5.33) implies that

$$\begin{aligned}
\|{}_Te\|_{\ell_2}^2 + \epsilon(\|{}_T\vartheta\|_{\ell_2}^2 + \|{}_Tx^H\|_{\ell_2}^2) &\le (\gamma^2 - \epsilon)\|{}_Td\|_{\ell_2}^2 + \left[(\xi^G)^T, 0 \right] P(0) \left[(\xi^G)^T, 0 \right]^T \qquad (5.34) \\
&\le (\gamma^2 - \epsilon)\|{}_Td\|_{\ell_2}^2 + \lambda^2 \left((\xi^G)^T \Xi\ \xi^G \right) \qquad (5.35) \\
&\le (\gamma^2 - \epsilon)\|{}_Td\|_{\ell_2}^2 + \lambda^2 \qquad (5.36)
\end{aligned}$$

where (5.35) is implied by the constraint (5.31) and (5.36) is due to $\xi^G \in \mathcal{E}(\Xi)$. Since the left-hand side (LHS) of (5.34) monotonically increases with T, and $\lim_{T\to\infty} \|{}_Td\|_{\ell_2}^2 = \|d\|_{\ell_2}^2$, the

limit as $T \to \infty$ of the LHS of (5.34) exists, providing

$$\|e\|_{\ell_2}^2 + \epsilon(\|\vartheta\|_{\ell_2}^2 + \|x^H\|_{\ell_2}^2) \leq (\gamma^2 - \epsilon)\|d\|_{\ell_2}^2 + \lambda^2 \tag{5.37}$$

which implies that e, ϑ, and x^H are ℓ_2 signals. Because G^{ic} is bounded on ℓ_2, we also see that φ is an ℓ_2 signal, concluding that $(G^{ic}, \mathbf{\Delta})$ is robustly stable. By (5.37) we also observe that $\|e\|_{\ell_2} \leq \gamma\|d\|_{\ell_2} + \lambda$. □

It is apparent that the hypotheses (a) and (b) in Lemma 5.19 are more conservative than their counterparts in Theorem 5.18. These hypotheses can be relaxed when using strictly positive-negative multipliers.

Lemma 5.20. *Given an IQC multiplier* Π *with factors* (Ψ, S)*, if there exists a memoryless operator* $P = P^*$ *such that* (5.30) *holds, then for all* $N \in 0_+$*,* $\xi^G \in \mathbb{R}^{n_G}$*, and* $\xi \in \mathbb{R}^n$*,*

$$(\xi^H)^T \left(\llbracket P \rrbracket (N)\right) \xi^H \geq \underline{J}^{\Psi,S}(N, \xi) \tag{5.38}$$

where $\xi^H = \begin{bmatrix} (\xi^G)^T & \xi^T \end{bmatrix}^T$.

Proof. Define the partitioned causal node

$$H = \Psi[G_{11}^* \ I]^* = [A^H, B^H, C^H, D^H]_+. \tag{5.39}$$

For any $\vartheta \in \ell_2(N_+)$, $\xi^H \in \mathbb{R}^{n_H}$, define $x^H = \mathcal{S}_N^H \xi^H + \mathcal{L}_N^H \vartheta$, $r = C^H x^H + D^H \vartheta$, and $\varphi = G_{11}\vartheta + C^{G1}\mathcal{S}_N^G \xi^G$. With these definitions, $\langle r, Sr \rangle = J^{H,S}(N, \xi^H, \vartheta)$ and (5.13) is satisfied (replacing x with x^H, A with A^H, B with B^H and u with ϑ). Furthermore, because H and G_{11} are partitioned causal nodes, x^H, r, φ are in $\ell_2(N_+)$. Invoking (5.30) we have

$$\left\langle \begin{bmatrix} A^H & B^H & B^{H2} \\ C^H & D^H & D^{H12} \\ C^{H2} & D^{H21} & D^{H22} \end{bmatrix} \begin{bmatrix} x^H \\ \vartheta \\ 0 \end{bmatrix}, \begin{bmatrix} Z^*PZ & 0 & 0 \\ 0 & S & 0 \\ 0 & 0 & I \end{bmatrix} \begin{bmatrix} A^H & B^H & B^{H2} \\ C^H & D^H & D^{H12} \\ C^{H2} & D^{H21} & D^{H22} \end{bmatrix} \begin{bmatrix} x^H \\ \vartheta \\ 0 \end{bmatrix} \right\rangle$$

$$-\left\langle \begin{bmatrix} x^H \\ 0 \end{bmatrix}, \begin{bmatrix} P & 0 \\ 0 & \gamma^2 I \end{bmatrix} \begin{bmatrix} x^H \\ 0 \end{bmatrix} \right\rangle \leq -\epsilon(\|x^H\|_{\ell_2}^2 + \|\vartheta\|_{\ell_2}^2).$$

Defining $p = C^{H2}x^H + D^{H21}\vartheta$ and recalling (5.15), the previous inequality reduces to

$$\begin{aligned} -\epsilon(\|x^H\|_{\ell_2}^2 + \|\vartheta\|_{\ell_2}^2) - \|p\|_{\ell_2}^2 &\geq \left\langle \mathbb{P}_N^+ Z^* x^H, Z^* P Z\ \mathbb{P}_N^+ Z^* x^H \right\rangle - \left\langle x^H, P x^H \right\rangle + J^{H,S}(N, \xi^H, \vartheta) \\ &= -(\xi^H)^T \left([\![P]\!] (N) \right) \xi^H + J^{H,S}(N, \xi^H, \vartheta) \\ &= -(\xi^H)^T \left([\![P]\!] (N) \right) \xi^H + J^{\Psi,S}\left(N, \xi, \{\!\{ \varphi, \vartheta \}\!\}\right). \end{aligned} \tag{5.40}$$

Because (5.40) holds for any $\vartheta \in \ell_2(N_+)$, we obtain

$$\begin{aligned} (\xi^H)^T \left([\![P]\!] (N) \right) \xi^H &\geq \sup_{\vartheta \in \ell_2(N_+)} J^{\Psi,S}\left(N, \xi, \{\!\{ \varphi, \vartheta \}\!\}\right) \\ &\geq \sup_{\vartheta \in \ell_2(N_+)} \inf_{\varphi \in \ell_2(N_+)} J^{\Psi,S}\left(N, \xi, \{\!\{ \varphi, \vartheta \}\!\}\right) = \underline{J}^{\Psi,S}(N, \xi) \end{aligned} \tag{5.41}$$

thereby proving the result. □

While the last lemma connects hypothesis (b) in Lemma 5.19 to the lower Popov index, the next lemma establishes a relationship between hypothesis (a) in Lemma 5.19 and the upper Popov index.

Lemma 5.21. *Given an IQC multiplier* Π *with factors* (Ψ, S)*, if* $\mathbf{\Delta} \in \mathrm{IQC}(\Pi)$*, then for all* $\varphi \in \ell_{2e}$*,* $\Delta \in \mathbf{\Delta}$*, and* $N \in 0_+$*,*

$$J_N^{\Psi,S}\left(0, 0, \{\!\{ \varphi, \Delta(\varphi) \}\!\}\right) \geq -\bar{J}^{\Psi,S}(N, x(N)) \tag{5.42}$$

where $x = \mathcal{L}_0^{\Psi}\{\!\{ \varphi, \Delta(\varphi) \}\!\}$*.*

Proof. Since $\mathbf{\Delta} \in \mathrm{IQC}(\Pi)$, then for all $\varphi \in \ell_2$ and $N \in 0_+$,

$$\begin{aligned} 0 &\leq J^{\Psi,S}\left(0, 0, \{\!\{ \varphi, \Delta(\varphi) \}\!\}\right) \\ &= J_N^{\Psi,S}\left(0, 0, \{\!\{ {}_N\varphi, {}_N(\Delta({}_N\varphi)) \}\!\}\right) + J^{\Psi,S}\left(N, x(N), \{\!\{ {}^N\varphi, {}^N(\Delta(\varphi)) \}\!\}\right) \end{aligned} \tag{5.43}$$

where (5.43) can be established by invoking the causality of Ψ and Δ. Thus, for all $\varphi \in \ell_2,\ N \in 0_+,$ and $\Delta \in \mathbf{\Delta}$,

$$J_N^{\Psi,S}\left(0,0,\{\!\!\{ {}_N\varphi, {}_N(\Delta({}_N\varphi))\}\!\!\}\right) \geq -J^{\Psi,S}\left(N, x(N), \{\!\!\{ {}^N\varphi, {}^N\left(\Delta(\varphi)\right)\}\!\!\}\right). \tag{5.44}$$

Because (5.44) holds for all $\varphi \in \ell_2$ and the LHS of (5.44) is independent of ${}^N\varphi$, the supremum over ${}^N\varphi \in \ell_2(N_+)$ of the right-hand side (RHS) of (5.44) can be taken, yielding

$$\begin{aligned} J_N^{\Psi,S}\left(0,0,\{\!\!\{ {}_N\varphi, {}_N(\Delta({}_N\varphi))\}\!\!\}\right) &\geq \sup_{{}^N\varphi\in\ell_2(N_+)} -J^{\Psi,S}\left(N, x(N), \{\!\!\{ {}^N\varphi, {}^N(\Delta(\varphi))\}\!\!\}\right) \\ &\geq \sup_{{}^N\varphi\in\ell_2(N_+)} \inf_{{}^N\vartheta\in\ell_2(N_+)} -J^{\Psi,S}\left(N, x(N), \{\!\!\{ {}^N\varphi, {}^N\vartheta\}\!\!\}\right) \\ &\geq -\inf_{{}^N\varphi\in\ell_2(N_+)} \sup_{{}^N\vartheta\in\ell_2(N_+)} J^{\Psi,S}\left(N, x(N), \{\!\!\{ {}^N\varphi, {}^N\vartheta\}\!\!\}\right) \\ &= -\bar{J}^{\Psi,S}(N, x(N)). \end{aligned} \tag{5.45}$$

Invoking the causality of Δ and noting that $J_N^{\Psi,S}(0,\xi,{}_Nu) = J_N^{\Psi,S}(0,\xi,u)$ for all $\xi \in \mathbb{R}^n$, $u \in \ell_2$, the LHS of (5.45) can be restated as the LHS of (5.42). Up to this point we have proven that (5.42) holds for all $\Delta \in \mathbf{\Delta}$, $N \in 0_+$, and $\varphi \in \ell_2$. However, (5.42) must hold for all signals φ in the larger set ℓ_{2e}. To establish this, we define two different sets

$$\begin{aligned} \mathcal{J}_N^{\ell_{2e}} &= \{j \in \mathbb{R} \mid j = J_N^{\Psi,S}(0,0,\{\!\!\{\varphi,\Delta(\varphi)\}\!\!\}),\ \text{for } \Delta \in \mathbf{\Delta} \text{ and } \varphi \in \ell_{2e}\} \\ \mathcal{J}_N^{\ell_2} &= \{j \in \mathbb{R} \mid j = J_N^{\Psi,S}(0,0,\{\!\!\{\varphi,\Delta(\varphi)\}\!\!\}),\ \text{for } \Delta \in \mathbf{\Delta} \text{ and } \varphi \in \ell_2\} \end{aligned}$$

and prove that $\mathcal{J}_N^{\ell_{2e}} = \mathcal{J}_N^{\ell_2}$ for all $N \in 0_+$. Therefore, a lower bound on the LHS of (5.42) for all $\Delta \in \mathbf{\Delta}$, $N \in 0_+$, $\varphi \in \ell_2$ remains a lower bound when φ may be an element of ℓ_{2e}. That $\mathcal{J}_N^{\ell_2} \subseteq \mathcal{J}_N^{\ell_{2e}}$ is easy to see. We establish $\mathcal{J}_N^{\ell_{2e}} \subseteq \mathcal{J}_N^{\ell_2}$ by invoking causality of Ψ and Δ.

Specifically, given $N \in 0_+$, we have

$$
\begin{aligned}
& j \in \mathcal{J}_N^{\ell_{2e}} \\
\iff & \exists\ \varphi \in \ell_{2e}, \Delta \in \mathbf{\Delta} \text{ s.t.:} \quad j = J_N^{\Psi,S}(0,0,\{\!\!\{\varphi, \Delta(\varphi)\}\!\!\}) && \text{(by definition)} \\
\iff & \exists\ \varphi \in \ell_{2e}, \Delta \in \mathbf{\Delta} \text{ s.t.:} \quad j = J_N^{\Psi,S}(0,0,\{\!\!\{{}_N\varphi, {}_N(\Delta(\varphi))\}\!\!\}) && \text{(by causality of } \Psi) \\
\iff & \exists\ \varphi \in \ell_{2e}, \Delta \in \mathbf{\Delta} \text{ s.t.:} \quad j = J_N^{\Psi,S}(0,0,\{\!\!\{{}_N\varphi, {}_N(\Delta({}_N\varphi))\}\!\!\}) && \text{(by causality of } \Delta) \\
\iff & \exists\ \tilde{\varphi} \in \ell_2, \Delta \in \mathbf{\Delta} \text{ s.t.:} \quad j = J_N^{\Psi,S}(0,0,\{\!\!\{\tilde{\varphi}, {}_N(\Delta(\tilde{\varphi}))\}\!\!\}) && \text{(defining } \tilde{\varphi} = {}_N\varphi) \\
\iff & \exists\ \tilde{\varphi} \in \ell_2, \Delta \in \mathbf{\Delta} \text{ s.t.:} \quad j = J_N^{\Psi,S}(0,0,\{\!\!\{\tilde{\varphi}, \Delta(\tilde{\varphi})\}\!\!\}) && \text{(by causality of } \Psi) \\
\iff & j \in \mathcal{J}_N^{\ell_2} && \text{(by definition)}
\end{aligned}
$$

which concludes the proof. □

When Π is LTI, the result $J_N^{\Psi,S}(0,0,\{\!\!\{\varphi, \Delta(\varphi)\}\!\!\}) \geq -\bar{J}^{\Psi,S}(0, x(N))$ is given in [15]. The proof therein relies on the fact that Π is time-invariant. In this work, because Π may be time-varying, it is important to note that the associated lower bound in (5.42) is determined by the upper Popov index *starting at* N rather than 0.

The next lemma is key to connecting Lemmas 5.20 and 5.21 to Lemma 5.19.

Lemma 5.22. *For every strictly positive-negative IQC multiplier* Π *with factors* (Ψ, S), $N \in 0_+$, *and* $\xi \in \mathbb{R}^n$,

(1) there exists a stabilizing solution X *to the* $DDRE(\Psi, S)$;

(2) $\underline{J}^{\Psi,S}(N,\xi) = \bar{J}^{\Psi,S}(N,\xi) = \xi^T X(N)\xi$;

(3) there exists a factorization $(\bar{\Psi}, \bar{S})$ *of* Π, *wherein* $\bar{\Psi} = [A^{\Psi}, B^{\Psi}, C^{\bar{\Psi}}, D^{\bar{\Psi}}]_+$, $\bar{\Psi}^{-1}$ *is a bounded causal node, and the stabilizing solution to the* $DDRE(\bar{\Psi}, \bar{S})$ *is* $\bar{X} = 0$.

Proof. (1): By the definition of strictly positive-negative multipliers, for all $u \in \ell_2$, there exists a scalar $\epsilon > 0$ such that $\langle u, \Pi_{11} u \rangle \geq \epsilon \|u\|^2$ and $\langle u, \Pi_{22} u \rangle \leq -\epsilon \|u\|^2$. This implies that $\langle \bar{u}, \Pi_{11} \bar{u} \rangle \geq \epsilon \|\bar{u}\|^2$ and $\langle \bar{u}, \Pi_{22} \bar{u} \rangle \leq -\epsilon \|\bar{u}\|^2$ for all $\bar{u} \in \ell_2(N_+)$, which implies that ${}^N\Pi$ is strictly positive-negative on $\ell_2(N_+)$ for all $N \in 0_+$. Because ${}^N\Pi_{22}$ is negative definite, it is bijective on $\ell_2(N_+)$ and, by the bounded inverse theorem [92], has a bounded inverse on $\ell_2(N_+)$. In conjunction with ${}^N\Pi_{11}$ being positive definite, we see that ${}^N\Pi^{\times} = {}^N\Pi_{11} - {}^N\Pi_{12} ({}^N\Pi_{22})^{-1} {}^N\Pi_{12}^*$ is positive definite and has a bounded inverse on $\ell_2(N_+)$. Hence, ${}^N\Pi$ can be written as

$$
{}^N\Pi = \begin{bmatrix} I & {}^N\Pi_{12} {}^N\Pi_{22}^{-1} \\ 0 & I \end{bmatrix} \begin{bmatrix} {}^N\Pi^{\times} & 0 \\ 0 & {}^N\Pi_{22} \end{bmatrix} \begin{bmatrix} I & 0 \\ {}^N\Pi_{22}^{-1} {}^N\Pi_{12}^* & I \end{bmatrix}
$$

whose bounded inverse on $\ell_2(N_+)$ can be easily obtained. Invoking Theorem 3.2.2 from [48], if ${}^N\Pi$ is boundedly invertible on $\ell_2(N_+)$ for all $N \in 0_+$, then there exists a stabilizing solution to the $DDRE(\Psi, S)$.

(2): Define $u_N^\star = \{\!\!\{\varphi_N^\star, \vartheta_N^\star\}\!\!\} = -(\mathcal{R}_N^{\Psi,S})^{-1}(\mathcal{P}_N^{\Psi,S})^* \xi$ and $x_N^\star = \mathcal{L}_N^\Psi u_N^\star + \mathcal{S}_N^\Psi \xi$. Because $(\mathcal{R}_N^{\Psi,S})^{-1} = ({}^N\Pi)^{-1}$ is bounded, then $\varphi_N^\star, \vartheta_N^\star \in \ell_2(N_+)$, thereby ensuring that $J^{\Psi,S}(N, \xi, u_N^\star)$ is well-defined. Hence,

$$
\begin{aligned}
J(N, \xi, u_N^\star) &= \left\langle \begin{bmatrix} \xi \\ u_N^\star \end{bmatrix}, \begin{bmatrix} \mathcal{X}_N^{\Psi,S} & \mathcal{P}_N^{\Psi,S} \\ (\mathcal{P}_N^{\Psi,S})^* & \mathcal{R}_N^{\Psi,S} \end{bmatrix} \begin{bmatrix} \xi \\ u_N^\star \end{bmatrix} \right\rangle \\
&= \left\langle \xi, \begin{bmatrix} I & -\mathcal{P}_N^{\Psi,S}(\mathcal{R}_N^{\Psi,S})^{-1} \end{bmatrix} \begin{bmatrix} \mathcal{X}_N^{\Psi,S} & \mathcal{P}_N^{\Psi,S} \\ (\mathcal{P}_N^{\Psi,S})^* & \mathcal{R}_N^{\Psi,S} \end{bmatrix} \begin{bmatrix} I \\ -(\mathcal{R}_N^{\Psi,S})^{-1}(\mathcal{P}_N^{\Psi,S})^* \end{bmatrix} \xi \right\rangle \\
&= \left\langle \xi, \left(\mathcal{X}_N^{\Psi,S} - \mathcal{P}_N^{\Psi,S}(\mathcal{R}_N^{\Psi,S})^{-1}(\mathcal{P}_N^{\Psi,S})^* \right) \xi \right\rangle.
\end{aligned}
$$

Following similar arguments to those in the proof of [48, Theorem 3.2.2], $\mathcal{X}_N^{\Psi,S} - \mathcal{P}_N^{\Psi,S}(\mathcal{R}_N^{\Psi,S})^{-1}(\mathcal{P}_N^{\Psi,S})^*$

$= X(N)$, whereby $J(N,\xi,u_N^\star) = \xi^T X(N)\xi$. Now, for any $\varphi_N, \vartheta_N \in \ell_2(N_+)$ define $u_N = \{\!\!\{\varphi_N, \vartheta_N\}\!\!\}$, $x = \mathcal{L}_N^\Psi u_N$, $\tilde{u}_N = u_N - u_N^\star$, and $\tilde{x}_N = x_N - x_N^\star$, and observe that

$$
\begin{aligned}
J^{\Psi,S}(N,\xi,u_N) &= \left\langle \begin{bmatrix} x_N^\star + \tilde{x}_N \\ u_N^\star + \tilde{u}_N \end{bmatrix}, \begin{bmatrix} {}^N Q & {}^N L \\ ({}^N L)^* & {}^N R \end{bmatrix} \begin{bmatrix} x_N^\star + \tilde{x}_N \\ u_N^\star + \tilde{u}_N \end{bmatrix} \right\rangle \\
&= J^{\Psi,S}(N,\xi,u_N^\star) + J^{\Psi,S}(N,0,\tilde{u}_N) + 2\left\langle \begin{bmatrix} \tilde{x}_N \\ \tilde{u}_N \end{bmatrix}, \begin{bmatrix} {}^N Q & {}^N L \\ ({}^N L)^* & {}^N R \end{bmatrix} \begin{bmatrix} x_N^\star \\ u_N^\star \end{bmatrix} \right\rangle \\
&= J^{\Psi,S}(N,\xi,u_N^\star) + J^{\Psi,S}(N,0,\tilde{u}_N) + 2\left\langle \begin{bmatrix} 0 \\ \tilde{u}_N \end{bmatrix}, \begin{bmatrix} \mathcal{S}_N^\Psi & \mathcal{L}_N^\Psi \\ 0 & I \end{bmatrix}^* \begin{bmatrix} {}^N Q & {}^N L \\ ({}^N L)^* & {}^N R \end{bmatrix} \begin{bmatrix} \mathcal{S}_N^\Psi & \mathcal{L}_N^\Psi \\ 0 & I \end{bmatrix} \begin{bmatrix} \xi \\ u_N^\star \end{bmatrix} \right\rangle \\
&= J^{\Psi,S}(N,\xi,u_N^\star) + J^{\Psi,S}(N,0,\tilde{u}_N) + 2\left\langle \begin{bmatrix} 0 \\ \tilde{u}_N \end{bmatrix}, \begin{bmatrix} \mathcal{X}_N^{\Psi,S} & \mathcal{P}_N^{\Psi,S} \\ (\mathcal{P}_N^{\Psi,S})^* & \mathcal{R}_N^{\Psi,S} \end{bmatrix} \begin{bmatrix} I \\ -(\mathcal{R}_N^{\Psi,S})^{-1}(\mathcal{P}_N^{\Psi,S})^* \end{bmatrix} \xi \right\rangle \\
&= J^{\Psi,S}(N,\xi,u_N^\star) + J^{\Psi,S}(N,0,\tilde{u}_N) + 2\left\langle \begin{bmatrix} 0 \\ \tilde{u}_N \end{bmatrix}, \begin{bmatrix} X(N) \\ 0 \end{bmatrix} \xi \right\rangle \\
&= J^{\Psi,S}(N,\xi,u_N^\star) + J^{\Psi,S}(N,0,\tilde{u}_N).
\end{aligned}
$$

With the previous equation we have

$$J^{\Psi,S}\left(N,\xi,\{\!\!\{\varphi_N,\vartheta_N^\star\}\!\!\}\right) - J^{\Psi,S}\left(N,\xi,\{\!\!\{\varphi_N^\star,\vartheta_N^\star\}\!\!\}\right) = J^{\Psi,S}\left(N,\xi,\{\!\!\{\tilde{\varphi}_N,0\}\!\!\}\right) \tag{5.46}$$

$$J^{\Psi,S}\left(N,\xi,\{\!\!\{\varphi_N^\star,\vartheta_N\}\!\!\}\right) - J^{\Psi,S}\left(N,\xi,\{\!\!\{\varphi_N^\star,\vartheta_N^\star\}\!\!\}\right) = J^{\Psi,S}\left(N,\xi,\{\!\!\{0,\tilde{\vartheta}_N\}\!\!\}\right) \tag{5.47}$$

for all $\tilde{\varphi}_N, \tilde{\vartheta}_N \in \ell_2(N_+)$. Recalling that ${}^N\Pi_{11}$ is positive definite, ${}^N\Pi_{22}$ is negative definite, and $J^{\Psi,S}(N,\xi,u_N) = \langle u_N, \Pi u_N\rangle$, (5.46) and (5.47) provide

$$J^{\Psi,S}\left(N,\xi,\{\!\!\{\varphi_N^\star,\vartheta_N\}\!\!\}\right) \le J^{\Psi,S}\left(N,\xi,\{\!\!\{\varphi_N^\star,\vartheta_N^\star\}\!\!\}\right) \le J^{\Psi,S}\left(N,\xi,\{\!\!\{\varphi_N,\vartheta_N^\star\}\!\!\}\right)$$

for all $\varphi_N, \vartheta_N \in \ell_2(N_+)$, or in other words, $(\varphi_N^\star, \vartheta_N^\star)$ is a saddle-point solution. The existence

of a saddle-point solution implies that the lower and upper Popov indices are equal [93], i.e., $\bar{J}^{\Psi,S}(N,\xi) = \underline{J}^{\Psi,S}(N,\xi) = \xi^T X(N)\xi$.

(3): The first part of this statement is proven in [48, Proposition 4.4.3]. Therein, defining

$$R + (B^{\Psi})^* Z^* X Z B^{\Psi} = \begin{bmatrix} \mathcal{Y}_{11} & \mathcal{Y}_{12} \\ \mathcal{Y}_{12}^* & \mathcal{Y}_{22} \end{bmatrix} \tag{5.48}$$

and asserting that $\mathcal{Y}_{11}$ and $-\mathcal{Y}_{22}^{\times} = \mathcal{Y}_{12}^* \mathcal{Y}_{11} \mathcal{Y}_{12} - \mathcal{Y}_{22}$ are positive definite, they construct

$$\bar{S} = \begin{bmatrix} I & 0 \\ 0 & -I \end{bmatrix}, D^{\bar{\Psi}} = \begin{bmatrix} \mathcal{Y}_{11}^{\frac{1}{2}} & \mathcal{Y}_{11}^{-\frac{1}{2}} \mathcal{Y}_{12} \\ 0 & (-\mathcal{Y}_{22}^{\times})^{\frac{1}{2}} \end{bmatrix}, C^{\bar{\Psi}} = \bar{S}(D^{\bar{\Psi}})^{-*}((B^{\Psi})^* Z^* X Z A^{\Psi} + (D^{\Psi})^* S C^{\Psi}). \tag{5.49}$$

That the equations (5.49) and $\bar{\Psi} = [A^{\Psi}, B^{\Psi}, C^{\bar{\Psi}}, D^{\bar{\Psi}}]_+$ indeed define a factorization $(\bar{\Psi}, \bar{S})$ of Π can be demonstrated by invoking the $DDRE(\Psi, S)$. Specifically, we have

$$\begin{aligned} (C^{\bar{\Psi}})^* \bar{S} C^{\bar{\Psi}} &= \left((A^{\Psi})^* Z^* X Z B^{\Psi} + L\right) \left((B^{\Psi})^* Z^* X Z B^{\Psi} + R\right)^{-1} \left(L^* + (B^{\Psi})^* Z^* X Z A^{\Psi}\right) \\ &= Q + (A^{\Psi})^* Z^* X Z A^{\Psi} - X \\ &\qquad \text{for } Q = (C^{\Psi})^* S C^{\Psi},\ L = (C^{\Psi})^* S D^{\Psi}, \text{ and } R = (D^{\Psi})^* S D^{\Psi} \end{aligned}$$

thereby implying

$$\begin{bmatrix} (C^{\bar{\Psi}})^* \\ (D^{\bar{\Psi}})^* \end{bmatrix} \bar{S} \begin{bmatrix} C^{\bar{\Psi}} & D^{\bar{\Psi}} \end{bmatrix} = \begin{bmatrix} Q & L \\ L^* & R \end{bmatrix} + \begin{bmatrix} (A^{\Psi})^* Z^* X Z A^{\Psi} - X & (A^{\Psi})^* Z^* X Z B^{\Psi} \\ (B^{\Psi})^* Z^* X Z A^{\Psi} & (B^{\Psi})^* Z^* X Z B^{\Psi} \end{bmatrix}. \tag{5.50}$$

Post- and pre-multiplying the last term in (5.50) by $\begin{bmatrix} \left((I - Z A^{\Psi})^{-1} Z B^{\Psi}\right)^* & I \end{bmatrix}^*$ and its

adjoint, respectively, produce

$$\begin{bmatrix} (I - ZA^{\Psi})^{-1}ZB^{\Psi} \\ I \end{bmatrix}^* \left(\begin{bmatrix} (A^{\Psi})^*Z^* \\ (B^{\Psi})^*Z^* \end{bmatrix} X \begin{bmatrix} (A^{\Psi})^*Z^* \\ (B^{\Psi})^*Z^* \end{bmatrix}^* - \begin{bmatrix} X & 0 \\ 0 & 0 \end{bmatrix} \right) \begin{bmatrix} (I - ZA^{\Psi})^{-1}ZB^{\Psi} \\ I \end{bmatrix} = \mathcal{Q}. \tag{5.51}$$

It is clear that (5.51) is equivalently zero; for any $u \in \ell_2$ we define $x = (I - ZA^{\Psi})^{-1}ZB^{\Psi}u \in \ell_2$ to produce the inner product

$$\begin{aligned} \langle u, \mathcal{Q}u \rangle &= \left\langle \begin{bmatrix} x \\ u \end{bmatrix}, \left(\begin{bmatrix} (A^{\Psi})^*Z^* \\ (B^{\Psi})^*Z^* \end{bmatrix} X \begin{bmatrix} ZA^{\Psi} & ZB^{\Psi} \end{bmatrix} - \begin{bmatrix} X & 0 \\ 0 & 0 \end{bmatrix} \right) \begin{bmatrix} x \\ u \end{bmatrix} \right\rangle \\ &= \left\langle \begin{bmatrix} ZA^{\Psi} & ZB^{\Psi} \end{bmatrix} \begin{bmatrix} x \\ u \end{bmatrix}, X \begin{bmatrix} ZA^{\Psi} & ZB^{\Psi} \end{bmatrix} \begin{bmatrix} x \\ u \end{bmatrix} \right\rangle - \langle x, Xx \rangle \\ &= \langle x, Xx \rangle - \langle x, Xx \rangle = 0. \end{aligned}$$

Hence, we have shown that $\bar{\Psi}^*\bar{S}\bar{\Psi} = \Psi^*S\Psi = \Pi$, or that $(\bar{\Psi}, \bar{S})$ are factors of Π. To prove that Ψ^{-1} is a causal node (boundedness is implied by the definition of a causal node), we make mention of the fact that, for a causal node $\mathcal{G} = [A, B, C, D]_+$, if D is boundedly invertible and $A - BD^{-1}C$ is causally stable, then $\mathcal{G}^{-1}$ is a causal node defined by $\mathcal{G}^{-1} = [A - BD^{-1}C, BD^{-1}, -D^{-1}C, D^{-1}]_+$. Per the definition in (5.49), it is clear that $D^{\bar{\Psi}}$ is boundedly invertible. Furthermore, we see that $A^{\Psi} - B^{\Psi}(D^{\bar{\Psi}})^{-1}C^{\bar{\Psi}}$ is causally stable, since

$$-(D^{\bar{\Psi}})^{-1}C^{\bar{\Psi}} = -\left((B^{\Psi})^*Z^*XZB^{\Psi} + R\right)^{-1}\left(L^* + (B^{\Psi})^*Z^*XZA^{\Psi}\right)$$

which is the feedback gain F associated with the stabilizing solution X to the $DDRE(\Psi, S)$. Therefore, $A^{\Psi} - B^{\Psi}(D^{\bar{\Psi}})^{-1}C^{\bar{\Psi}} = A^{\Psi} + B^{\Psi}F$ is causally stable and we may define $\bar{\Psi}^{-1}$ by the causal node $[A^{\Psi} - B^{\Psi}(D^{\bar{\Psi}})^{-1}C^{\bar{\Psi}}, B^{\Psi}(D^{\bar{\Psi}})^{-1}, -(D^{\bar{\Psi}})^{-1}C^{\bar{\Psi}}, (D^{\bar{\Psi}})^{-1}]_+$.

The fact that $\bar{X} = 0$ is a solution to the $DDRE(\bar{\Psi}, \bar{S})$ can be proven by simply substituting $\bar{X}$ into the $DDRE(\bar{\Psi}, \bar{S})$. Defining $\bar{Q} = (C^{\bar{\Psi}})^* \bar{S} C^{\bar{\Psi}}$, $\bar{L} = (C^{\bar{\Psi}})^* \bar{S} D^{\bar{\Psi}}$, and $\bar{R} = (D^{\bar{\Psi}})^* \bar{S} D^{\bar{\Psi}}$, we check the equation defined by the $DDRE(\bar{\Psi}, \bar{S})$ with the candidate solution $\bar{X} = 0$:

$$\begin{aligned} 0 &= \bar{Q} - \bar{L}\bar{R}^{-1}\bar{L}^* \\ &= Q + (A^{\Psi})^* Z^* X Z A^{\Psi} - X - \left(L + (A^{\Psi})^* Z^* X Z B^{\Psi}\right) \\ &\qquad \times \left(R + (B^{\Psi})^* Z^* X Z B^{\Psi}\right)^{-1} \left(L^* + (B^{\Psi})^* Z^* X Z A^{\Psi}\right). \end{aligned}$$

These equations are indeed valid since X is the stabilizing solution to the $DDRE(\Psi, S)$. Finally, $\bar{X} = 0$ is the stabilizing solution to the $DDRE(\bar{\Psi}, \bar{S})$ because the associated feedback operator $\bar{F} = -\bar{R}^{-1}\bar{L}^*$ is equivalent to the feedback operator F for the stabilizing solution X of the $DDRE(\Psi, S)$. □

Proof of Theorem 5.18: Following the approach in [15], first consider the case where Π is a strictly positive-negative multiplier and has factors (Ψ, S). By the hypotheses of Theorem 5.18, $\mathbf{\Delta} \in \mathrm{IQC}(\Pi)$ and there exists a memoryless operator $P = P^*$ such that (5.30) holds. Invoking Lemma 5.22, there is a solution X to the $DDRE(\Psi, S)$, and Π has factors $(\bar{\Psi}, \bar{S})$ such that $\bar{J}^{\bar{\Psi},\bar{S}}(N, \xi) = \underline{J}^{\bar{\Psi},\bar{S}}(N, \xi) = \xi^T \bar{X}(N) \xi = 0$, where $\bar{X}$ satisfies the $DDRE(\bar{\Psi}, \bar{S})$. With $\bar{\Psi} = [A^{\Psi}, B^{\Psi}, C^{\bar{\Psi}}, D^{\bar{\Psi}}]_+$, define the factors $(\bar{\Psi}, \bar{S})$ of Π by (5.48) and (5.49). By Lemma 5.21, $J_T^{\bar{\Psi},\bar{S}}(0, 0, \{\!\!\{\varphi, \Delta(\varphi)\}\!\!\}) \geq 0$ for all $T \in 0_+$, $\varphi \in \ell_{2e}$, $\Delta \in \mathbf{\Delta}$, or in other words, $\mathbf{\Delta} \in \mathrm{HIQC}(\bar{\Psi}, \bar{S})$. By lengthy manipulations, it can be shown that (5.30) is satisfied if and only if

$$\begin{bmatrix} A^{\overline{H}} & B^{\overline{H}} & B^{\overline{H}2} \\ C^{\overline{H}} & D^{\overline{H}} & D^{\overline{H}12} \\ C^{\overline{H}2} & D^{\overline{H}21} & D^{\overline{H}22} \end{bmatrix}^* \begin{bmatrix} Z^* \bar{P} Z & 0 & 0 \\ 0 & \bar{S} & 0 \\ 0 & 0 & I \end{bmatrix} \begin{bmatrix} A^{\overline{H}} & B^{\overline{H}} & B^{\overline{H}2} \\ C^{\overline{H}} & D^{\overline{H}} & D^{\overline{H}12} \\ C^{\overline{H}2} & D^{\overline{H}21} & D^{\overline{H}22} \end{bmatrix} - \begin{bmatrix} \bar{P} & 0 & 0 \\ 0 & 0 & 0 \\ 0 & 0 & \gamma^2 I \end{bmatrix} \preceq -\epsilon I \quad (5.52)$$

where $\bar{P} = P - [0, I]^* X [0, I]$, and all operators $A^\bullet$, $B^\bullet$, $C^\bullet$, and $D^\bullet$ in (5.52) are defined by

(5.27), (5.28), and (5.29) (replacing all instances of H and Ψ with $\overline{H}$ and $\bar{\Psi}$, respectively[†]). With Lemma 5.20, we have $\left[\!\left[\bar{P}\right]\!\right](N) \succeq 0$ for all $N \in 0_+$. Hence, using the factors $(\bar{\Psi}, \bar{S})$ for Π, the hypotheses of Lemma 5.19 are satisfied, providing the conclusion of Theorem 5.18.

Suppose now that Π is non-strictly positive-negative. Because there exists some scalar μ such that $\sup_{\Delta \in \mathbf{\Delta}} \|\Delta\| \leq \mu$, for any $\kappa > 0$ we can construct a strictly positive-negative multiplier

$$\Pi^\kappa = \kappa \begin{bmatrix} \mu^2 I & 0 \\ 0 & -I \end{bmatrix} + \begin{bmatrix} \Pi_{11} & \Pi_{12} \\ \Pi_{12}^* & \Pi_{22} \end{bmatrix} \tag{5.53}$$

such that $\mathbf{\Delta} \in \mathrm{IQC}(\Pi^\kappa)$. Because the LHS of (5.30) is uniformly negative definite, and by redefining the (Ψ, S) to be factors of Π^κ, we can choose κ small enough such that (5.30) holds with the factorization for Π^κ. The same arguments given in the previous paragraph are used to prove Theorem 5.18 for (possibly non-strictly) positive-negative multipliers Π. $\square$

Theorem 5.18 assumes that the disturbance d is any ℓ_2 signal. Though such an assumption is valid for many physical systems, oftentimes more information is known about the disturbance signals, such as certain characteristics in the frequency or time domain. These characteristics can be incorporated with signal IQCs to provide less conservative measures on the robust performance of the uncertain system. We define a *signal IQC multiplier* Φ to be a self-adjoint dichotomic node. Unlike standard IQC multipliers, a signal IQC multiplier is not partitioned.

Definition 5.23. The signal set $\mathcal{D} \subseteq \ell_2$ *satisfies the signal IQC defined by* Φ ($\mathcal{D} \in \mathrm{SigIQC}(\Phi)$) if

$$\langle d, \Phi d \rangle \geq 0, \text{ for all } d \in \mathcal{D}. \tag{5.54}$$

[†]By Lemma 5.22, it is clear that $A^{\bar{\Psi}} = A^{\Psi}$ and $B^{\bar{\Psi}} = B^{\Psi}$. Therefore, $C^{\overline{H}}$, $D^{\overline{H}}$, and $D^{\overline{H}12}$ are the only operators which differ from their "un-barred" counterparts.

Given factors (Θ, U) of Φ, where $\Theta = [A^\Theta, B^\Theta, C^\Theta, D^\Theta]_+$, the set $\mathcal{D}$ *satisfies the soft signal IQC defined by* (Θ, U) ($\mathcal{D} \in \mathrm{SSigIQC}(\Theta, U)$) if

$$J^{\Theta,U}(0, 0, d) \geq 0, \text{ for all } d \in \mathcal{D}. \tag{5.55}$$

The set $\mathcal{D}$ *satisfies the hard signal IQC defined by* (Θ, U) ($\mathcal{D} \in \mathrm{HSigIQC}(\Theta, U)$) if

$$J_T^{\Theta,U}(0, 0, d) \geq 0, \text{ for all } d \in \mathcal{D}, T \in 0_+. \tag{5.56}$$

To incorporate signal IQCs in asserting robust performance, we must define the following memoryless operators:

$$A^{\mathcal{H}} = \begin{bmatrix} A^G & 0 & 0 \\ B^{\Psi 1} C^{G1} & A^\Psi & 0 \\ 0 & 0 & A^\Theta \end{bmatrix}, \qquad B^{\mathcal{H}} = \begin{bmatrix} B^{G1} \\ B^{\Psi 1} D^{G11} + B^{\Psi 2} \\ 0 \end{bmatrix}, \qquad B^{\mathcal{H}2} = \begin{bmatrix} B^{G2} \\ B^{\Psi 1} D^{G12} \\ B^\Theta \end{bmatrix}$$

$$C^{\mathcal{H}} = \begin{bmatrix} D^{\Psi 1} C^{G1} & C^\Psi & 0 \end{bmatrix}, \qquad D^{\mathcal{H}} = D^{\Psi 1} D^{G11} + D^{\Psi 2}, \qquad D^{\mathcal{H}12} = D^{\Psi 1} D^{G12}$$

$$C^{\mathcal{H}2} = \begin{bmatrix} C^{G2} & 0 & 0 \end{bmatrix}, \qquad D^{\mathcal{H}21} = D^{G21}, \qquad D^{\mathcal{H}22} = D^{G22}$$

$$C^{\mathcal{H}3} = \begin{bmatrix} 0 & 0 & C^\Theta \end{bmatrix}, \qquad D^{\mathcal{H}31} = 0, \qquad D^{\mathcal{H}32} = D^\Theta.$$

The following theorem (proven in [50]) provides conditions for determining the robust performance of the uncertain system $(G^{ic}, \mathbf{\Delta})$ where $\mathcal{D}$ may be characterized with signal IQCs.

Theorem 5.24. *Given the partitioned IC node* G^{ic} *defined in* (5.19a)-(5.19b)*, the uncertain system* $(G^{ic}, \mathbf{\Delta})$ *defined by* (5.20) *has a robust* $(\Xi, \mathcal{D})$*-to-*ℓ_2 *gain performance level of* (λ, γ) *if* $(G^{ic}, \mathbf{\Delta})$ *is robustly well-posed and there exist a positive-negative IQC multiplier* Π *with factors* (Ψ, S) *and a signal IQC multiplier* Φ *with factors* (Θ, U) *such that*

(a) $\mathbf{\Delta} \in \mathrm{IQC}(\Pi)$*;*

(b) $\mathcal{D} \in \mathrm{SigIQC}(\Phi)$*;*

(c) there exist $\epsilon > 0$ *and a memoryless operator* $P = P^*$ *satisfying*

$$\begin{bmatrix} A^{\mathcal{H}} & B^{\mathcal{H}} & B^{\mathcal{H}2} \\ C^{\mathcal{H}} & D^{\mathcal{H}} & D^{\mathcal{H}12} \\ C^{\mathcal{H}2} & D^{\mathcal{H}21} & D^{\mathcal{H}22} \\ C^{\mathcal{H}3} & D^{\mathcal{H}31} & D^{\mathcal{H}32} \end{bmatrix}^* \begin{bmatrix} Z^*PZ & 0 & 0 & 0 \\ 0 & S & 0 & 0 \\ 0 & 0 & I & 0 \\ 0 & 0 & 0 & U \end{bmatrix} \begin{bmatrix} A^{\mathcal{H}} & B^{\mathcal{H}} & B^{\mathcal{H}2} \\ C^{\mathcal{H}} & D^{\mathcal{H}} & D^{\mathcal{H}12} \\ C^{\mathcal{H}2} & D^{\mathcal{H}21} & D^{\mathcal{H}22} \\ C^{\mathcal{H}3} & D^{\mathcal{H}31} & D^{\mathcal{H}32} \end{bmatrix} - \begin{bmatrix} P & 0 & 0 \\ 0 & 0 & 0 \\ 0 & 0 & \gamma^2 I \end{bmatrix} \preceq -\epsilon I \quad (5.57)$$

and (5.31).

Remark 5.25. The volume of the ellipsoid $\mathcal{E}(\Xi)$ is proportional to $\det(\Xi^{-\frac{1}{2}})$. Hence, both λ can be made arbitrarily small and the constraint (5.31) arbitrarily unrestrictive by setting the eigenvalues of Ξ to be arbitrarily large (thereby defining the ellipsoid $\mathcal{E}(\Xi)$ to be arbitrarily small). Measuring the robust $\mathcal{D}$-to-ℓ_2 gain performance level of $(G, \mathbf{\Delta})$ can be done by ensuring all the hypotheses of Theorem 5.24 except the constraint (5.31) hold.

While Theorem 5.24 can be used when G^{ic} is an arbitrary IC node and Π and Φ are arbitrary dichotomic nodes, if each node is (h, q)-eventually periodic, we can check the robust performance of $(G^{ic}, \mathbf{\Delta})$ by solving a semidefinite program (SDP).

Corollary 5.26. *Given an* (h_G, q_G)*-eventually periodic* G^{ic} *defined by* (5.19a)-(5.19b)*, the uncertain system* $(G^{ic}, \mathbf{\Delta})$ *defined by* (5.20) *has a robust* $(\Xi, \mathcal{D})$*-to-*ℓ_2 *gain performance level of* (λ, γ) *if* $(G^{ic}, \mathbf{\Delta})$ *is robustly well-posed and there exist a positive-negative IQC multiplier* Π *with* (h_Π, q_Π)*-eventually periodic factors* (Ψ, S) *and a signal IQC multiplier* Φ *with* (h_Φ, q_Φ)*-eventually periodic factors* (Θ, U) *such that*

(a) $\mathbf{\Delta} \in \mathrm{IQC}(\Pi)$*;*

(b) $\mathcal{D} \in \mathrm{SigIQC}(\Phi)$*;*

(c) there exist an $\epsilon > 0$ *and a finite sequence of symmetric matrices* $(P(k))_{k\in[0,h+q]}$ *with* $P(h+q) = P(h)$ *such that, for all* $k \in \{0, 1, \ldots, h+q-1\}$*,*

$$\mathcal{H}(k)^T \mathcal{X}(k) \mathcal{H}(k) - \mathrm{diag}(P(k), 0, \gamma^2 I) \preceq -\epsilon I \tag{5.58}$$

$$\text{where } \mathcal{H}(k) = \begin{bmatrix} A^{\mathcal{H}}(k) & B^{\mathcal{H}}(k) & B^{\mathcal{H}2}(k) \\ C^{\mathcal{H}}(k) & D^{\mathcal{H}}(k) & D^{\mathcal{H}12}(k) \\ C^{\mathcal{H}2}(k) & D^{\mathcal{H}21}(k) & D^{\mathcal{H}22}(k) \\ C^{\mathcal{H}3}(k) & D^{\mathcal{H}31}(k) & D^{\mathcal{H}32}(k) \end{bmatrix}, \quad \mathcal{X}(k) = \begin{bmatrix} P(k+1) & 0 & 0 & 0 \\ 0 & S(k) & 0 & 0 \\ 0 & 0 & I & 0 \\ 0 & 0 & 0 & U(k) \end{bmatrix} \tag{5.59}$$

$h = \max(h_G, h_\Pi, h_\Phi)$*, and* q *is the least common multiple of* q_G, q_Π*, and* q_Φ

$$\text{and } \begin{bmatrix} I_{n_G} & 0 \end{bmatrix} P(0) \begin{bmatrix} I_{n_G} & 0 \end{bmatrix}^T \preceq \lambda^2 \Xi. \tag{5.60}$$

Utilizing Corollary 5.26 to measure the robust performance of $(G^{ic}, \mathbf{\Delta})$ amounts to defining a priori the causal nodes Ψ and Θ and solving an SDP for $P(k)$, $S(k)$, $U(k)$, γ^2 and λ^2 such that (5.58) and (5.60) are satisfied. When the initial condition of G is zero, robust performance reduces to the robust $\mathcal{D}$-to-ℓ_2 gain performance level, and γ^2 can be minimized to determine the lowest robust $\mathcal{D}$-to-ℓ_2 gain performance level which IQC analysis can provide. However, by incorporating uncertain initial conditions and attempting to minimize λ^2, the associated SDP becomes a vector optimization problem.

A natural question to Corollary 5.26 is if the search for (h, q)-eventually periodic symmetric matrix sequences $P(k)$, $S(k)$, and $U(k)$ satisfying (5.58) produces needlessly conservative results. The following two lemmas indicate that the answer is negative; if there are arbitrary symmetric matrix sequences $P(k)$, $S(k)$, and $U(k)$ satisfying (5.58), then there are also (h, q)-eventually periodic symmetric matrix sequences satisfying (5.58).

Lemma 5.27. *Given a q-periodic sequence of matrices $\mathcal{H}$ defined by* (5.59)*, there exist symmetric matrix sequences $P(k)$, $S(k)$, $U(k)$ bounded above and below which satisfy the LMI* (5.58) *for all $k \in 0_+$ if and only if there exist q-periodic symmetric matrix sequences $P_q(k)$, $S_q(k)$, $U_q(k)$ that satisfy* (5.58) *for all $k \in 0_+$.*

Proof. The proof of the 'if' direction is immediate. We now prove the 'only if' direction by constructing q-periodic solutions $P_q(k)$, $S_q(k)$, $U_q(k)$ from $P(k)$, $S(k)$, $U(k)$, respectively. Define $P_N(k) := \frac{1}{N}\sum_{i=0}^{N-1} P(k+iq)$ and $U_N(k)$ and $S_N(k)$ in like manner. In the following arguments, we hold k fixed for $P_N(k)$ and formulate a sequence $P_N(k)$ by incrementing N. Because $P(k)$ is bounded, the sequence $P_N(k)$ is bounded, implying that there exists a subsequence $P_M(k)$ of $P_N(k)$ that weakly converges to a matrix we shall call $\mathbf{P}(k)$ [90,92,94]. We can likewise define $\mathbf{S}(k)$ and $\mathbf{U}(k)$. If $\mathcal{H}(k)$ is q-periodic and (5.58) holds, then

$$\mathcal{H}(k)^T \mathrm{diag}\left(P_M(k+1), S_M(k), I, U_M(k)\right) \mathcal{H}(k) - \mathrm{diag}\left(P_M(k), 0, \gamma^2 I\right) \preceq -\epsilon I \tag{5.61}$$

holds for all $k \in 0_+$. Noting that

$$P_M(k+q) - P_M(k) = \frac{1}{M}(P(k+Mq) - P(k)) \tag{5.62}$$

we have $\lim_{M\to\infty}[P_M(k+q) - P_M(k)] = 0$. By weak convergence, this implies that $\mathbf{P}(k+q) = \mathbf{P}(k)$, or in other words, $\mathbf{P}(k)$ is q-periodic. With similar arguments we conclude that $\mathbf{S}(k)$ and $\mathbf{U}(k)$ are also q-periodic. Finally, taking the limit as M approaches infinity for (5.61), we see that

$$\mathcal{H}(k)^T \mathrm{diag}(\mathbf{P}(k+1), \mathbf{S}(k), I, \mathbf{U}(k)) \mathcal{H}(k) - \mathrm{diag}(\mathbf{P}(k), 0, \gamma^2 I) \preceq -\epsilon I \tag{5.63}$$

holds for all $k \in 0_+$. □

Lemma 5.28. *Given an (h,q)-eventually periodic sequence of matrices $\mathcal{H}$ defined by* (5.59)*, there exist symmetric matrix sequences $P(k)$, $S(k)$, $U(k)$ which satisfy the LMI* (5.58) *for all $k \in 0_+$ if and only if there exist (h,q)-eventually periodic symmetric matrix sequences $P_{h,q}(k)$, $S_{h,q}(k)$, $U_{h,q}(k)$ that satisfy* (5.58) *for all $k \in 0_+$.*

Proof. We just need to prove the 'only if' direction. The proof is very similar to that of a counterpart result given in [95]. To start, suppose that the sequences of symmetric matrices $P(k)$, $S(k)$, $U(k)$ satisfy (5.58) for all $k \in 0_+$, which is conveniently rewritten as

$$\begin{bmatrix} A^{\mathcal{H}}(k) & \tilde{B}(k) \\ \tilde{C}(k) & \tilde{D}(k) \end{bmatrix}^T \begin{bmatrix} P(k+1) & 0 \\ 0 & \tilde{S}(k) \end{bmatrix} \begin{bmatrix} A^{\mathcal{H}}(k) & \tilde{B}(k) \\ \tilde{C}(k) & \tilde{D}(k) \end{bmatrix} - \begin{bmatrix} P(k) & 0 \\ 0 & \Gamma \end{bmatrix} \preceq -\epsilon I \tag{5.64}$$

$$\text{where } \tilde{C}(k) = \begin{bmatrix} C^{\mathcal{H}}(k) \\ C^{\mathcal{H}2}(k) \\ C^{\mathcal{H}3}(k) \end{bmatrix}, \ \tilde{D}(k) = \begin{bmatrix} D^{\mathcal{H}}(k) & D^{\mathcal{H}12}(k) \\ D^{\mathcal{H}21}(k) & D^{\mathcal{H}}22(k) \\ D^{\mathcal{H}31}(k) & D^{\mathcal{H}32}(k) \end{bmatrix}, \quad \begin{array}{l} \tilde{S}(k) = \operatorname{diag}(S(k), I, U(k)) \\ \Gamma = \operatorname{diag}(0, \gamma^2 I), \text{ and} \\ \tilde{B}(k) = \begin{bmatrix} B^{\mathcal{H}}(k) & B^{\mathcal{H}2}(k) \end{bmatrix}. \end{array}$$

By making use of the continuity and convexity properties of LMIs, along with Lemma 5.27, we can apply the same argument as that used in the proof of [95, Lemma 7] to construct (N,q)-eventually periodic symmetric matrix sequences $P_{N,q}(k)$ and $\tilde{S}_{N,q}(k)$ satisfying (5.58) for all $k \in 0_+$. The next step in the proof is to show that (h,q)-eventually periodic solutions $P_{h,q}(k)$ and $\tilde{S}_{h,q}(k)$ can be obtained from $P_{N,q}(k)$ and $\tilde{S}_{N,q}(k)$. To do this, counterpart versions of the technical machinery given in [95, Section 4.2] have to be developed to work with the LMIs in (5.58). For instance, the counterpart versions of the sets $\mathbb{D}_k$ and mappings Ω_k, defined in [95, Section 4.2], will be as follows in our case:

$$\mathbb{D}_k := \{P \in \mathbb{S}^n | \tilde{B}(k)^T P \tilde{B}(k) + \tilde{D}(k)^T \tilde{S}(k) \tilde{D}(k) - \Gamma \prec 0\}$$

$\Omega_k : \mathbb{D}_k \to \mathbb{S}^n$ where

$$\Omega_k(P) := A^{\mathcal{H}}(k)^T P A^{\mathcal{H}}(k) + \tilde{C}(k)^T \tilde{S}(k) \tilde{C}(k) - \left(A^{\mathcal{H}}(k)^T P \tilde{B}(k) + \tilde{C}(k)^T \tilde{S}(k) \tilde{D}(k) \right) \times \left(\tilde{B}(k)^T P \tilde{B}(k) + \tilde{D}(k)^T \tilde{S}(k) \tilde{D}(k) - \Gamma \right)^{-1} \left(\tilde{B}(k)^T P A^{\mathcal{H}}(k) + \tilde{D}(k)^T \tilde{S}(k) \tilde{C}(k) \right).$$

The set $\hat{\mathbb{D}}$ and mapping $\hat{\Omega} : \hat{\mathbb{D}} \to \mathbb{S}^n$ can also be defined in the same manner as performed in [95, Section 4.2]. We note that our definitions of $\mathbb{D}_k$, $\hat{\mathbb{D}}$, Ω_k, and $\hat{\Omega}$ are dependent on the solution sequence $\tilde{S}(k)$, which differ from the definitions in [95, Section 4.2]. To clearly demonstrate the parallels with [95], our symbols do not explicitly display the dependence of these sets and mappings on $\tilde{S}(k)$, though such dependence is evident by the definitions. By applying the Schur complement formula to (5.64), we obtain $P(k+1) \in \mathbb{D}_k$ and $\Omega_k(P(k+1)) \prec P(k)$. Following a similar argument to that in the proof of [95, Proposition 8], we can show that if $P_1 \in \mathbb{S}^n$, $P_2 \in \mathbb{D}_k$, and $P_1 \preceq P_2$, then $P_1 \in \mathbb{D}_k$ and $\Omega_k(P_1) \preceq \Omega_k(P_2)$. Given this result, counterpart versions of [95, Corollary 10] and [95, Corollary 11] can be stated and applied for the solutions $P_{N,q}(k)$ and $\tilde{S}_{N,q}(k)$ of (5.64). Finally, the argument in the proof of [95, Theorem 12] may be applied with the modified LMIs in (5.64) to construct an (h,q)-eventually periodic solution $P_{h,q}(k)$ from $P_{N,q}(k)$. Alternatively, the existence of an (h,q)-eventually periodic solution can be shown using LMI tools stemming from SDP duality theory, following arguments similar to the ones used in [96].

Up to this point, we have indicated that, given an (h,q)-eventually periodic matrix $\mathcal{H}(k)$, there exists an (h,q)-eventually periodic solution $P_{h,q}(k)$ and an (N,q)-eventually periodic solution $\tilde{S}_{N,q}(k)$ such that (5.64) holds for all $k \in 0_+$. In other words, we have:

$$\mathcal{H}(0)^T \begin{bmatrix} P_{h,q}(1) & 0 \\ 0 & \tilde{S}_{N,q}(0) \end{bmatrix} \mathcal{H}(0) - \begin{bmatrix} P_{h,q}(0) & 0 \\ 0 & \Gamma \end{bmatrix} \preceq -\epsilon I$$

$$\vdots$$

$$\mathcal{H}(h)^T \begin{bmatrix} P_{h,q}(h+1) & 0 \\ 0 & \tilde{S}_{N,q}(h) \end{bmatrix} \mathcal{H}(h) - \begin{bmatrix} P_{h,q}(h) & 0 \\ 0 & \Gamma \end{bmatrix} \preceq -\epsilon I$$

$$\vdots$$

$$\mathcal{H}(h+q-1)^T \begin{bmatrix} P_{h,q}(h) & 0 \\ 0 & \tilde{S}_{N,q}(h+q-1) \end{bmatrix} \mathcal{H}(h+q-1) - \begin{bmatrix} P_{h,q}(h+q-1) & 0 \\ 0 & \Gamma \end{bmatrix} \preceq -\epsilon I$$

$$\mathcal{H}(h)^T \begin{bmatrix} P_{h,q}(h+1) & 0 \\ 0 & \tilde{S}_{N,q}(h+q) \end{bmatrix} \mathcal{H}(h) - \begin{bmatrix} P_{h,q}(h) & 0 \\ 0 & \Gamma \end{bmatrix} \preceq -\epsilon I$$

$$\vdots$$

$$\mathcal{H}(h+q-1)^T \begin{bmatrix} P_{h,q}(h) & 0 \\ 0 & \tilde{S}_{N,q}(N-1) \end{bmatrix} \mathcal{H}(h+q-1) - \begin{bmatrix} P_{h,q}(h+q-1) & 0 \\ 0 & \Gamma \end{bmatrix} \preceq -\epsilon I$$

$$\mathcal{H}(h)^T \begin{bmatrix} P_{h,q}(h+1) & 0 \\ 0 & \tilde{S}_{N,q}(N) \end{bmatrix} \mathcal{H}(h) - \begin{bmatrix} P_{h,q}(h) & 0 \\ 0 & \Gamma \end{bmatrix} \preceq -\epsilon I$$

$$\vdots$$

$$\mathcal{H}(h+q-1)^T \begin{bmatrix} P_{h,q}(h) & 0 \\ 0 & \tilde{S}_{N,q}(N+q-1) \end{bmatrix} \mathcal{H}(h+q-1) - \begin{bmatrix} P_{h,q}(h+q-1) & 0 \\ 0 & \Gamma \end{bmatrix} \preceq -\epsilon I$$

$$\mathcal{H}(h)^T \begin{bmatrix} P_{h,q}(h+1) & 0 \\ 0 & \tilde{S}_{N,q}(N) \end{bmatrix} \mathcal{H}(h) - \begin{bmatrix} P_{h,q}(h) & 0 \\ 0 & \Gamma \end{bmatrix} \preceq -\epsilon I$$

$$\vdots$$

which implies that (h, q)-eventually periodic symmetric matrix sequences $P_{h,q}(k)$ and $\tilde{S}_{h,q}(k)$ satisfy (5.64) for all $k \in 0_+$, where

$$\tilde{S}_{h,q}(k) = \begin{cases} \tilde{S}_{N,q}(k), & k < h \\ \tilde{S}_{N,q}(N+k-h), & k \geq h. \end{cases} \tag{5.65}$$

Hence, there is always a manner to construct (h,q)-eventually periodic symmetric matrix sequences $P_{h,q}(k)$, $S_{h,q}(k)$, and $U_{h,q}(k)$ from the solutions $P(k)$, $S(k)$, and $U(k)$ (respectively) such that (5.58) holds. We note that the creation of $\tilde{S}_{h,q}(k)$ from $\tilde{S}_{N,q}(k)$ in (5.65) is defined more simply than the construction of $P_{h,q}(k)$ from $P_{N,q}(k)$. This is because there is no temporal coupling of $\tilde{S}(k)$ in the sequence of LMIs (5.64), whereas $P(k)$ does induce such a coupling in the sequence of LMIs. □

5.3 Time-varying IQC multipliers

By defining Π as a dichotomic node, much more freedom can be given in parameterizing appropriate IQCs. The standard LTI IQC multipliers are obviously captured by dichotomic nodes, along with a variety of *time-varying* multipliers. This section briefly presents a number of time-varying IQCs which either extend the original definition based on LTI multipliers or introduce novel characterizations for sets with time-varying characteristics.

5.3.1 Time-varying, arbitrarily fast scalar uncertainties

Consider the set of memoryless operators Δ, where $|\Delta(k)| \leq \alpha(k) \in \mathbb{R}_+$. Then $\mathbf{\Delta} \in \mathrm{IQC}(\Pi)$ for all memoryless Π where

$$\Pi(k) = \begin{bmatrix} \alpha(k)^2 X(k) & Y(k) \\ Y(k)^T & -X(k) \end{bmatrix}, \quad \begin{matrix} X(k) = X(k)^T \succeq 0 \\ Y(k) = -Y(k)^T. \end{matrix}$$

5.3.2 Time-varying, rate-bounded scalar uncertainties

Consider the set of memoryless operators Δ, where $\Delta(k) = \delta(k)I$, $|\delta(k)| \leq \alpha(k) \in \mathbb{R}_+$ and $|\delta(k+1) - \delta(k)| \leq \beta(k) \in \mathbb{R}_+$. Robustness analysis for $(G^{ic}, \mathbf{\Delta})$ can be performed by constructing an extended nominal system G_e^{ic} and extended uncertainty set $\mathbf{\Delta}_e$ and conducting robustness analysis on $(G_e^{ic}, \mathbf{\Delta}_e)$ (see [97]). In this approach, $\mathbf{\Delta_e} \in \text{IQC}(\Pi)$, where

$$\Delta_e = \begin{bmatrix} \Delta \\ (Z^*\Delta Z - \Delta)[A^\Psi, B^\Psi, A^\Psi, B^\Psi]_+ \end{bmatrix}, \ \Pi = \Psi^* S \Psi$$

$$\Psi = \left[\begin{bmatrix} A^\Psi & 0 \\ 0 & A^\Psi \end{bmatrix}, \begin{bmatrix} B^\Psi & 0 & 0 \\ 0 & B^\Psi & I \end{bmatrix}, \begin{bmatrix} C^\Psi & 0 \\ A^\Psi & 0 \\ 0 & C^\Psi \\ 0 & 0 \end{bmatrix}, \begin{bmatrix} D^\Psi & 0 & 0 \\ B^\Psi & 0 & 0 \\ 0 & D^\Psi & 0 \\ 0 & 0 & I \end{bmatrix} \right]_+$$

$$S(k) = \begin{bmatrix} \text{diag}(\alpha^2(k)X(k), \beta^2(k)\bar{X}(k)) & \text{diag}(Y(k), \bar{Y}(k)) \\ \text{diag}(Y(k), \bar{Y}(k))^T & -\text{diag}(X(k), \bar{X}(k) \end{bmatrix}, \begin{matrix} X(k) \succeq 0, \ Y(k) = -Y(k)^T \\ \bar{X}(k) \succeq 0, \ \bar{Y}(k) = -\bar{Y}(k)^T. \end{matrix}$$

These multipliers can characterize uncertainties that transition to/from time-varying and time-invariant parameters. This is especially useful for analyzing systems undergoing transition maneuvers.

5.3.3 Time-varying, sector-bounded uncertainties

Consider the set of memoryless nonlinear operators defined by $(\Delta(\varphi))(k) = \Delta(k)(\varphi(k))$, where $\Delta(k)$ maps $\mathbb{R}$ to $\mathbb{R}$ and satisfies $(\Delta(k)(x) - \alpha(k)x)(\beta(k)x - \Delta(k)(x)) \geq 0 \ \forall x \in \mathbb{R}$, $k \in 0_+$. This condition assumes $\beta \geq 0 \geq \alpha$. Then $\mathbf{\Delta} \in \text{IQC}(\Pi)$ for all memoryless Π defined by

$$\Pi(k) = \begin{bmatrix} -2\alpha(k)\beta(k) & \alpha(k) + \beta(k) \\ \alpha(k) + \beta(k) & -2 \end{bmatrix}.$$

5.3.4 Disturbances with energy restricted to time-intervals

Consider the set of disturbances $d \in \mathcal{D} \subset \ell_2$ that satisfy

$$\|d(k)\|_2 = 0 \text{ for all } k \in \mathbb{I} \subset 0_+.$$

Then $\mathcal{D} \in \text{SigIQC}(\Phi)$ for any memoryless Φ defined by

$$\Phi(k) = \begin{cases} -\rho I, & k \in \mathbb{I} \\ 0, & \text{otherwise} \end{cases}$$

where $\rho > 0$. Such a multiplier mirrors the multiplier which characterizes the energy content of signals in the frequency domain [16]. This time-domain multiplier can be used for systems undergoing periodic trajectories where certain disturbances are present only during specified portions of the trajectory.

5.3.5 Disturbances which increase or decrease

Consider the set of disturbances $d \in \mathcal{D} \subset \ell_2$ that satisfy

$$\|d(\bar{k})\|_2 \leq \|d(\underline{k})\|_2 \text{ for } \bar{k} > \underline{k} \in 0_+. \tag{5.66}$$

Defining the causal node Θ and the memoryless operator U by

$$\Theta = \left[0, I, \begin{bmatrix} I \\ 0 \end{bmatrix}, \begin{bmatrix} 0 \\ I \end{bmatrix} \right]_+, \quad U(k) = \begin{cases} \begin{bmatrix} I & 0 \\ 0 & -I \end{bmatrix}, & k \in \{\underline{k}+1, \underline{k}+2, \ldots, \bar{k}\} \\ 0, & \text{otherwise} \end{cases} \tag{5.67}$$

then $\mathcal{D} \in \text{SigIQC}(\Phi)$ where Φ has factors (Θ, U). The inequality in (5.66) may be reversed by swapping the signs in (5.67). This multiplier has a variety of potential applications. For example, when utilizing extended Kalman filters for unmanned aircraft systems, we oftentimes observe that the error of the state estimate drastically reduces upon receiving GPS measurements and slowly increases until the next GPS measurement.

The multipliers in Sections 5.3.1, 5.3.3, and 5.3.4 are memoryless and define hard IQCs. Hence, we could apply Lemma 5.19, but this would introduce conservatism by requiring $P \succeq 0$. The multiplier in Sections 5.3.2 is dynamic and the pertinent set of uncertainties does not, in general, satisfy the relevant hard IQC.

Though more IQCs based on dichotomic nodes can be expressed, these suffice in demonstrating their utility. Not only can dichotomic multipliers better characterize uncertainties and disturbances with time-varying characteristics, they may also reduce conservatism by providing a greater number of decision variables (e.g., $X(k)$ and $Y(k)$ in the previous subsections). This potential improvement comes at the cost of increasing computational complexity.

Theorem 5.24 directly provides a tool for analysis of uncertain systems with non-zero initial conditions. Signal IQCs also enable the incorporation of uncertain initial conditions. Consider the IC node (5.19a) with the uncertain initial condition $\xi^G \in \mathcal{E}(\Xi)$ and assume, for simplicity, that it is LTI (this assumption can be removed by following the technique in [98]). Incorporating the uncertain initial condition can be done by defining the causal node

$$\tilde{G} = \left[A^G, \begin{bmatrix} B^{G1} & B^{G2} & B^{G\xi} \end{bmatrix}, \begin{bmatrix} C^{G1} \\ C^{G2} \end{bmatrix}, \begin{bmatrix} D^{G11} & D^{G12} & 0 \\ D^{G21} & D^{G22} & 0 \end{bmatrix} \right]_+$$

where $B^{G\xi}(k) = \mathcal{B}^{G\xi} \in \mathbb{R}^{n_G \times n_G}$ and $\mathcal{B}^{G\xi}\mathcal{B}^{G\xi} = \Xi^{-1}$. Hence, $(\tilde{G}, \boldsymbol{\Delta})$ is disturbed by an additional signal d_ξ, which represents the uncertain initial condition. By assuming $\|d_\xi\|_{\ell_2} \leq 1$

and using signal IQCs to restrict the support of d_ξ and d to 1_- and 1_+, respectively, the robust $\mathcal{D}$-to-ℓ_2 gain performance level γ provides a bound on $\|e\|_{\ell_2}$ in terms of the disturbance d and the system's initial condition. Significantly, such an approach does not directly constrain $[\![P]\!](0)$ as in (5.31), whereas this constraint is enforced in Theorem 5.18, Theorem 5.24, and Corollary 5.26 for asserting the robust $(\Xi, \mathcal{D})$-to-ℓ_2 performance level of $(G^{ic}, \mathbf{\Delta})$. Another method of incorporating the effect of the uncertain initial condition for LTI systems relies on utilizing the signal IQC introduced in [17] for characterizing the output of autonomous systems.

5.4 Applications of IQC theorem

5.4.1 Bounds on the UAS state after a Split-S maneuver

We will apply Corollary 5.26 to analyze a UAS flight controller. In modeling the UAS we mostly follow the derivations given in Chapter 3, except that the vehicle of interest is a Hobby Express 6-foot Junior Telemaster [99]. As this example was developed previous to the work in Chapter 3, not all the uncertainties described therein are included in this section. A diagram of the UAS with exogenous disturbances and uncertainties in red is shown in Figure 5.3. Though the coefficients and constants differ from those in Chapter 3, the UAS model is structured as in (2.7).

Trajectory, Linearization, and Controller

The trajectory considered is a Split-S maneuver. It is obtained by manually flying a Split-S multiple times and recording the control histories of each flight. The average of these control histories is then commanded to a simulated UAS initially at straight-and-level trim.

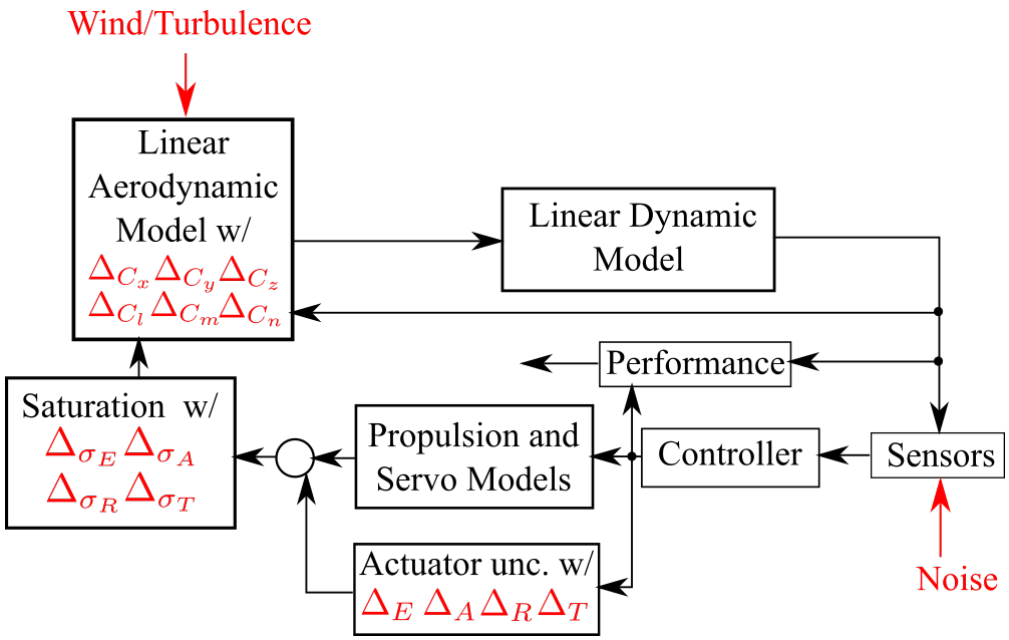

Figure 5.3: UAS model and uncertainties

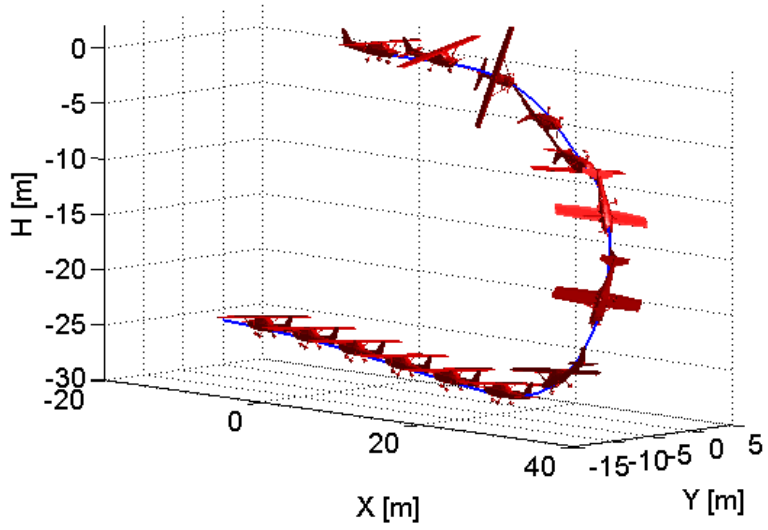

Figure 5.4: Split-S trajectory (graphic credit [2])

	C_x	C_y	C_z	C_l	C_m	C_n
$\Delta^-_{(\cdot)}$	-9E-3	-1E-2	-4E-2	-5E-3	-2E-2	-2E-3
$\Delta^+_{(\cdot)}$	7E-3	1E-2	4E-2	5E-3	2E-2	2E-3
$\nu^-_{(\cdot)}$	-1E-2	-2E-2	-5E-2	-5E-3	-3E-2	-4E-3
$\nu^+_{(\cdot)}$	1E-2	9E-3	5E-2	5E-3	2E-2	2E-3

Table 5.1: Aerodynamic coefficient error bounds

The resulting state trajectory $x^\star$ with its command history $u^\star$ then becomes the trajectory about which the UAS is linearized and discretized to form the open-loop plant. Using a sampling time of 0.05 seconds, the total trajectory occurs in 6 seconds, or 119 timesteps, that is $k \in [0, 119]$. The error state and error command are $\bar{x} = x - x^\star$ and $\bar{u} = u - u^\star$. Following ℓ_2-induced norm controller design methods [59, 100], the performance output

$$e = \left[0.1\bar{p}_b, 0.1\bar{q}_b, 0.1\bar{r}_b, 0.03\bar{u}_b, 0.4\bar{\phi}, 0.4\bar{\theta}, 0.4\bar{\psi}, 0.03\bar{X}, 0.03\bar{Y}, 0.03\bar{h}, 0.4\bar{\delta}_E, 0.2\bar{\delta}_A, 0.5\bar{\delta}_R, 2\bar{\delta}_T\right]^T$$

is used to synthesize an 18 state finite horizon discrete-time controller with matrices $A^K(k)$, $B^K(k)$, $C^K(k)$, $D^K(k)$ and finite horizon length $h = 120$. Further details on creating the trajectory, linearizing the plant, and synthesizing the controller can be found in [60].

Uncertainties

For this example, we consider aerodynamic uncertainties and actuator uncertainties, both as derived in Chapter 3. The bounds on the actuator uncertainties are the same as previously derived, but since the vehicle under analysis is different from that in Chapter 3, the bounds on the aerodynamic uncertainties are different (see Table 5.1).

It should be observed that the foregoing uncertainties are all linear. IQC theory is capable of addressing nonlinearities, such as passive, norm-bounded, and sector-bounded nonlinearities. Additionally, in order to "recover" the nonlinear system by the LFT representation, there

ought to be model uncertainties in the Linear Dynamic Model (see Figure 5.3). This uncertainty has not yet been introduced for two reasons. First, the complexity of representing each nonlinear term in the 12 equations of motion produces an LFT which has too many states to be computationally tractable. Second, the uncertainties are initially introduced in the continuous-time dynamic equations, and it is a challenge to determine a proper discretization technique which sufficiently preserves the behavior of the continuous-time time-varying model while formulating an LFT which is not overly complex and intractable. The work in Chapters 3 and 4 for LTI systems is not challenged by the second point, and includes linear perturbations in the dynamic model. As this example is simply to illustrate the application of the previous theoretical results, the solution to these issues can be addressed in work dedicated to formulating the uncertain UAS framework.

Results

Analysis of the UAS is done where performance output is chosen as

$$e(k) = \begin{cases} 0, & k < 119 \\ \left[\bar{X}(k), \bar{Y}(k), \bar{h}(k)\right]^T, & k = 119. \end{cases} \tag{5.68}$$

Note that the performance output chosen for analysis is different from the one used in the controller synthesis. The resulting γ^2 obtained from applying Corollary 5.26 to the UAS model with actuator and aerodynamic uncertainties then serves as a scaling factor between the energy of the disturbance input d truncated at $k = 119$ and the radius squared of the Euclidean ball in which the final error in position resides. YALMIP/Mosek [74, 75] is used with MATLAB to find the optimal γ, the solution sequence $P(k)$, and matrix $S(k) = S$ that satisfy the LMI in Corollary 5.26. In this example, we consider the intial condition of the UAS to be zero, thereby removing the necessity to enforce (5.31) when applying Corollary

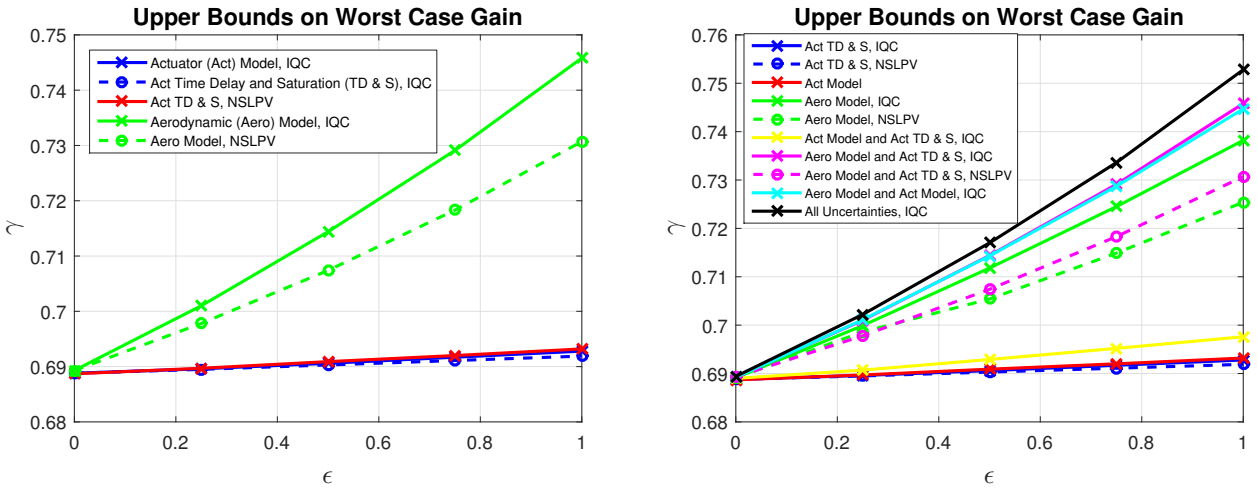

Figure 5.5: Upper bounds on worst-case performance under different combinations of uncertainties

5.26.

Figure 5.5 shows the effects of different combinations of the considered uncertainties on the worst-case performance. Specifically, for a group of uncertainties, say, the six SLTV perturbations that appear in the aerodynamic model, Corollary 5.26 is applied to the interconnection $(G, \epsilon\Delta)$ for $\epsilon = 0, 0.25, 0.5, 0.75, 1$. Additional analyses for upper bounds are conducted on uncertainty groups that are entirely SLTV. For such uncertainty groups, an analysis result on nonstationary linear parameter-varying (NSLPV) systems [101] is employed to determine the conservativeness of the IQC analysis.

A number of simulations are also carried out to further clarify the usefulness of the bound γ. In these simulations, the DLTI and SLTV perturbations are pseudo-randomly generated using the MATLAB commands `drss` and `rand`, respectively, along with appropriate scalings. In total, 20 different Δ blocks are created, and for each Δ block, 60 simulations are performed using 60 different disturbance signals, resulting in 1200 simulations. The truncated disturbance d in these simulations consists of a 2 m/s steady wind, where the wind direction varies between simulations, along with light turbulence generated from the low-altitude

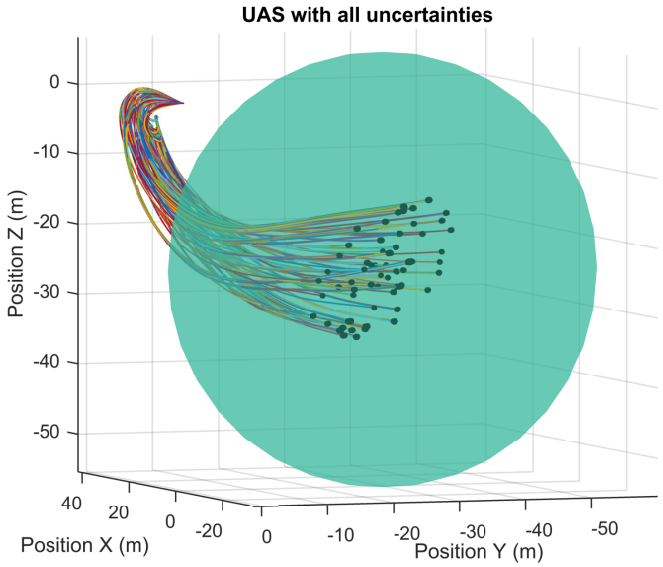

Figure 5.6: Split-S trajectories for all uncertainties

Dryden turbulence model and zero-mean, unit-variance, Gaussian sensor noise across all channels. Given the aforementioned disturbances, the average ℓ_2-norm of d is 41.3. The resulting physical bounds on the final position error range from 28.6 m for the case of no uncertainties to 31.1 m when all uncertainties are considered. A sample of the most deviant trajectories is displayed in Figure 5.6, along with the guaranteed ball where the UAS will finally reside.

The immediate observation of these results is that the UAS model is most sensitive to aerodynamic uncertainties. Indeed, the performance degradation from both actuator uncertainties was only 1.3%, while the performance degradation due to aerodynamic uncertainties was 7.2%. We also see that the resulting physical bounds are rather large, even for the nominal system without uncertainties (in which case the bound is equal to that obtained by applying the standard KYP lemma for LTV systems [90]). This suggests that the designed controller does not provide excellent performance, but is quite robust to the considered uncertainties.

To illustrate this point, another LTV controller (Controller B) is synthesized with the per-

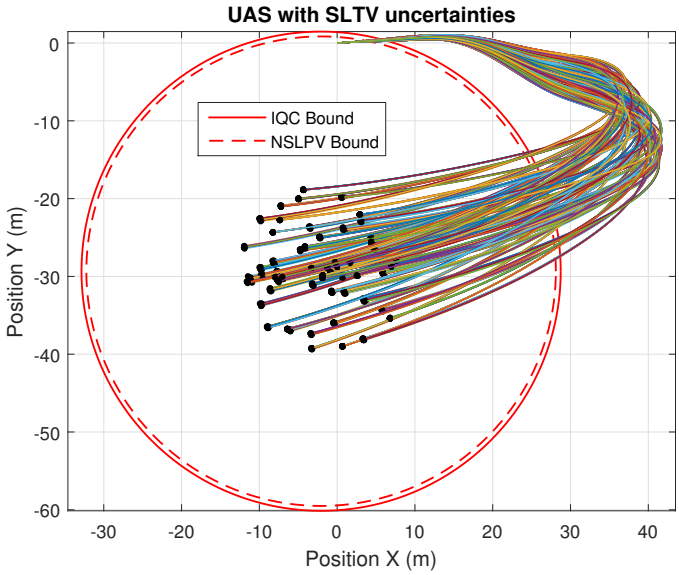

Figure 5.7: Split-S trajectories considering all SLTV uncertainties (Aero Model and Act TD & S)

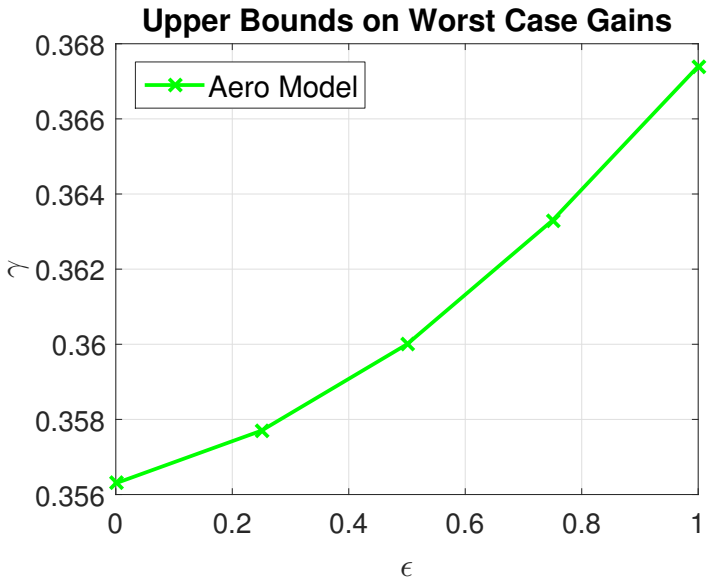

Figure 5.8: Upper bounds on $\|d \mapsto e\|$ for Controller B, which is synthesized based on (5.68)

formance output (5.68). This performance output is precisely the same as the one used in analysis, producing a controller that minimizes the final ball for a system without uncertainties. However, when uncertainties are incorporated, IQC analysis demonstrates that this controller lacks robustness.

Consulting Figure 5.8, it is apparent that the nominal γ for the UAS with Controller B is 52% that of the UAS with the original controller. Additionally, the degradation under aerodynamic uncertainty is 43% that of the degradation for aerodynamic uncertainty with the previous controller. Though this appears to provide better performance, all other uncertainties produce an infeasible problem under IQC analysis. Here we see that Controller B is better for the nominal system, but is not robust to uncertainties. We also see that γ will never be lower than 0.356, as that is the gain for the nominal system with a controller synthesized to minimize the performance output (5.68). With the aforementioned disturbances, this gain produces a bounding sphere of radius 14.7 m. Even in this case, such a bound is still large, and demonstrates that for this system there are inherent sensitivities to disturbances which cannot be mitigated.

Controller B additionally highlights the merits of IQC analysis in addressing performance, robust stability, and robust performance in a unifying theorem. Not only did Controller B fail to produce a feasible problem with all uncertainties (aside from aerodynamic uncertainties) for robust performance, but the closed-loop system did not pose a feasible problem in testing for robust *stability*. In other words, Controller B demonstrated excellent robust performance for aerodynamic uncertainties, but IQC analysis could not conclude that mere robust stability existed in the presence of actuator uncertainties. From a numerical standpoint, it is also possible to obtain a performance level γ for the nominal system with IQC theory by scaling the LFT's uncertainties to a negligible size and applying Corollary 5.26. The results shown here for $\epsilon = 0$ are obtained by this manner, and correspond with the γ obtained when

applying the KYP Lemma for nominal LTV systems [90, 95].

Note that the bounds obtained from applying the NSLPV analysis result from [101] are less than those from IQC analysis. It may be even possible to further reduce these bounds by employing the NSLPV analysis result that appears in [102, 103], which is based on a parameter-dependent Lyapunov approach and takes into account the bounds on the rates of variation of the SLTV uncertainties. These observations demonstrate the complementary fashion of different analysis tools. Though the NSLPV result used herein is less conservative when analyzing SLTV uncertainties, it cannot be used for analyzing other uncertainties. However, the IQC approach can analyze systems with diverse uncertainties, and there is a mature library of IQC multipliers which describe many types of perturbations.

Finally, these problems have large computational demands. This issue needs to be addressed in future work, where model reduction or exploiting the structure of the LMIs needs to be investigated. Reducing computational demands may also help in lowering the IQC bounds by allowing the use of longer basis functions in describing Π. As an illustrative example, this system demonstrates a useful application of Corollary 5.26 and reveals the benefits and challenges to IQC analysis on large and complicated systems.

5.4.2 An inverted pendulum

Consider a telescoping pendulum executing a controlled maneuver from its horizontal position (i.e., the pendulum angle $\eta = -\pi/2$) to its inverted position ($\eta = 0$). The pendulum's dynamics are expressed by

$$\ddot{\eta}(t) = \frac{g \sin \eta(t)}{l(t)} + \frac{1}{ml^2(t)} \tau_c(t) \tag{5.69}$$

where $g = 9.81\text{m/s}^2$, $m = 2\text{kg}$, and τ_c are the gravitational acceleration, the pendulum's mass, and the controlling torque, respectively. The pendulum's length ($l(t) = l_c + \bar{l}(t)$) has a constant term $l_c = 0.5\text{m}$ and a time-varying uncertainty $\bar{l}(t) \in [-0.17, 0.17]\text{m}$. The trajectory we wish to execute is

$$\eta_r(t) = \begin{cases} \dfrac{3\pi}{\kappa^2}\left(\dfrac{t^2}{2} - \dfrac{t^3}{3\kappa}\right) - \dfrac{\pi}{2}, & t < \kappa \\ 0, & t \geq \kappa \end{cases} \tag{5.70}$$

for some $\kappa > 0$. This trajectory is selected because $\eta_r(0) = -\dfrac{\pi}{2}$, $\eta_r(\kappa) = 0$, and $\dot{\eta}_r(0) = \dot{\eta}_r(\kappa) = 0$. The remaining reference signals $\dot{\eta}_r$ and τ_r^c can be easily obtained by appealing to (5.70) and (5.69). We now linearize (5.69) with respect to the reference trajectory (5.70), producing the following linear equation which approximates the error dynamics:

$$\dot{\bar{x}}_c(t) = \overbrace{\begin{bmatrix} 0 & 1 \\ \dfrac{g}{l_c + \bar{l}(t)}\cos\eta_r(t) & 0 \end{bmatrix}}^{A_c(\bar{l}(t),t)} \bar{x}_c(t) + \overbrace{\begin{bmatrix} 0 \\ \dfrac{1}{m(l_c + \bar{l}_c(t))^2} \end{bmatrix}}^{B_c^2(\bar{l}(t))} \bar{\tau}_c(t).$$

The previous equation can be expressed in the LFT form

$$\begin{bmatrix} \dot{\bar{x}}_c(t) \\ \varphi_c(t) \end{bmatrix} = \begin{bmatrix} A_c^{ss}(t) & A_c^{sp}(t) & B_c^{2s} \\ A_c^{ps} & A_c^{pp} & B_c^{2p} \end{bmatrix} \begin{bmatrix} \bar{x}_c(t) \\ \vartheta_c(t) \\ \bar{\tau}_c(t) \end{bmatrix}, \quad \vartheta_c(t) = \bar{l}_c(t)\varphi_c(t)$$

which can be discretized by

$$A^{ss}(k) = \Phi_c^{ss}((k+1)T, kT), \qquad A^{sp}(k) = \int_{kT}^{(k+1)T} \Phi_c^{ss}((k+1)T, \sigma) A_c^{sp}(\sigma) d\sigma$$

$$B^{2s}(k) = \int_{kT}^{(k+1)T} \Phi_c^{ss}((k+1)T, \sigma) B_c^{2s} d\sigma, \quad A^{ps}(k) = A_c^{ps},\ A^{pp}(k) = A_c^{pp}, \text{ and } B^{2p}(k) = B_c^{2p}$$

Table 5.2: γ-values for pendulum with uncertain length

Time-invariant	Eventually time-invariant	General time-varying
0.923	3.36	4.39

where $\Phi_c^{ss}(\cdot,\cdot)$ is the continuous-time state transition matrix associated with A_c^{ss} and T is the sampling time. Defining the performance output $e(k) = \bar{x}(k) = \bar{x}_c(kT)$, the sensor output $\bar{y}(k)$ as the pendulum's angle error, and a disturbance torque $d(k)$ which influences the system exactly like the control torque in discrete time $\bar{\tau}(k)$ (i.e., $B_c^{1\bullet} = B_c^{2\bullet}$), we obtain the discrete-time LFT

$$\begin{bmatrix} \bar{x}^+ \\ \varphi \\ e \\ \bar{y} \end{bmatrix} = \begin{bmatrix} A^{ss} & A^{sp} & B^{1s} & B^{2s} \\ A^{ps} & A^{pp} & B^{1p} & B^{2p} \\ C^{1s} & C^{1p} & D^{11} & D^{12} \\ C^{2s} & C^{2p} & D^{21} & 0 \end{bmatrix} \begin{bmatrix} \bar{x} \\ \vartheta \\ d \\ \bar{\tau} \end{bmatrix}, \quad \begin{bmatrix} \bar{x} \\ \varphi \end{bmatrix} = \begin{bmatrix} Z & 0 \\ 0 & \bar{l} \end{bmatrix} \begin{bmatrix} \bar{x}^+ \\ \vartheta \end{bmatrix} \tag{5.71}$$

where all of the operators in the leftmost equation of (5.71) are $(h,1)$-eventually periodic, with h being the integer ceiling of κ/T.

By extracting the nominal system from (5.71), synthesizing an $(h,1)$-eventually periodic controller $K = [A^K, B^K, C^K, D^K]_+$, and closing the loop via the equation $\bar{\tau} = K\bar{y}$, we obtain an LFT mapping $d \mapsto e$:

$$\begin{bmatrix} \bar{x}^+ \\ \varphi \\ e \end{bmatrix} = \begin{bmatrix} \mathcal{A}^{ss} & \mathcal{A}^{sp} & \mathcal{B}^s \\ \mathcal{A}^{ps} & \mathcal{A}^{pp} & \mathcal{B}^p \\ \mathcal{C}^s & \mathcal{C}^p & \mathcal{D} \end{bmatrix} \begin{bmatrix} \bar{x} \\ \vartheta \\ d \end{bmatrix}, \quad \begin{bmatrix} \bar{x} \\ \varphi \end{bmatrix} = \begin{bmatrix} Z & 0 \\ 0 & \bar{l} \end{bmatrix} \begin{bmatrix} \bar{x}^+ \\ \vartheta \end{bmatrix}. \tag{5.72}$$

Up to this point, the behavior of $\bar{l}$ has only been specified as time-varying. In fact, we will

Table 5.3: γ-values for pendulum with uncertain mass

Nominal system	Uncertain mass eventually discarded	General time-varying
0.054	0.42	1.04

conduct IQC analysis where $\bar{l}$ is a rate-bounded time-varying operator. For the first h steps, $|\bar{l}_{k+1} - \bar{l}_k| \leq 0.17$m, but afterwards—once the pendulum is in the inverted position—we have $|\bar{l}_{k+1} - \bar{l}_k| = 0$. In other words, the pendulum no longer telescopes for all $k \geq h$, but its final length remains uncertain. Such phenomena occur in sets of manufacturing robotic arms which have the same control law but need to end at different heights. If we could not take advantage of eventually periodic IQC multipliers, the uncertainty would be conservatively characterized as rate-bounded time-varying whose rate-bounds are constant. This is demonstrated by measuring the robust performance for three different uncertainty characterizations. The first characterization uses the standard IQC multiplier for rate-bounded time-varying uncertainties where the rate β is identically zero, or in other words, $\bar{l}$ is time-invariant. For this case, the value of γ is 0.923. We then characterize $\bar{l}$ with a time-varying multiplier, describing an eventually time-invariant uncertainty. The pertinent γ-value is obtained by applying Corollary 5.26 with the IQC multiplier given in 5.3.2. This value is found to be 3.36. Finally, analysis is conducted when the rate bound is constant, allowing $\bar{l}$ to change in perpetuity. For this case, the γ-value is 4.39. Analysis is done using YALMIP/ MOSEK [74, 75] on MATLAB R2018a. As seen from the preceding, less conservative results can be obtained by more accurately characterizing the eventually time-invariant uncertainty with time-varying IQC multipliers.

We can see the effectiveness of eventually periodic IQC multipliers in another example. Instead of allowing uncertainty in the pendulum's length, allow the pendulum's mass to be time-varying (assuming that the dynamics are still described by the given equations). A

pendulum with time-varying mass may be used to model robotic arms that are required to lift and release various objects having different masses. Suppose the pendulum releases its uncertain mass after a certain point (denoted the time instant $\tilde{h}$) in its trajectory. This behavior can be expressed with the multiplier in 5.3.1, where $\alpha_k = 0$ for all $k > \tilde{h} \in [0, h]$. The benefit of utilizing this multiplier is seen when comparing robust performance results to those for the nominal system and the system with possibly ever-changing uncertain mass (see Table 5.3). We see from Tables 5.2 and 5.3 that the eventually periodic multipliers used to obtain the γ-values in the center columns are greatly improved from those in the rightmost columns. The γ-values from the central columns in both tables required the use of Corollary 5.26.

Chapter 6

Conclusions

In Chapter 3, the IQC-based uncertainty framework proposed in [12] was applied to a 94-in wingspan Senior Telemaster Plus UAS platform. The considered uncertainties were then used to analyze the performance of an $\mathcal{H}_\infty$ controller. A gradient-based minimization algorithm utilizing IQC analysis was implemented to tune a first-cut controller, producing an improved intermediate, then superior final controller. Simulation and flight test data corresponded qualitatively to IQC analysis results and validated the capability of IQC theory in assessing robust performance of the physical UAS while guiding the control design process. Flight test data also demonstrated that robust performance–rather than nominal performance–is a better suited metric in assessing how well the physical system behaves.

In Chapter 4, the original uncertain UAS framework was enriched by incorporating uncertainties in the UAS trim point. This addition allows the application of IQC analysis for level, arbitrarily curved paths whose inverse radius of curvature is bounded. IQC analysis is also used to tune a variety of controllers: path-following or trajectory-tracking, $\mathcal{H}_2$ or $\mathcal{H}_\infty$, and path-following PID controllers. By comparing IQC analysis results, simulations, and flight tests of numerous controllers, it is shown that IQC analysis is a useful tool in predicting controller failures and qualitatively comparing the performance of controllers. It also becomes apparent that the capability to characterize disturbances via IQCs is a powerful tool. This is especially relevant, as signal IQCs are too often ignored in the literature to date. Finally, IQC analysis, simulations, and flight tests provide additional data in affirming the superior

performance of $\mathcal{H}_2$ and $\mathcal{H}_\infty$ controllers over the considered PID controller and path-following controllers over trajectory-tracking ones.

Although the data appears to confirm it, we cautiously refrain from stating that this approach provides a *guaranteed* bound on the physical aircraft performance. Some uncertainties approximate the true characteristics of the aircraft dynamics (such as actuator saturation) but do not express them exactly. Furthermore, the bounds on some uncertainties are derived with an assumed flight envelope of the aircraft, such as the aerodynamic model uncertainties. These aspects prevent this approach from completely characterizing the physical UAS. As it stands, we have found this approach to be a fast, inexpensive, and reliable tool for predicting the physical UAS performance.

Though we do not address software in this work, the control algorithm analyzed herein is a high-level representation of the aircraft flight control software. This framework can provide evidence that certain "functional, performance, and safety-related requirements of the system are satisfied" [4] by the controller. Such evidence ought to *complement*, rather than replace, those provided from more traditional analyses, such as simulation results and gain/phase margins [104].

In Chapter 5, we derived results allowing the general application of time-varying multipliers when conducting IQC analysis for uncertain systems whose nominal system may be time-varying and have non-zero initial conditions. These IQC multipliers belong to the space of *dichotomic nodes*, a time-varying analog to $\mathcal{RL}_\infty$. Furthermore, we have demonstrated how IQC analysis can be conducted by solving a finite set of LMIs when the nominal system and the IQC multiplier are eventually periodic. Multiple time-varying IQC multipliers have been presented. Furthermore, two examples are provided to demonstrate how robust bounds can be generated on the UAS state, and how time-varying IQC multipliers can be used to provide improved robust performance results when time-domain properties of the uncertain system

can be characterized. These results can be extended to allow the application of signal IQCs [50], which enables the use of time-varying signal IQC multipliers. Such multipliers have the capability of expressing many different types of signal sets with time-domain characteristics, opening up new possibilities in the robustness analysis of uncertain UAS.

Bibliography

[1] D. Muniraj, M. Palframan, K. Guthrie, and M. Farhood, "Path-following control of small fixed-wing unmanned aircraft systems with $\mathcal{H}_\infty$ type performance," *Control Engineering Practice*, vol. 67, pp. 76–91, 2017. xi, 5, 55, 56, 77

[2] O. Arifianto and M. Farhood, "Development and modeling of a low-cost unmanned aerial vehicle research platform," *Journal of Intelligent & Robotic Systems*, vol. 80, no. 1, pp. 139–164, 2015. xii, 18, 128

[3] FAA, "AC 20–115D: Airborne software development assurance using EUROCAE ED-12 and RTCA DO-178," Jul. 2017. 1

[4] *Software Considerations in Airborne Systems and Equipment Certification*, RTCA Std. DO–178C, Dec. 2011. 1, 141

[5] Office of the Secretary of Defense, "Unmanned aircraft systems roadmap, 2005–2030," Aug. 2005. 1

[6] *Vehicle Management Systems – Flight Control Function, Design, Installation and Test of Piloted Military Aircraft, General Specification for*, SAE International Std. AS94 900, Rev. A, 2018. 1

[7] *Aerospace – Vehicle Management Systems – Flight Control Design, Installation and Test of, Military Unmanned Aircraft, Specification Guide For*, SAE Aerospace Std. ARP94 910, 2012. 1

[8] C. Belcastro and C. Belcastro, "On the validation of safety critical aircraft systems, part i: An overview of analytical & simulation methods," in *AIAA Guidance, Navigation, and Control Conference and Exhibit*, Austin, TX, 2003. 1

[9] B. L. Stevens, F. L. Lewis, and E. N. Johnson, *Aircraft Control and Simulation: Dynamics, Controls, Design, and Autonomous Systems*, 3rd ed. Hoboken, NJ: John Wiley & Sons, 2016. 2

[10] S. A. Jacklin, "Closing the certification gaps in adaptive flight control software," in *AIAA Guidance, Navigation, and Control Conference and Exhibit*, Honolulu, Hawaii, 2008. 2

[11] A. Megretski and A. Rantzer, "System analysis via integral quadratic constraints," *IEEE Transactions on Automatic Control*, vol. 42, no. 6, pp. 819–830, 1997. 2, 3, 6, 7, 8, 20, 21, 88, 98, 101, 102

[12] M. C. Palframan, "Robust control design and analysis for small fixed-wing unmanned aircraft systems using integral quadratic constraints," Ph.D. dissertation, Virginia Tech, 2016. 2, 4, 5, 26, 35, 140

[13] M. Palframan, J. M. Fry, and M. Farhood, "Robustness analysis of flight controllers for fixed-wing unmanned aircraft systems using integral quadratic constraints," *IEEE Transactions on Control Systems Technology*, vol. 27, no. 1, pp. 86–102, Jan. 2019. 2, 5, 9, 10, 26, 28, 32

[14] J. M. Fry and M. Farhood, "A comprehensive analytical tool for control validation of fixed-wing unmanned aircraft," *IEEE Transactions on Control Systems Technology*, pp. 1–17, 2019, doi: 10.1109/TCST.2019.2923649. 2, 9, 10, 52

[15] P. Seiler, "Stability analysis with dissipation inequalities and integral quadratic constraints," *IEEE Transactions on Automatic Control*, vol. 60, no. 6, pp. 1704–1709, Jun. 2015. 2, 7, 109, 114

[16] A. V. Megretski, "Power distribution approach in robust control," in *Proceedings of the 12th Triennial IFAC World Congress*, Sydney, Australia, 1993, pp. 27–30. 3, 125

[17] U. Jonsson and A. Megretski, "IQC characterizations of signal classes," in *European Control Conference*. IEEE, 1999, pp. 1481–1486. 3, 22, 24, 127

[18] A. Packard and J. Doyle, "The complex structured singular value," *Automatica*, vol. 29, no. 1, pp. 71–109, 1993. 3

[19] G. J. Balas, J. C. Doyle, K. Glover, A. Packard, and R. Smith, *μ–Analysis and Synthesis Toolbox*, Natick, MA, 2001. 3

[20] J. Veenman, C. W. Scherer, and H. Köroğlu, "Robust stability and performance analysis based on integral quadratic constraints," *European Journal of Control*, vol. 31, pp. 1–32, 2016. 3, 20, 22, 98, 102

[21] J.-M. Biannic, C. Roos, and A. Knauf, "Design and robustness analysis of fighter aircraft flight control laws," *European Journal of Control*, vol. 12, no. 1, pp. 71–85, Jan. 2006. 4

[22] J. Veenman, H. Köroğlu, and C. W. Scherer, "Analysis of the controlled NASA HL20 atmospheric re–entry vehicle based on dynamic IQCs," in *AIAA Guidance, Navigation, and Control Conference*, Chicago, IL, 2009. 4, 32

[23] M. J. Siersma, R. Van der Weerd, and S. Bennani, "Robustness analysis of a gain-scheduled flight control system using integral quadratic constraints," in *AIAA Guid-*

ance, Navigation, and Control Conference and Exhibit; Denver, CO, Denver, CO, 2000, pp. 1–11. 4

[24] A. Chakraborty, P. J. Seiler, and G. J. Balas, "Local performance analysis of uncertain polynomial systems with applications to actuator saturation," in *50th IEEE Conference on Decision and Control and European Control Conference*, no. 1, Orlando, Florida, 2011, pp. 8176–8181. 4

[25] F. Demourant, "New algorithmic approach based on integral quadratic constraints for stability analysis of high order models," in *European Control Conference*, Zürich, Switzerland, 2013, pp. 359–364. 4

[26] A. Hjartarson, P. J. Seiler, and G. J. Balas, "LPV robustness analysis of gain scheduled flight control for a aeroelastic aircraft," in *American Control Conference*, Portland, Oregon, 2014. 4

[27] A. Iannelli, A. Marcos, and M. Lowenberg, "Nonlinear robust approaches to study stability and postcritical behavior of an aeroelastic plant," *IEEE Transactions on Control Systems Technology*, vol. 27, no. 2, pp. 703–716, March 2019. 4

[28] C. L. Beck, "Coprime factors reduction methods for linear parameter varying and uncertain systems," *Systems & Control Letters*, vol. 55, no. 3, pp. 199–213, Mar. 2006. 4, 33

[29] I. Kaminer, A. Pascoal, E. Xargay, N. Hovakimyan, C. Cao, and V. Dobrokhodov, "Path following for small unmanned aerial vehicles using L1 adaptive augmentation of commercial autopilots," *Journal of Guidance, Control, and Dynamics*, vol. 33, no. 2, pp. 550–564, 2010. 5, 54, 55

[30] A. P. Aguiar, J. P. Hespanha, and P. V. Kokotović, "Performance limitations in reference tracking and path following for nonlinear systems," *Automatica*, vol. 44, no. 3, pp. 598–610, 2008. 6

[31] U. T. Jönsson, "Lecture notes on integral quadratic constraints," Department of Mathematics, Royal Institute of Technology, Stockholm, Sweden, Tech. Rep. TRITA/MAT-00-OS12, 2001. 6, 20

[32] C.-Y. Kao, A. Megretski, and U. T. Jönsson, "A cutting plane algorithm for robustness analysis of periodically time-varying systems," *IEEE Transactions on Automatic Control*, vol. 46, no. 4, pp. 579–592, 2001. 7

[33] U. T. Jönsson, C.-Y. Kao, and A. Megretski, "Analysis of periodically forced uncertain feedback systems," *IEEE Transactions on Circuits and Systems I: Fundamental Theory and Applications*, vol. 50, no. 2, pp. 244–258, 2003. 7

[34] T. Hagiwara and Y. Ohara, "Noncausal linear periodically time-varying scaling for robust stability analysis of discrete-time systems: Frequency-dependent scaling induced by static separators," *Automatica*, vol. 46, no. 1, pp. 167 – 173, 2010. 7

[35] J. C. Willems, "Dissipative dynamical systems part I: General theory," *Archive for Rational Mechanics and Analysis*, vol. 45, no. 5, pp. 321–351, Jan 1972. 7, 104

[36] ——, "Dissipative dynamical systems part II: Linear systems with quadratic supply rates," *Archive for Rational Mechanics and Analysis*, vol. 45, no. 5, pp. 352–393, Jan 1972. 7, 104

[37] H. Pfifer and P. Seiler, "Robustness analysis of linear parameter varying systems using integral quadratic constraints," *International Journal of Robust and Nonlinear Control*, vol. 25, no. 15, pp. 2843–2864, 2015. 7

[38] J. M. Fry, M. Farhood, and P. Seiler, "IQC-based robustness analysis of discrete-time linear time-varying systems," *International Journal of Robust and Nonlinear Control*, vol. 27, no. 16, pp. 3135–3157, Nov. 2017. 7, 9, 10, 88, 94, 104

[39] J. Veenman and C. W. Scherer, "Stability analysis with integral quadratic constraints: A dissipativity based proof," in *Proc. of the IEEE Conference on Decision and Control*, Florence, Italy, 2013, pp. 3770–3775. 7, 21

[40] H. Pfifer and P. Seiler, "Less conservative robustness analysis of linear parameter varying systems using integral quadratic constraints," *International Journal of Robust and Nonlinear Control*, vol. 26, no. 16, pp. 3580–3594, 2016. 7

[41] B. Hu, M. J. Lacerda, and P. Seiler, "Robustness analysis of uncertain discrete-time systems with dissipation inequalities and integral quadratic constraints," *International Journal of Robust and Nonlinear Control*, vol. 27, no. 11, pp. 1940–1962, 2017. 7, 104

[42] H. Bart, I. Gohberg, M. A. Kaashoek, and A. C. Ran, *A State Space Approach to Canonical Factorization with Applications*, ser. Linear Operators and Linear Systems. Birkhäuser, 2010. 7

[43] J. A. Ball, I. Gohberg, and M. A. Kaashoek, "Nevanlinna-pick interpolation for time-varying input-output maps: The discrete case," in *Time–variant systems and interpolation*, ser. Operator Theory: Advances and Applications. Birkhäuser, 1992. 7

[44] M. Green, K. Glover, D. Limebeer, and J. Doyle, "A J-spectral factorization approach to $\mathcal{H}_\infty$ control," *SIAM Journal on Control and Optimization*, vol. 28, no. 6, pp. 1350–1371, 1990. 7

[45] K.-C. Goh and M. G. Safonov, "Robust analysis, sectors, and quadratic functionals," in *Proceedings of 1995 34th IEEE Conference on Decision and Control*, vol. 2, Dec. 1995, pp. 1988–1993. 7

[46] K.-C. Goh, "Structure and factorization of quadratic constraints for robustness analysis," in *Proceedings of 35th IEEE Conference on Decision and Control*, vol. 4, Dec. 1996, pp. 4649–4654. 7

[47] C. W. Scherer and J. Veenman, "Stability analysis by dynamic dissipation inequalities: On merging frequency–domain techniques with time–domain conditions," *Systems & Control Letters*, vol. 121, pp. 7–15, 2018. 8

[48] A. Halanay and V. Ionescu, *Time–Varying Discrete Linear Systems*. Birkhäuser, 1994, vol. 68. 8, 88, 92, 93, 97, 110, 112

[49] J. M. Fry and M. Farhood, "IQC-based robustness analysis with time-varying multipliers," in *Proceedings of the 2019 American Control Conference (ACC)*, Philadelphia, PA, USA, Jul. 10–12 2019, pp. 1786–1791. 8, 9, 10, 88

[50] J. M. Fry, D. Abou Jaoude, and M. Farhood, "Robustness analysis of uncertain time-varying systems using integral quadratic constraints with time-varying multipliers," Submitted. 8, 9, 10, 88, 116, 142

[51] M. Cantoni, U. Jönsson, and S. Khong, "Robust stability analysis for feedback interconnections of time-varying linear systems," *SIAM Journal on Control and Optimization*, vol. 51, no. 1, pp. 353–379, 2013. 8

[52] J. M. Fry and M. Farhood, "Robustness analysis of eventually periodic systems using integral quadratic constraints with periodic multipliers," in *Proceedings of the 2017*

IEEE 56th Annual Conference on Decision and Control (CDC), Melbourne, Australia, Dec. 12–15 2017, pp. 2967–2972. 9, 10, 88

[53] Hobby Express. Senior Telemaster Plus. [Online]. Available: http://hobbyexpress.com/senior-telemaster-laser-cut-kit/ 14

[54] B. Bacon and I. M. Gregory, "General equations of motion for a damaged asymmetric aircraft," in *AIAA Atmospheric Flight Mechanics Conference and Exhibit*, Reston, Virigina, Aug. 2007, pp. 1–13. 15

[55] APC Propellers. [Online]. Available: https://www.apcprop.com/technical-information/ 16

[56] R. V. Jategaonkar, *Flight Vehicle System Identification: A Time–Domain Methodology*. Reston, VA: AIAA, 2006. 17, 31

[57] U. T. Jönsson, C.-Y. Kao, A. V. Megretski, and A. Rantzer, "A guide To IQC β: A MATLAB toolbox for robust stability and performance analysis," 2004. [Online]. Available: http://actrol.ee.nsysu.edu.tw/ 20, 24

[58] A. Rantzer, "On the Kalman–Yakubovich–Popov lemma," *Systems & Control Letters*, vol. 28, no. 1, pp. 7–10, 1996. 21

[59] P. Gahinet and P. Apkarian, "A linear matrix inequality approach to H_∞ control," *International Journal of Robust and Nonlinear Control*, vol. 4, no. 4, pp. 421–448, 1994. 27, 129

[60] O. Arifianto and M. Farhood, "Optimal control of a small fixed-wing UAV about concatenated trajectories," *Control Engineering Practice*, vol. 40, pp. 113–132, 2015. 27, 129

[61] S. Boyd and L. Vandenberghe, *Convex Optimization*. Cambridge University Press, 2004. 29

[62] R. D'Andrea and S. Khatri, "Kalman decomposition of linear fractional transformation representations and minimality," *Proceedings of the 1997 American Control Conference*, vol. 6, pp. 3557–3561, Jun. 1997. 33

[63] M. Farhood and G. E. Dullerud, "Model reduction of nonstationary LPV systems," *IEEE Transactions on Automatic Control*, vol. 52, no. 2, pp. 181–196, 2007. 33

[64] D. Abou Jaoude and M. Farhood, "Coprime factors model reduction of spatially distributed LTV systems over arbitrary graphs," *IEEE Transactions on Automatic Control*, Dec. 2016. 33

[65] J. Veenman and C. W. Scherer, "IQC-synthesis with general dynamic multipliers," *International Journal of Robust and Nonlinear Control*, vol. 24, no. 17, pp. 3027–3056, 2014. 39

[66] S. Wang, H. Pfifer, and P. Seiler, "Robust synthesis for linear parameter varying systems using integral quadratic constraints," *Automatica*, vol. 68, pp. 111–118, 2016. 39

[67] S. O. R. Moheimani, A. V. Savkin, and I. R. Petersen, "Minimax optimal control of discrete-time uncertain systems with structured uncertainty," *Dynamics and Control*, vol. 7, no. 1, pp. 5–24, Jan 1997. 39

[68] I. R. Petersen, M. R. James, and P. Dupuis, "Minimax optimal control of stochastic uncertain systems with relative entropy constraints," *IEEE Transactions on Automatic Control*, vol. 45, no. 3, pp. 398–412, Mar. 2000. 39

[69] C.-Y. Kao, M. Ravuri, and A. Megretski, "Control synthesis with dynamic integral quadratic constraints-LMI approach," in *Decision and Control, 2000. Proceedings of the 39th IEEE Conference on*, vol. 2. IEEE, 2000, pp. 1477–1482. 39

[70] P. Apkarian and D. Noll, "IQC analysis and synthesis via nonsmooth optimization," *Systems & Control Letters*, vol. 55, no. 12, pp. 971–981, 2006. 39

[71] C.-Y. Kao, A. Megretski, and U. Jönsson, "Specialized fast algorithms for IQC feasibility and optimization problems," *Automatica*, vol. 40, no. 2, pp. 239–252, 2004. 39

[72] D. Abou Jaoude, M. C. Palframan, and M. Farhood, "An oracle for the discrete-time integral quadratic constraint problem," *Automatica*, vol. 107, pp. 112–118, 2019. 39

[73] J. F. Magni, "User manual of the linear fractional representation toolbox," ONERA, Toulouse, France, Tech. Rep., 2006. 41

[74] J. Löfberg, "Yalmip : A toolbox for modeling and optimization in matlab," in *In Proceedings of the CACSD Conference*, Taipei, Taiwan, 2004. 41, 71, 130, 138

[75] MOSEK ApS, *The MOSEK optimization toolbox for MATLAB manual. Version 8.0.*, 2017. [Online]. Available: http://docs.mosek.com/8.0/intro/index.html 41, 130, 138

[76] T. R. Beal, "Digital simulation of atmospheric turbulence for Dryden and von Karman models," *Journal of Guidance, Control, and Dynamics*, vol. 16, no. 1, pp. 132–138, 2000. 47

[77] R. L. Bishop, "There is more than one way to frame a curve," *The American Mathematical Monthly*, vol. 82, no. 3, pp. 246–251, 1975. 53

[78] A. Hanson and H. Ma, "Parallel transport approach to curve framing," Department of Computer Science, Indiana University, Bloomington, IN, Tech. Rep. 425, 1995. 53

[79] M. Izumi, O. Atsumi, and S. Nobuhide, "LMI--based controller synthesis: A unified formulation and solution," *International Journal of Robust and Nonlinear Control*, vol. 8, no. 8, pp. 669–686, 1998. 60

[80] K. Zhou, J. Doyle, K. Glover, and B. Bodenheimer, "Mixed $\mathcal{H}_2$ and $\mathcal{H}_\infty$ control," in *1990 American Control Conference*, May 1990, pp. 2502–2507. 61

[81] R. W. Beard and T. W. McLain, *Small Unmanned Aircraft: Theory and Practice*. Princeton, NJ: Princeton University Press, 2012. 61

[82] J. E. Dennis and R. B. Schnabel, *Numerical Methods for Unconstrained Optimization and Nonlinear Equations*. SIAM, 1996. 68

[83] B. Borchers, "CSDP, a C library for semidefinite programming," *Optimization Methods and Software*, vol. 11, no. 1–4, pp. 613–623, 1999. 71

[84] J. F. Sturm, "Using SeDuMi 1.02, a matlab toolbox for optimization over symmetric cones," *Optimization Methods and Software*, vol. 11, no. 1-4, pp. 625–653, 1999. 73

[85] *Flying Qualities of Piloted Airplanes*, U.S. Department of Defense Std. MIL-F-8785C, Nov. 1980. 74

[86] S. Gage, "Creating a unified graphical wind turbulence model from multiple specifications," in *AIAA Modeling and Simulation Technologies Conference and Exhibit*, Austin, Texas, 2003. 74

[87] Gumstix. Gumstix overo fire. [Online]. Available: https://store.gumstix.com/coms/overo-coms/overo-firestorm-y-com.html 76

[88] Pixhawk. [Online]. Available: https://pixhawk.org/modules/pixhawk 76

[89] J. Doyle, "Guaranteed margins for LQG regulators," *IEEE Transactions on Automatic Control*, vol. 23, no. 4, pp. 756–757, Aug. 1978. 86

[90] G. E. Dullerud and S. Lall, "A new approach for analysis and synthesis of time-varying systems," *IEEE Transactions on Automatic Control*, vol. 44, no. 8, pp. 1486–1497, 1999. 88, 89, 119, 132, 135

[91] M. Fetzer and C. W. Scherer, "Full-block multipliers for repeated, slope-restricted scalar nonlinearities," *International Journal of Robust and Nonlinear Control*, vol. 27, no. 17, pp. 3376–3411, 2017. 102

[92] V. Hutson, J. S. Pym, and M. J. Cloud, *Applications of Functional Analysis and Operator Theory*. Amsterdam, The Netherlands: Elsevier, 2005. 110, 119

[93] J. Engwerda, *LQ dynamic optimization and differential games*. John Wiley & Sons, 2005. 112

[94] P. R. Halmos, *A Hilbert Space Problem Book*, ser. Graduate Texts in Mathematics. Springer-Verlag New York, 1974. 119

[95] M. Farhood and G. E. Dullerud, "LMI tools for eventually periodic systems," *Systems & Control Letters*, vol. 47, pp. 417–432, Dec. 2002. 120, 121, 135

[96] ——, "Duality and eventually periodic systems," *International Journal of Robust and Nonlinear Control*, vol. 15, no. 13, pp. 575–599, Sep. 2005. 121

[97] H. Köroğlu and C. W. Scherer, "Robust performance analysis for structured linear time-varying perturbations with bounded rates-of-variation," *IEEE Transactions on Automatic Control*, vol. 52, no. 2, pp. 197–211, 2007. 124

[98] M. Farhood and G. E. Dullerud, "Control of systems with uncertain initial conditions," *IEEE Transactions on Automatic Control*, vol. 53, no. 11, pp. 2646–2651, 2008. 126

[99] Hobby Express. Junior Telemaster. [Online]. Available: http://hobbyexpress.com/deluxe-telemaster-40-kit/ 127

[100] G. E. Dullerud and F. G. Paganini, *A course in robust control theory: a convex approach*. New York: Springer, 2000. 129

[101] M. Farhood and G. E. Dullerud, "Control of nonstationary LPV systems," *Automatica*, vol. 44, no. 8, pp. 2108–2119, Aug. 2008. 131, 135

[102] M. Farhood, "LPV control of nonstationary systems: A parameter-dependent Lyapunov approach," *IEEE Transactions on Automatic Control*, vol. 57, no. 1, pp. 209–215, Jan. 2012. 135

[103] ——, "Nonstationary LPV control for trajectory tracking: A double pendulum example," *International Journal of Control*, vol. 85, no. 5, pp. 545–562, May 2012. 135

[104] *Flight Control Systems – Design, Installation and Test of Piloted Aircraft, General Specification for*, U.S. Department of Defense Std. MIL-DTL-9490E, Apr. 2008. 141